1993

End-to-end analysis of hexagonal vs rectangular sampling in digital imaging systems

John Clifton Burton II
College of William & Mary - Arts & Sciences

Order Number 9403277

End-to-end analysis of hexagonal vs. rectangular sampling in digital imaging systems

Burton, John Clifton, II, Ph.D.

The College of William and Mary, 1993

U·M·I
300 N. Zeeb Rd.
Ann Arbor, MI 48106

END-TO-END ANALYSIS OF HEXAGONAL VS. RECTANGULAR SAMPLING IN DIGITAL IMAGING SYSTEMS

A DISSERTATION
PRESENTED TO
THE FACULTY OF THE DEPARTMENT OF COMPUTER SCIENCE
THE COLLEGE OF WILLIAM AND MARY IN VIRGINIA

IN PARTIAL FULFILLMENT
OF THE REQUIREMENTS FOR THE DEGREE OF
DOCTOR OF PHILOSOPHY

By
John C. Burton II
April 1993

APPROVAL SHEET

This dissertation is submitted in partial fulfillment of
the requirements of the degree of
Doctor of Philosophy

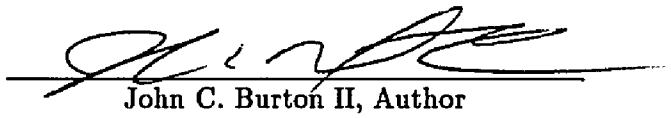

John C. Burton II, Author

Approved, April 1993

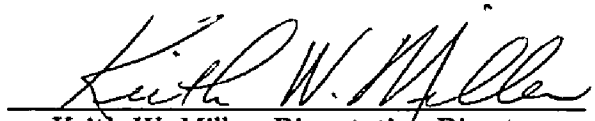

Keith W. Miller, Dissertation Director

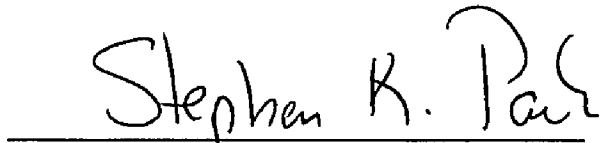

Stephen K. Park

William L. Bynum

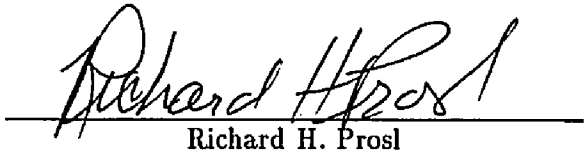

Richard H. Prosl

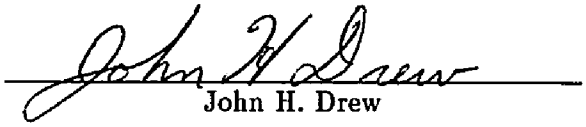

John H. Drew

Dedication

This dissertation is dedicated to the memory of my father, John Burton, whose thirst for knowledge and curiosity about the world around him left a lasting impression on me.

Contents

Acknowledgments

I am grateful to Professor Keith W. Miller for guiding me through the process of this research, and to Professor Stephen K. Park for providing valuable insights into this field. Portions of this work were supported by NASA Graduate Researcher Fellowship Grant NGT-50111 at the NASA Langley Research Center. I am indebted to my wife, Maia T. Conrad for her understanding and patience, and to my daughter Jordan for helping to keep my life in perspective.

List of Tables

List of Figures

Abstract

The purpose of this study was to compare two common methods for image sampling in digital image processing: hexagonal sampling and rectangular sampling. The two methods differ primarily in the arrangement of the sample points on the image focal plane. In order to quantitatively compare the two sampling methods, a mathematical model of an idealized digital imaging system was used to develop a set of mean–squared–error fidelity loss metrics. The noiseless continuous/discrete/continuous end–to–end digital imaging system model consisted of four independent components: an input scene, an image formation point spread function, a sampling function, and a reconstruction function. The metrics measured the amount of fidelity lost by an image due to image formation, sampling and reconstruction, and the combined loss for the entire system.

End–To–End Analysis of Hexagonal vs. Rectangular Sampling in Digital Imaging Systems

Chapter 1

Introduction

An often overlooked area in the end–to–end analysis of digital imaging systems is the sampling of the continuous scene into discrete units of information, and the subsequent reconstruction of this discrete information into the continuous output image. Many researchers have studied the sampling operation in isolation or in conjunction with an *ideal* reconstruction function, but relatively little effort has been spent to analyze these operations in the context of the complete, end–to–end imaging system. Regular hexagonal sampling is considered to be the optimal sampling geometry, and is optimal, under specific conditions. Rectangular sampling is the de-facto standard for virtually all hardware devices and software tools developed. If hexagonal sampling is the superior sampling geometry, then why is rectangular sampling the de-facto standard? Is hexagonal sampling still the optimal sampling geometry for conditions outside those reported? If the answers to these and similar questions are to have any applicability to real world imaging systems, then the comparison of the sampling geometries must be made in the context of an end–to–end digital imaging system.

To facilitate the comparison of rectangular sampling to hexagonal sampling, this dissertation provides a common mathematical framework for analyzing image fidelity losses in sampled imaging systems. The fidelity losses considered are due to blurring during image formation, aliasing due to undersampling, and imperfect reconstruction. The analysis of the individual and combined effects of these losses is based upon an idealized, noiseless, continuous/discrete/continuous end–to–end digital imaging system model consisting of four independent system components: an input scene, an image gathering point spread function, a generalized sampling function, and an image reconstruction function. The generalized sampling function encompasses both rectangular and hexagonal sampling lattices. Quantification of the image fidelity losses is accomplished via the mean–squared–error (MSE) metrics: imaging fidelity loss, sampling and reconstruction fidelity loss, and end–to–end fidelity loss. Shift–variant sampling effects are accounted for with an expected value analysis. This mathematical framework is used as the basis for a series of simulations comparing

a rectangular (square) sampling grid to a hexagonal sampling grid for a variety of image formation and image reconstruction conditions.

The fidelity loss metrics developed provide invaluable insight into the tradeoffs, including sampling grid geometry and reconstruction operation, encountered in the design of a digital imaging system. The experimental results clearly demonstrate the intimate relationship among the various system components in general, and the sampling and reconstruction operations in particular. Specifically, if any advantages from the use of a particular sampling grid are to be realized, then the reconstruction component must be designed specifically for that sampling grid.

1.1 Background

In 1949 Shannon presented landmark papers, *Communication in the Presence of Noise* [1], and *The Mathematical Theory of Communication* [2], which provided a basis for many subsequent developments in digital signal and image processing. Of particular importance to this thesis was the presentation of what is now often considered *Shannon's Sampling Theorem*, which states [2],

> *If a function of time $f(t)$ is limited to the band from 0 to W cycles per second it is completely determined by giving its ordinates at a series of discrete points spaced $\frac{1}{2W}$ seconds apart in the manner indicated by the following result.*
>
> *Theorem: Let $f(t)$ contain no frequencies over W.*
> *Then*
>
> $$f(t) = \sum_{n=-\infty}^{\infty} X_n \frac{\sin \pi(2Wt - n)}{\pi(2Wt - n)}$$
>
> *where*
>
> $$X_n = f\left(\frac{n}{2W}\right).$$

Building upon the ideas in [1] and [2], Petersen and Middleton [3] extended Shannon's one dimensional sampling theorem to include multidimensional spaces having generalized periodic sampling geometries. Petersen and Middleton's *N-dimensional sampling theorem* states:

> *A function $f(\mathbf{x})$ whose Fourier transform $F(\omega)$ vanishes over all but a finite portion of wave-number space can be everywhere reproduced from its sample values taken over a lattice of points*
>
> $$\{l_1\mathbf{v}_1 + l_2\mathbf{v}_2 + \cdots + l_N\mathbf{v}_N\}, l_1, l_2, \cdots, l_N = 0, \pm 1, \pm 2, \cdots,$$
>
> *provided that the vectors $\{\mathbf{v}_j\}$ are small enough to ensure non-overlapping of the spectrum $F(\omega)$ with its images on a periodic lattice defined by the vectors $\{\mathbf{u}_k\}$, with $\mathbf{v}_j \cdot \mathbf{u}_k = 2\pi\delta_{jk}$.*

Central to both the one-dimensional sampling theorem [1,2] and the N-dimensional sampling theorem [3] is the existence of a reconstruction function that will exactly reproduce a sufficiently sampled function from its sampled values. For a function to be exactly reconstructed from its sampled values, the function must have a Fourier transform which is zero outside a specific base band-region in Fourier space. The reconstruction function that will exactly reproduce such a function from its sampled values is characterized by having a Fourier transform with a constant non-zero value over the base band-region of the sampled function, and a value of zero wherever the periodically replicated band-regions of the sampled function are non-zero [3]. For one-dimensional sampling the most common reconstruction function is the *rectangular pulse function* covering the baseband of the sampled function. The Fourier transform of the rectangular pulse is the sinc() function, where $\text{sinc}(x) = \sin(\pi x)/\pi x$, which is the reconstruction function described by Shannon [1].

1.2 Hexagonal Sampling

An interesting observation made by Petersen and Middleton and supported by subsequent researchers [4–9] is that in two-dimensional space rectangular sampling is not the optimal sampling geometry, and has several drawbacks including spatial resolution that varies with direction [4]. The sampling geometry that was cited by these researchers as being optimal was a regular hexagonal pattern.

> *Hexagonal sampling is the optimal sampling scheme for signals which are band-limited over a circular region of the Fourier plane, in the sense that exact reconstruction of the waveform requires a lower sampling density than with alternative schemes. For such signals hexagonal sampling requires 13.4 percent fewer samples than rectangular sampling.* [6]

Sampling density for a given sampling geometry is proportional to the area in the Fourier domain of the parallelepiped formed by the centers of four adjacent replicated band-regions [3,6] as shown by the shaded regions in figures 1.1(a) and 1.1(b).

The figure of 13.4 percent comes from a Fourier domain *bin-packing* argument; the most efficient packing of equal sized circles (circular band-regions) on a plane is a regular hexagonal arrangement (six circles surrounding and equidistant from a central circle), and the area of the parallelepiped for a regular hexagonal grid is 13.4 percent less than the area of the parallelepiped for the rectangular grid. A more recent investigation into imaging system design by Fales et al. [10,11] suggests that in terms of information density the hexagonal sampling lattice provides approximately 5 percent improvement over the rectangular sampling lattice. The two figures (5% and 13.4%) are not directly comparable since they result from different comparison metrics, and are based on different assumptions. In particular, Fales et al. [10] based their work on a constant sampling density and photo-sensor aperture

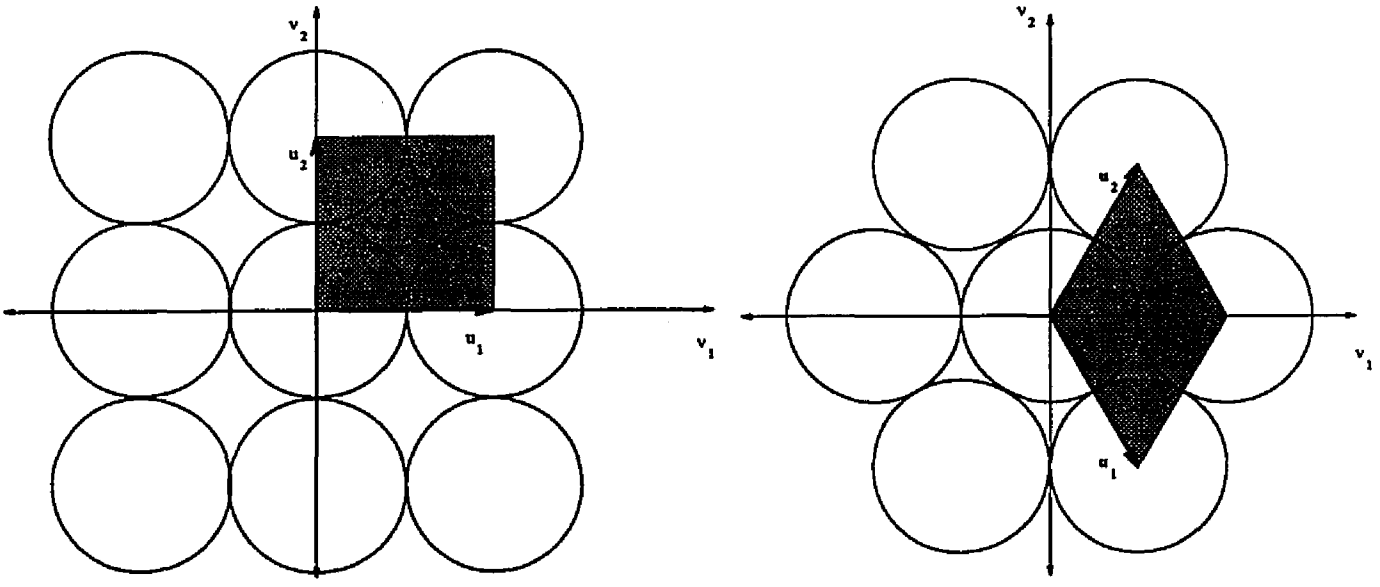

(a) Rectangular Sampling (b) Hexagonal Sampling

Figure 1.1: Fourier Domain Representation of Sampling Grids

size instead of assuming a sufficiently sampled, circularly band-limited signal. While not directly comparable, both studies tend to indicate that hexagonal sampling has an advantage over rectangular sampling in the ability to accurately sample and reconstruct the input scenes specified.

In the areas of computer vision, symbolic image description, and related fields, a fundamental problem is determining the geometrical relationship or connectivity of pixels representing regions considered to be of the same type or class. The main difficulty with rectangular sampling is the ambiguity in defining what constitutes a nearest neighbor [12], a problem not encountered with hexagonal sampling [13–16]. Methods for extracting and manipulating these topological properties on a hexagonal grid for binary images have been developed [17,18] based on work by Golay [19]. One goal that is often associated with computer vision is the emulation of the human visual process, which is based on a natural image acquisition device (e.g. the human eye) with a sensor array that closely approximates a hexagonal tessellation [20,21].

1.3 Rectangular Sampling

Traditionally rectangular sampling has been the method of choice for virtually all signal and image processing applications. By far, most of the hardware devices and software tools

developed for image processing are based on this scheme. The algorithms used for processing rectangularly sampled images are, in most cases, a straightforward generalization from the one-dimensional case. The resulting expressions can be easily understood and implemented in software. Many text books concerning digital image processing [22–24] do not even consider alternate sampling schemes and simply assume the use of rectangular sampling. The few text books that do mention hexagonal sampling [13,14] briefly discuss it in the context of computer vision and image understanding, not in the context of traditional image processing.

The proponents of a rectangular sampling geometry cite the mathematical convenience of rectangular sampling models and the mechanical simplicity of imaging systems based on a rectangular photo-detector grid. These advantages are significant, but if for a fixed number of photo-detectors a hexagonal sampling geometry can deliver higher quality images, then for some applications mathematical inconvenience and mechanical complexity may be less important than the improved quality. To facilitate this kind of trade–off study, quantitative measurements of image fidelity are needed to reasonably compare sampling geometries.

1.4 Comparisons

In order to quantitatively compare rectangular and hexagonal sampling, a set of metrics is needed that can be applied directly to both sampling geometries. In 1982 Park and Schowengerdt [25] introduced a mean–squared–error (MSE) methodology for analyzing the loss of imaging fidelity for a one-dimensional digital imaging system. This methodology explicitly measured the loss of fidelity due to the image formation operation and the loss of fidelity due to the sampling and reconstruction operations. It also accounted for the shift–variant sampling effects encountered when the scene contains features that are finer than the the sampling grid inter-sample distance (i.e. sampling is *shift-variant* at the sub–pixel level). Subsequent efforts extended the image formation fidelity loss and sampling and reconstruction fidelity loss metrics to a normalized rectangularly sampled two dimensional digital imaging system [26,27], and introduced an additional metric for end–to–end fidelity loss [28–30]. These fidelity loss metrics were extended to account for both hexagonal and rectangular sampling grids [31,32], based on the work by Mersereau [5,7] and Ulichney [33] concerning generalized sampling grids. These extended fidelity loss metrics were used as the basis for simulations comparing rectangular sampling grids to hexagonal sampling grids under a variety of conditions.

1.5 Chapter Description

Chapter 2 Imaging System Model. Chapter 2 describes the end–to–end system model used for the development of the fidelity loss metrics and subsequent experimentation. This continuous/discrete/continuous end–to–end digital imaging system model is based on the model developed and used by Park et.al. The system is characterized by four independent components referenced to a common orthogonal 2-dimensional spatial coordinate system. The use of this model–based approach facilitates the direct comparison of hexagonal and rectangular sampling, and provides a simulation environment that can be accurately and precisely controlled.

Chapter 3 Fidelity Loss Metrics. Chapter 3 develops a mathematical framework for analyzing image fidelity losses in hexagonally and rectangularly sampled digital imaging systems. Quantification of the image fidelity losses is accomplished via three mean–squared–error (MSE) metrics: imaging fidelity loss, sampling and reconstruction fidelity loss, and end–to–end fidelity loss. Sub–pixel, shift–variant sampling effects are accounted for with a sample–scene phase expected value analysis.

Chapter 4 Experimental Results — Synthetic Scenes. In chapter 4 *synthetic scenes* are used for an in-depth investigation into the mechanisms contributing to imaging system fidelity losses by providing strict control over the frequency content of the scene. The parameters investigated include type of scene, band-limit of the scene, optical transfer function shape, and reconstruction function type and shape. The fidelity loss metrics described in chapter 3 are used to provide quantitative comparisons as a function of synthetic scene frequency content.

Chapter 5 Experimental Results — Digital Scenes. The results obtained in chapter 4 provide significant insight into the mechanisms of fidelity loss in a digital imaging system, but provide little information concerning the (spatial) visual appearance of various fidelity losses as perceived by a human observer. The results presented in chapter 5 provide insight into how the various fidelity loss mechanisms affect the spatial structure of digital images. Quantitative results for the digital scenes were obtained using the metrics described in chapter 3 and used in chapter 4. Digital images with various levels and types of fidelity loss are given to provide qualitative comparisons.

Chapter 6 Summary and Conclusions. Chapter 6 summarizes the results presented in chapters 4 and 5 and presents the conclusions drawn from these results. In particular, while hexagonal sampling proved to be marginally superior to rectangular sampling for the majority of conditions investigated, the advantages of a particular sampling grid can easily be negated by improper design of the other system components.

References

[1] Claude E. Shannon. Communication in the presence of noise. *Proceedings of the IRE*, 37(1):10–21, 1949.

[2] Claude Shannon and Warren Weaver. *The Mathematical Theory of Communication.* University of Illinois Press, Urbana, IL, 1964. Originally published in the *Bell System Technical Journal*, 27:379–423 and 28:623–656, 1948.

[3] Daniel P. Petersen and David Middleton. Sampling and reconstruction of wave-number-limited functions in n-dimensional euclidean spaces. *Information and Control*, 5(4):279–323, 1962.

[4] Richard R. Legault. The aliasing problems in two-dimensional sampled imagery. In Lucien M. Biberman, editor, *Perception of Displayed Information*, chapter 7, pages 279–312. Plenum Press, New York, NY, 1973.

[5] Dan E. Dudgeon and Russell M. Mersereau. *Multidimensional Digital Signal Processing.* Prentice-Hall, Englewood Cliffs, NJ, 1984.

[6] Russel M. Mersereau. The processing of hexagonally sampled two-dimensional signals. *Proceedings of the IEEE*, 67(6):930–949, 1979.

[7] Russell M. Mersereau and Theresa C. Speake. The processing of periodically sampled multidimensional signal. *IEEE Transactions on Acoustics, Speech, and Signal Processing*, 31(5):188–194, 1983.

[8] Kwan F. Cheung and Robert J. Marks. Image sampling below the nyquist density without aliasing. *Journal of the Optical Society of America A*, 7(1):92–105, 1990.

[9] Robert J. Marks. Multidimensional signal sample dependency at nyquist densities. *Journal of the Optical Society of America A*, 3(2):268–273, 1986.

[10] Carl L. Fales, Friedrich O. Huck, and Richard W. Samms. Image system design for improved information capacity. *Applied Optics*, 23(6):872–888, 1984.

[11] Friedrich O. Huck, Carl L. Fales, Stephen K. Park, and Richard W. Samms. Image-plane processing for improved computer vision. In *NASA Conference Publication 2302*, pages 19–34. NASA, August 1983.

[12] Azriel Rosenfeld and Avinash C. Kak. *Digital Picture Processing.* Academic Press, Orlando, FL, second edition, 1982.

[13] William K. Pratt. *Digital Image Processing.* John Wiley and Sons, New York, NY, 1978.

[14] Berthold Klaus Paul Horn. *Robot Vision.* MIT Press, Cambridge, MA, 1986.

[15] Richard O. Duda and P. E. Hart. *Pattern Classification and Scene Analysis.* John Wiley and Sons, New York, NY, 1973.

[16] Dana H. Ballard and Christopher M. Brown. *Computer Vision.* Prentice-Hall, Englewood Cliffs, NJ, 1982.

[17] Stephen B. Gray. Local properties of binary images in two dimensions. *IEEE Transactions on Computers*, C-20(5):551–561, 1971.

[18] Kendall Jr. Preston. Feature extraction by golay hexagonal pattern transforms. *IEEE Transactions on Computers*, C-20(9):1007–1014, 1971.

[19] Marcel Golay. Hexagonal parallel pattern transformations. *IEEE Transactions on Computers*, C-18(8):733–740, 1969.

[20] Martin D. Levine, editor. *Vision in Man and Machine.* McGraw-Hill, New York, NY, 1985.

[21] Andrew B. Watson and Albert J. Ahumada. A hexagonal orthogonal–oriented pyramid as a model of image representation in visual cortex. *IEEE Transactions on Biomedical Engineering*, 36(1):97–106, 1989.

[22] Rafael C. Gonzalez and Paul Wintz. *Digital Image Processing.* Addison-Wesley, Reading, MA, second edition, 1987.

[23] H. C. Andrews and B. R. Hunt. *Digital Image Restoration.* Prentice-Hall, Englewood Cliffs, NJ, 1977.

[24] William B. Green. *Digital Image Processing: A Systems Approach.* Van Nostrand Reinhold, New York, NY, 1983.

[25] Stephen K. Park and Robert A. Schowengerdt. Image sampling, reconstruction, and the effect of sample-scene phasing. *Applied Optics*, 21(17):3142–3151, 1982.

[26] Robert Schowengerdt, Stephen K. Park, and Robert Gray. Topics in the two–dimensional sampling and reconstruction of images. *International Journal of Remote Sensing*, 5(2):333–347, 1984.

[27] Stephen K. Park, Robert A. Schowengerdt, and Mary-Anne Kaczynski. Modulation-transfer-function analysis for sampled image systems. *Applied Optics*, 23(15):2572–2582, 1984.

[28] Stephen K. Park and Stephen E. Reichenbach. Digital image gathering and minimum mean-square error restoration. In *Visual Communications and Image Processing V*, pages 1578–1589. Proc. SPIE 1360, 1990.

[29] Stephen K. Park. Linear digital imaging system fidelity analysis. In *Visual Information Processing for Television and Telerobotics*, pages 3–10. NASA Conf. Pub. 3053, 1989.

[30] Stephen K. Park. Image gathering, interpolation and restoration: A fidelity analysis. In *SPIE 1992 Technical Symposium on Visual Information Processing.* SPIE, 1992.

[31] John C. Burton, Stephen K. Park, and Keith W. Miller. Hexagonally sampled digital imaging system analysis. In *SPSE's 43rd Annual Conf.*, pages 238–241. SPSE, 1990.

[32] John C. Burton, Keith W. Miller, and Stephen K. Park. Fidelity metrics for hexagonally sampled digital imaging systems. *Journal of Imaging Technology*, 17(6):279–283, 1991.

[33] Robert Ulichney. *Digital Halftoning.* MIT Press, Cambridge, MA, 1987.

Chapter 2

The Imaging System Model

Of fundamental importance to scientific research is the development of a mathematical model describing the process or system under investigation. The model provides the basis for a simulation environment that can be accurately and precisely controlled by the investigator, and provides the flexibility necessary to investigate a broad range of conditions. A concise description of the model facilitates the validation of experimental results and extension of those results by others. The continuous/discrete/continuous end-to-end digital imaging system model used for this dissertation is based on the model presented by Park [1–4] and used by Park et. al. [5–9], as illustrated in figure 2.1. The following description of the imaging system model was previously presented by the author in [6], but in lesser detail. This chapter provides a more in-depth description of the imaging system model than was presented in [6].

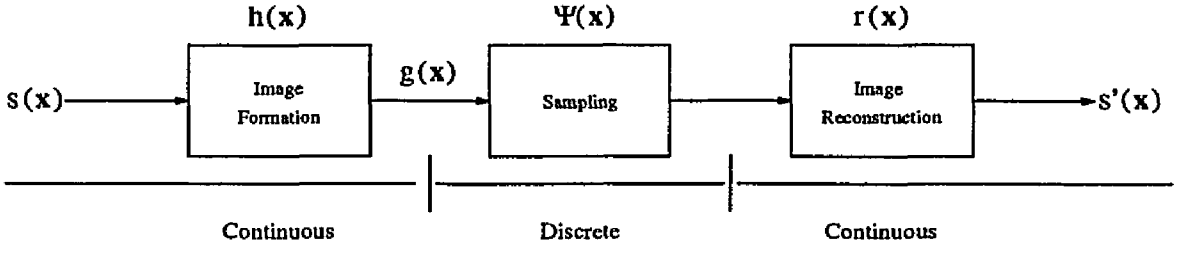

Figure 2.1: Typical Digital Image Processing System

The system is characterized by four independent system components: an input scene $s(\mathbf{x})$, an image formation point spread function $h(\mathbf{x})$, a sampling function $\Psi(\mathbf{x})$, and a reconstruction function $r(\mathbf{x})$. All four components are referenced to a common orthogonal 2-dimensional spatial coordinate system represented in vector notation by the 2-dimensional real column vector $\mathbf{x}$. For clarity two other components are included, the pre-sampling image

$g(\mathbf{x})$ and the reconstructed image $s'(\mathbf{x})$. The pre-sampling image is defined as

$$g(\mathbf{x}) = s(\mathbf{x}) * h(\mathbf{x}) \tag{2.1}$$

where $*$ is the convolution operation. The relation between the input scene s and the reconstructed image s' is given by

$$s'(\mathbf{x}) = \Big[[s(\mathbf{x}) * h(\mathbf{x})]\, \Psi(\mathbf{x}) \Big] * r(\mathbf{x}) \tag{2.2}$$

The model-based approach in this research facilitates the direct comparison of hexagonal sampling to rectangular sampling by allowing easy interchanging of the sampling functions and analytical determination of the fidelity loss for the various operations.

2.1 Scene

An end–to–end model of a digital imaging system starts with a *simulated scene*, a mathematical description of the input to the simulation. The properties of a simulated scene should correspond as closely as possible to those of a real scene. A real scene is continuous and can contain details that are too small to be resolved by the digital imaging system. Both image formation and sampling can obscure the sub–pixel details of a scene, but in fundamentally different ways. The accuracy of the simulation depends in part upon the ability of the simulated scene to provide details that are of sub-pixel dimensions [3, 8–10].

The model of a scene used for this dissertation is predicated on the property that a continuous 2-D periodic function with periods N_1 and N_2 can be exactly represented by the infinite 2-D Fourier series [3, 8, 11, 12].

$$s(x_1, x_2) = \sum_{\nu_1=-\infty}^{\infty} \sum_{\nu_2=-\infty}^{\infty} C[\nu_1, \nu_2] \exp\left(i2\pi \left(\frac{\nu_1 x_1}{N_1} + \frac{\nu_2 x_2}{N_2} \right) \right) \tag{2.3}$$

where

$$C[\nu_1, \nu_2] = \frac{1}{N_1 N_2} \int_{-\frac{N_2}{2}}^{\frac{N_2}{2}} \int_{-\frac{N_1}{2}}^{\frac{N_1}{2}} s(x_1, x_2) \exp\left(-i2\pi \left(\frac{\nu_1 x_1}{N_1} + \frac{\nu_2 x_2}{N_2} \right) \right) dx_1\, dx_2 \tag{2.4}$$

Or in terms of the integer column vector $\boldsymbol{\nu}$ and the real column vector $\mathbf{x}$,

$$s(\mathbf{x}) = \sum_{\boldsymbol{\nu}} C[\boldsymbol{\nu}] \exp\left(i2\pi \boldsymbol{\nu}^t \mathbf{N}^{-1} \mathbf{x} \right) \tag{2.5}$$

where

$$\sum_{\boldsymbol{\nu}} \equiv \sum_{\nu_1=-\infty}^{\infty} \sum_{\nu_2=-\infty}^{\infty}$$

$$\mathbf{x} \equiv \begin{bmatrix} x_1 \\ x_2 \end{bmatrix}$$
$$\nu \equiv \begin{bmatrix} \nu_1 \\ \nu_2 \end{bmatrix}$$
$$\mathbf{N} \equiv \begin{bmatrix} N_1 & 0 \\ 0 & N_2 \end{bmatrix}$$

and

$$C[\nu] = \frac{1}{|\det \mathbf{N}|} \int_{\mathbf{N}} s(\mathbf{x}) \exp\left(-\imath 2\pi \nu^t \mathbf{N}^{-1} \mathbf{x}\right) d\mathbf{x} \tag{2.6}$$

In theory the requirement of periodicity limits the usefulness of the Fourier series in representing natural scenes, which are aperiodic. In practice, however, it is useful to assume that the scene is continuous over a finite region and that this finite region is periodically replicated in both the x_1 and x_2 directions to completely tessellate the (x_1, x_2) plane [12].

A simulated scene based on an infinite Fourier series can include details smaller than the resolution of any given sampling grid because the infinite series can possess infinitely high frequencies. In reality, implementation of a simulated scene necessitates using a finite Fourier series instead of an infinite Fourier series; this imposes a band limit on the frequencies present.

For the purposes of this dissertation we will be considering a *band–limited* simulated scene. To be precise, a scene (or function) $s(\mathbf{x})$ is considered *band–limited* with band-region $\mathbf{K}$ iff

$$s(\mathbf{x}) = \sum_{\nu}^{\mathbf{K}} C[\nu] \exp\left(\imath 2\pi \nu^t \mathbf{N}^{-1} \mathbf{x}\right). \tag{2.7}$$

where

$$\sum_{\nu}^{\mathbf{K}} = \sum_{\nu_1 = -\frac{K_1}{2}}^{\frac{K_1}{2}} \sum_{\nu_2 = -\frac{K_2}{2}}^{\frac{K_2}{2}}. \tag{2.8}$$

and K_1, K_2 are positive integers. Equation 2.7 indicates that the *band–limited* scene $s(\mathbf{x})$ has no energy at frequencies outside the *band-region* $\mathbf{K}$. For the case of the rectangularly band–limited scene shown in figure 2.2 $C[\nu_1, \nu_2] = 0$ for $\nu_1 > |\frac{K_1}{2}|$ or $\nu_2 > |\frac{K_2}{2}|$. The band-region in figure 2.2 is depicted as rectangular for simplicity. In reality the actual band-region of the scene can be virtually any shape and generally depends upon the nature of the scene.

The simulated scene can be derived from an actual scene as captured by a digital image acquisition device (a *digital scene*), or it can be syntheticly generated/tailored for a specific application (a *synthetic scene*) [3,8,9]. These two types of scenes are complimentary; the synthetic scene provides direct control over scene statistics but little control over spatial structure; the digital scene provides control over spatial structure but little direct control

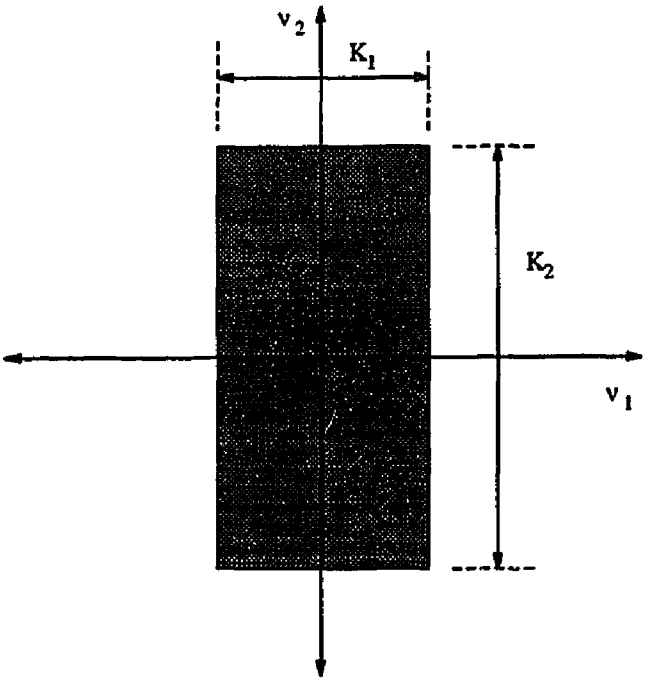

Figure 2.2: Rectangular Band-region

over scene statistics. The digital scene is represented by samples in the spatial domain, and the synthetic scene is represented by Fourier coefficients in the frequency domain.

2.1.1 Synthetic Scenes

A synthetic scene is constructed in the frequency domain by specifying the phase ($\phi[\nu]$) and amplitude ($\rho[\nu]$) values of the phase–amplitude form of a finite 2-D Fourier series, i.e.

$$s(\mathbf{x}) = \sum_{\nu}^{\mathbf{N}} \rho[\nu] \cos\left(\left(2\pi\nu^t \mathbf{N}^{-1}\mathbf{x}\right) - \phi[\nu]\right). \tag{2.9}$$

In this case the band-region of the scene, as represented by $\mathbf{K}$ in equation 2.7, is the same as the periodically replicated region represented by $\mathbf{N}$. Specification of the amplitude provides direct control over important scene statistics such as mean and autocorrelation (power spectrum in the frequency domain). Using random phase enables the creation of an entire family of scenes having similar statistical characteristics [3, 8]. The simulated scene given by equation 2.7 can be derived from equation 2.9 as follows:

$$s(\mathbf{x}) \;=\; \sum_{\nu}^{\mathbf{N}} \rho[\nu] \cos\left(\left(2\pi\nu^t \mathbf{N}^{-1}\mathbf{x}\right) - \phi[\nu]\right)$$

$$= \sum_{\nu}^{\mathbf{N}} A[\nu] \cos\left(2\pi\nu^t \mathbf{N}^{-1}\mathbf{x}\right) + B[\nu] \sin\left(2\pi\nu^t \mathbf{N}^{-1}\mathbf{x}\right) \tag{2.10}$$

where:

$$\begin{aligned} A[\nu] &= \rho[\nu]\cos(\phi[\nu]) \\ B[\nu] &= \rho[\nu]\sin(\phi[\nu]). \end{aligned}$$

Recalling that

$$\begin{aligned} \cos(\theta) &= \frac{\exp(i\theta)+\exp(-i\theta)}{2} \\ \sin(\theta) &= \frac{\exp(i\theta)-\exp(-i\theta)}{2i}, \end{aligned}$$

and defining

$$C[\nu] = \frac{1}{2}(A[\nu] - iB[\nu]),$$

produces the complex form of the Fourier series, i.e.

$$\begin{aligned} s(\mathbf{x}) &= \sum_{\nu}^{\mathbf{N}} C[\nu]\left(\cos\left(2\pi\nu^t \mathbf{N}^{-1}\mathbf{x}\right) + i\sin\left(2\pi\nu^t \mathbf{N}^{-1}\mathbf{x}\right)\right) \\ &= \sum_{\nu}^{\mathbf{N}} C[\nu]\exp\left(i2\pi\nu^t \mathbf{N}^{-1}\mathbf{x}\right). \end{aligned} \tag{2.11}$$

The simulated scene is now defined in terms of the complex Fourier series coefficients $C[\nu]$, obtained from syntheticly generated data. The value of any point in the scene $s(\mathbf{x})$ can now be determined based on equation 2.11 and $C[\nu]$.

2.1.2 Digital Scenes

Digital scenes are images that have been previously captured by a digital image acquisition device (camera). The acquisition operation imposes both spatial and spectral limits requiring the digital scene to be both *space-limited* and *band-limited.* The acquisition device has a finite field of view, imposing spatial limits; and has a finite number of sampling points, imposing spectral limits. The optics associated with the acquisition operation act as a low-pass filter, imposing additional spectral limits. The relationship between the spectral limits imposed by the sampling grid (number of sampling points) and the limits imposed by the optics determines if aliasing artifacts can be present in the captured image. When a digital image is used as a digital scene, any aliasing artifacts are considered part of the scene. A digital scene is not continuous; it is defined only at discrete points. According to

the sampling theorem [11–14], a rectangularly band-limited scene $s(\mathbf{x})$ with band-region $\mathbf{K}$ and sampling interval Δx_1 not exceeding $\frac{2}{K_1}$ and sampling interval Δx_2 not exceeding $\frac{2}{K_2}$ can be completely reconstructed from its sampled data $s(\mathbf{Vn})$ via

$$s(\mathbf{x}) = \sum_{\mathbf{n}} s(\mathbf{Vn}) \text{sinc}\left(2\mathbf{K}(\mathbf{x} - \mathbf{Vn})\right) \tag{2.12}$$

where

$$V = \begin{bmatrix} \Delta x_1 & 0 \\ 0 & \Delta x_2 \end{bmatrix},$$

and sinc $(\cdot)$ is the two dimensional ideal interpolation function. $s(\mathbf{x})$ is also spatially limited to a region in the (x_1,x_2) plane containing N_1 samples in the x_1 direction and N_2 samples in the x_2 direction. As with the synthetic scene, we assume $\mathbf{N} = \mathbf{K}$. For notational convenience, the sampled data $s(\mathbf{Vn})$ will be written as $s[\mathbf{n}]$. Normalizing the sampling interval (i.e. $\Delta x_1 = 1$ and $\Delta x_2 = 1$) equation 2.12 becomes

$$s(\mathbf{x}) = \sum_{\mathbf{n}}^{\mathbf{N}} s[\mathbf{n}] \text{sinc}\left(\mathbf{N}(\mathbf{x} - \mathbf{n})\right). \tag{2.13}$$

The simulated scene $s(\mathbf{x})$ is now defined in terms of the sampled data $s[\mathbf{n}]$. The value of $s(\mathbf{x})$ at any point in the scene can now be determined based on equation 2.13.

2.1.3 Comparison of Synthetic and Digital Scenes

Two methods have been described to generate a simulated scene: in the frequency domain as a synthetic scene, and in the spatial domain as a digital scene. The synthetic scene gives a great deal of control over the statistics of the scene, but provides little control over the spatial structure of the scene. The digital scene on the other hand provides a great deal of control over the spatial structure of the scene, but little direct control over the scene statistics. In this sense, the two development methods compliment one another, each providing experimental control unavailable or extremely limited with the other. The synthetic scene is a frequency domain representation using complex data, and the digital scene is a spatial domain representation using real data. Although the development of each type of simulated scene occurs in a different domain, it is straightforward converting between the two through the use of the discrete Fourier transform.

The frequency domain representation of the digital scene can be obtained by determining the Fourier series coefficients of the scene, i.e.

$$C[\boldsymbol{\nu}] = \frac{1}{|\det \mathbf{N}|} \int_{\mathbf{N}} s(\mathbf{x}) \exp\left(-\imath 2\pi \boldsymbol{\nu}^{\mathbf{t}} \mathbf{N}^{-\mathbf{1}} \mathbf{x}\right) d\mathbf{x}. \tag{2.14}$$

As shown in equation 2.13 the continuous simulated scene $s(\mathbf{x})$ is defined in terms of the set of discrete values $s[\mathbf{n}]$. Combining this with equation 2.14 produces

$$C[\nu] = \frac{1}{|\det \mathbf{N}|} \sum_{\mathbf{n}}^{\mathbf{N}} s[\mathbf{n}] \exp\left(-\imath 2\pi \nu^t \mathbf{N}^{-1} \mathbf{x}\right), \tag{2.15}$$

which is the discrete Fourier transform of the digital scene $s[\mathbf{n}]$.

From this development we find that the Fourier series coefficients of the digital scene can be obtained by taking the DFT of the sampled data. Similarly the sampled data can be recovered by taking the inverse DFT of the coefficient array. The simulated scene can be determined from the Fourier series coefficients using equation 2.11 or from the sampled image data using equation 2.13.

Up to this point we have considered two types of simulated scenes, the synthetic scene represented in the frequency domain, and the digital scene represented in the spatial domain. We have demonstrated procedures for converting the scenes from one domain to the other. From this point forward, no distinction will be made between the two type of scenes and we will consider a generic simulated scene that can be represented in either the frequency or spatial domain. The type of scene used (synthetic or digital) depends upon the desired end usage. If subjective visual comparisons of the reconstructed images is desired, then it is better to use a digital scene. If careful control of the frequency content of the scene is desired, then the synthetic scene should be used. The particular representation used for the scene is not critical to the simulation and more a matter of personal choice.

For the purposes of this simulation we will standardize on the frequency domain representation for the following reason: (*i*) The first stage of the simulation (optics) requires application of a point spread function (PSF) to the scene, a convolution operation in the spatial domain or a multiplication operation in the frequency domain. (*ii*) Sampling requires convolution in the frequency domain, or multiplication in the spatial domain. As some of the sampled points will not lie precisely on the discrete points of the spatial scene, interpolation with a sinc function would be required.

2.2 Image Formation

Image formation in a typical digital imaging system performs a non-isomorphic mapping of a finite area of the scene onto a finite image at the focal plane (sampling array) of the imaging device. The mapping is non-isomorphic in the sense that the virtual image is a spatially filtered proper subset of the actual scene. The degree of spatial filtering or blurring is modeled by a composite image formation *point spread function* (PSF), or equivalently by a composite image formation *optical transfer function* (OTF). The OTF is the Fourier transform of the PSF. This composite PSF consists of a *lens* PSF and a *sensor* PSF. The lens PSF describes the degree to which light received from a point source is spread across

the focal plane of the imaging device by the system optics. Even a perfectly focused lens produces some amount of filtering due to its physical characteristics [15,16]. The lens PSF is generally modeled as a small radially symmetric spot, decreasing in value from the center out. The corresponding OTF for many common image formation subsystems is accurately modeled as the radially symmetric function

$$\hat{h}_l(\omega_1, \omega_2) = \exp\left(-\left(\frac{\sqrt{\omega_1^2 + \omega_2^2}}{\alpha}\right)^{\beta}\right) \tag{2.16}$$

where α is the radial distance from the origin in the frequency domain at which the OTF is $\exp(-1)$ and β is a shape parameter [8,15]. A frequently used value is $\beta = 2$, in which case equation 2.16 becomes the *bell* or *Gaussian-spot* function shown in figure 2.3, with $\alpha = 0.25$. Note that $\hat{h}_l(\omega_1, \omega_2)$ is a continuous function and the quantities ω_1 and ω_2 are real valued frequency domain coordinates, which are related to the integer vector indices ν_1 and ν_2 via $\omega_1 = \nu_1/N_1$ and $\omega_2 = \nu_2/N_2$. It should be noted that the PSFs shown in figure 2.3(a) and throughout this dissertation are plotted on a normalized (x_1, x_2) scene coordinate system, i.e. $-N_1/2 < x_1 \leq N_1/2$ and $-N_2/2 < x_2 \leq N_2/2$

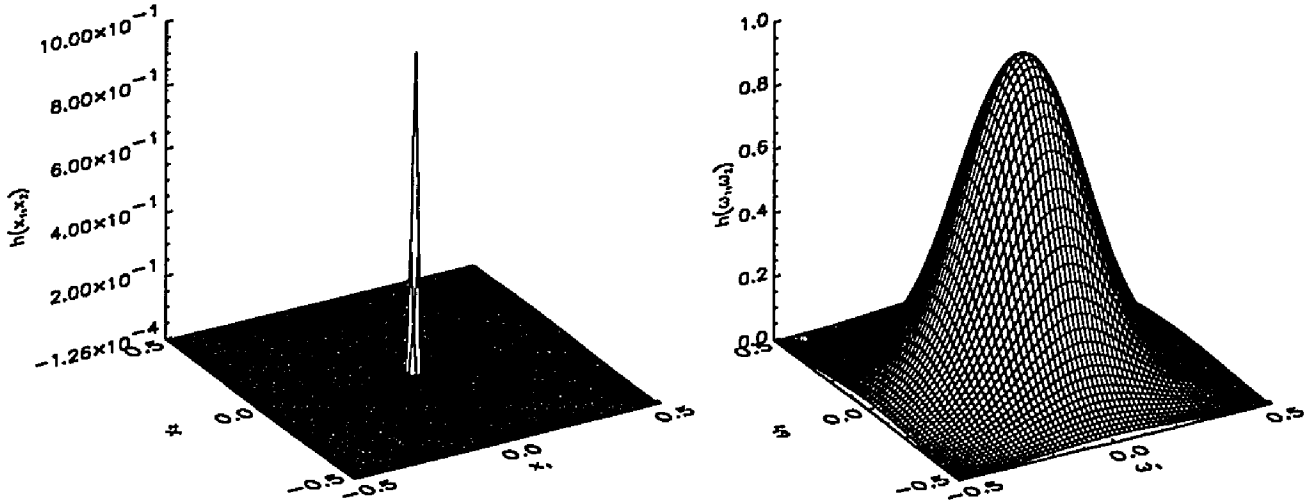

(a) Spatial Domain (PSF)

(b) Frequency Domain (OTF)

Figure 2.3: Example Optical Transfer Function

In the next section sampling is modeled as measuring the light intensity of the continuous formed image at uniformly spaced, infinitesimally small, discrete locations. These

sampled values are more accurately modeled as being obtained by integration over a non-infinitesimal area surrounding the sample point [8]. The integration is performed by the sensor response function (sensor PSF) $h_s(\mathbf{x})$; the corresponding sensor OTF is $\hat{h}_s(\omega)$. An example rectangular sensor OTF is shown in figure 2.4 and an example hexagonal sensor OTF is shown in figure 2.5.

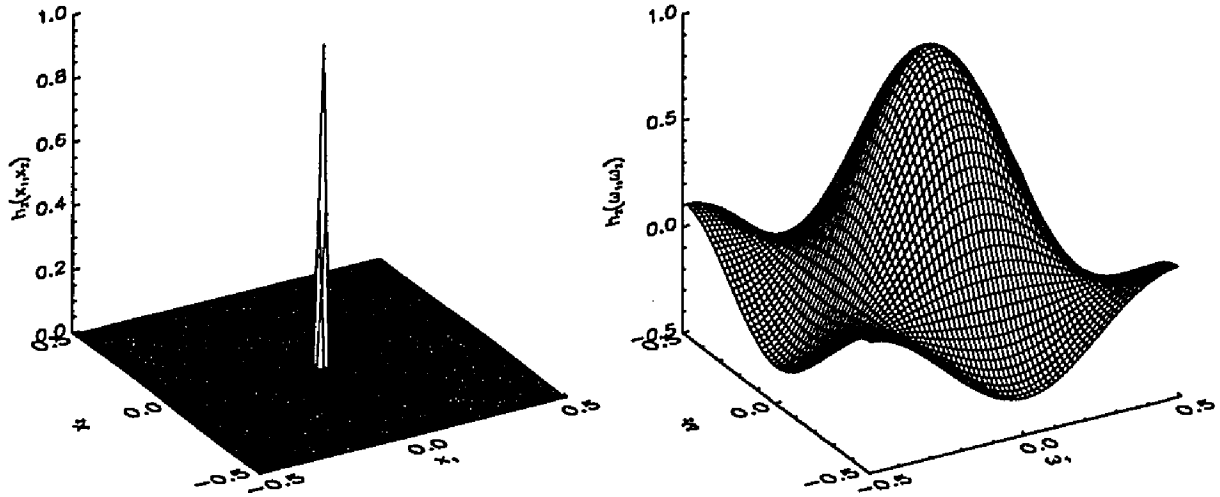

(a) Spatial Domain (PSF)

(b) Frequency Domain (OTF)

Figure 2.4: Sensor OTF for Rectangular Sensor Shape

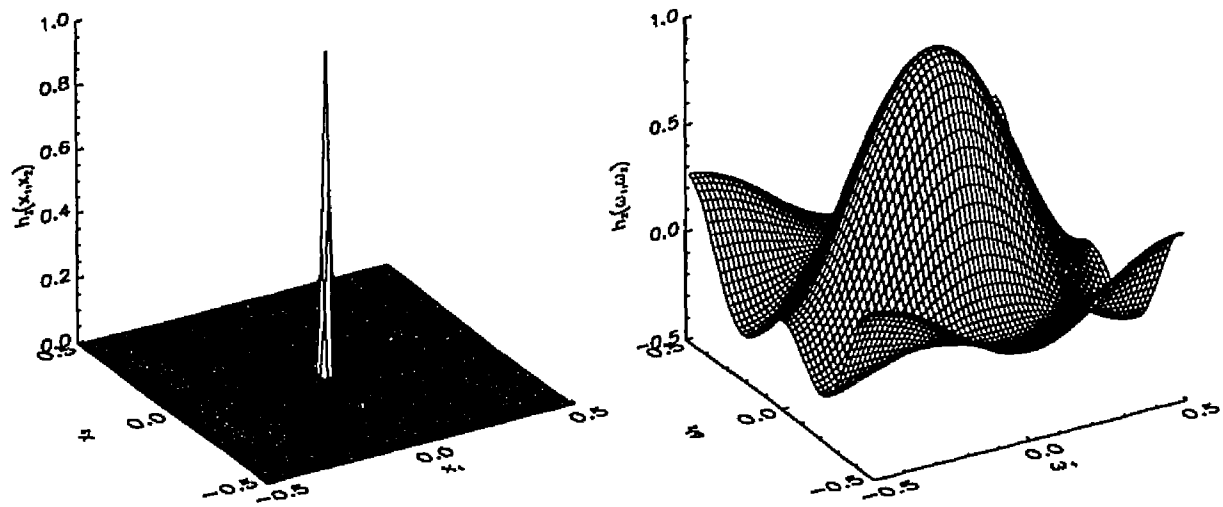

(a) Spatial Domain (PSF) (b) Frequency Domain (OTF)

Figure 2.5: Sensor OTF for Hexagonal Sensor Shape

The composite image formation PSF $h(\mathbf{x})$, shown in figures 2.6 and 2.7, is obtained by convolving the lens PSF $h_l(\mathbf{x})$ with the sensor PSF $h_s(\mathbf{x})$, i.e.

$$h(\mathbf{x}) = h_l(\mathbf{x}) * h_s(\mathbf{x}). \tag{2.17}$$

Equivalently the composite image formation OTF is obtained via frequency domain multiplication of the component OTFs, i.e.

$$\hat{h}(\omega) = \hat{h}_l(\omega)\,\hat{h}_s(\omega). \tag{2.18}$$

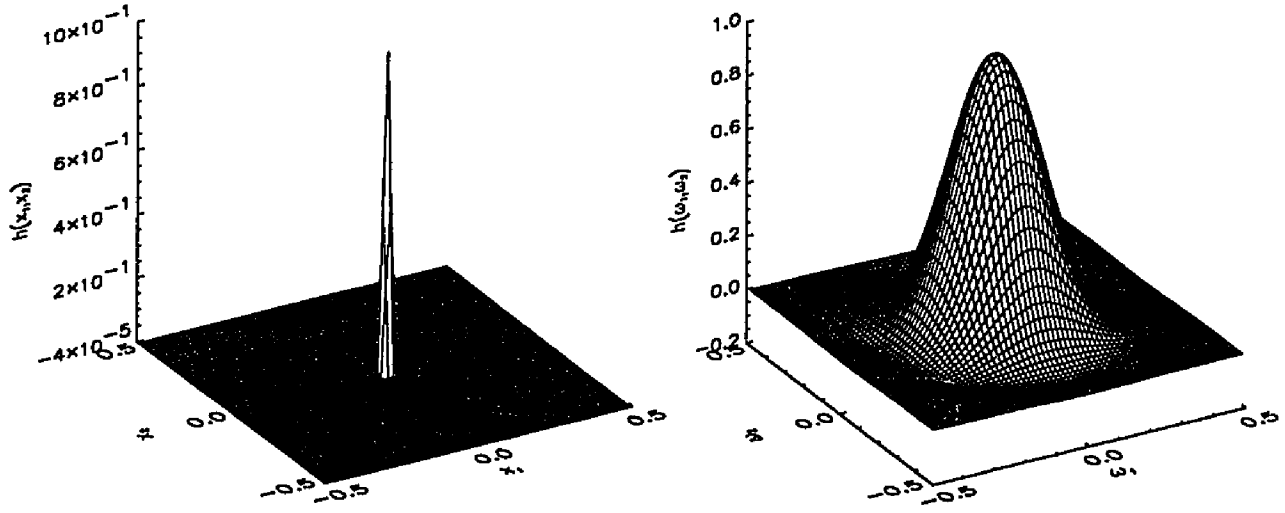

(a) Spatial Domain (PSF)

(b) Frequency Domain (OTF)

Figure 2.6: Composite OTF for Rectangular Sensor Shape

The image formation operation is simulated by the spatial domain convolution of the scene $s(\mathbf{x})$ and the composite image formation PSF $h(\mathbf{x})$ to produce the formed image $g(\mathbf{x})$, i.e.

$$g(\mathbf{x}) = h(\mathbf{x}) * s(\mathbf{x}) = \int_{\mathbf{x}'} h(\mathbf{x} - \mathbf{x}')\, s(\mathbf{x}') \tag{2.19}$$

or by multiplication in the frequency domain

$$\hat{g}(\omega) = \hat{h}(\omega)\,\hat{s}(\omega). \tag{2.20}$$

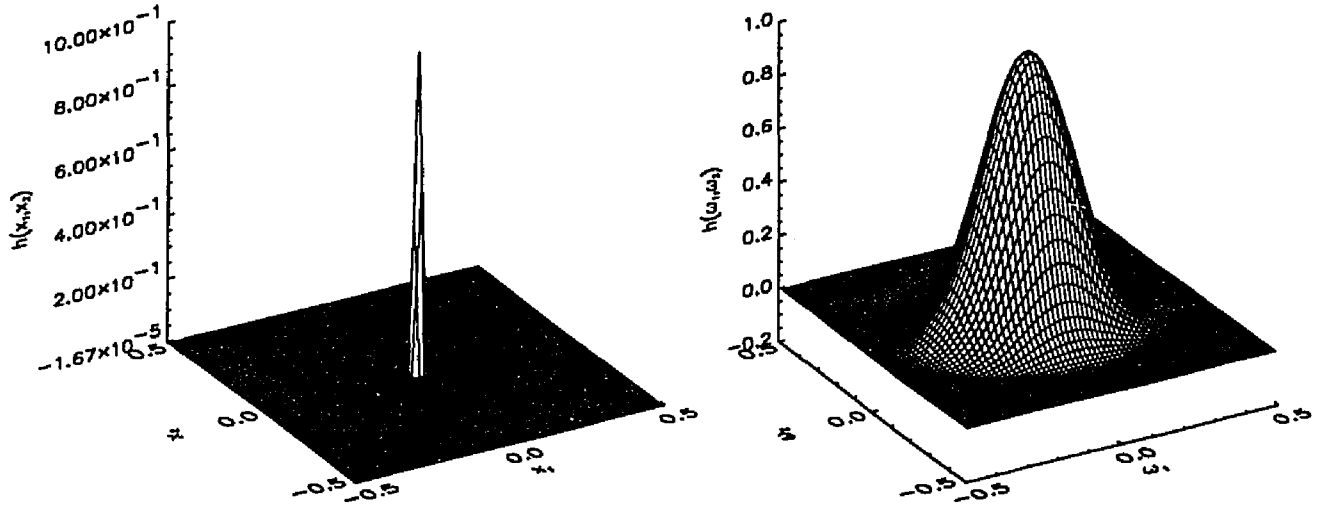

(a) Spatial Domain (PSF)

(b) Frequency Domain (OTF)

Figure 2.7: Composite OTF for Hexagonal Sensor Shape

2.3 Sampling

Traditional rectangular sampling in the spatial domain, with *sampling intervals* Δx_1 and Δx_2, is accomplished by multiplication of the continuous, formed scene $g(x_1, x_2)$ by the *shah* or *comb* function $\text{Ш}(x_1, x_2)$, i.e.

$$g(x_1, x_2)\text{Ш}(x_1, x_2) = g(x_1, x_2) \sum_{n_1=-\infty}^{\infty} \sum_{n_2=-\infty}^{\infty} \delta(x_1 - n_1\Delta x_1, x_2 - n_2\Delta x_2) \quad (2.21)$$

$$\vdots$$

$$= g(n_1\Delta x_1, n_2\Delta x_2). \quad (2.22)$$

where:

$$\text{Ш}(x_1, x_2) \equiv \sum_{n_1=-\infty}^{\infty} \sum_{n_2=-\infty}^{\infty} \delta(x_1 - n_1\Delta x_1, x_2 - n_2\Delta x_2) \quad (2.23)$$

and $\delta(x_1, x_2)$ is the two dimensional (Cartesian) Dirac delta function. In two dimensions, the *shah* function forms a lattice of points spread at uniform intervals over the plane to be sampled. Rectangular sampling is based on the rectangular sampling lattice shown in figure 2.8(a).

For complete reconstruction of the scene the magnitudes of the sampling intervals $\Delta x_1, \Delta x_2$ are determined by the band-region of the scene (shown in figure 2.2) and the periods of the scene, i.e.

$$\begin{aligned} \Delta x_1 &\leq \frac{N_1}{K_1} \\ \Delta x_2 &\leq \frac{N_2}{K_2} \end{aligned}$$

or since we assume $\mathbf{K} = \mathbf{N}$

$$\begin{aligned} \Delta x_1 &\leq 1 \\ \Delta x_2 &\leq 1. \end{aligned}$$

2.3.1 Arbitrary Sampling Geometries

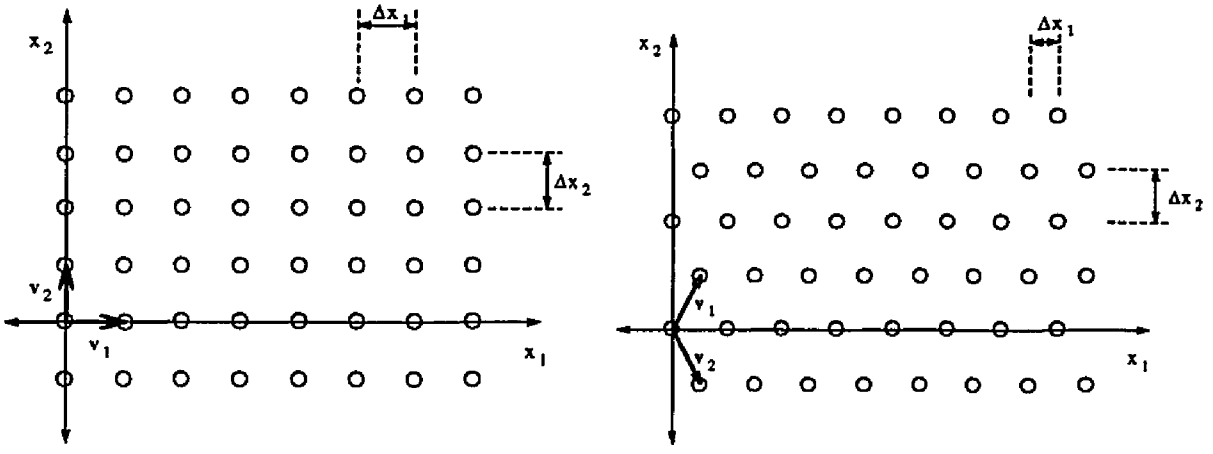

(a) Rectangular (b) Hexagonal

Figure 2.8: Sampling Lattice

As shown in figure 2.8 the location of doubly periodic sampling points in the (x_1, x_2) plane can be described in terms of two linearly independent vectors $\mathbf{v_1} = (v_{11}, v_{21})^T$ and $\mathbf{v_2} = (v_{12}, v_{22})^T$ [11,17], i.e.

$$\begin{aligned} x_1 &= v_{11}n_1 + v_{12}n_2 \\ x_2 &= v_{21}n_1 + v_{22}n_2 \end{aligned}$$

or in vector notation

$$\mathbf{x} = \mathbf{V}\mathbf{n} \tag{2.24}$$

where:

$$\mathbf{x} = \begin{bmatrix} x_1 \\ x_2 \end{bmatrix}$$

$$\mathbf{n} = \begin{bmatrix} n_1 \\ n_2 \end{bmatrix}$$

$$\mathbf{V} = [\mathbf{v_1}|\mathbf{v_2}] = \begin{bmatrix} v_{11} & v_{12} \\ v_{21} & v_{22} \end{bmatrix}$$

The 2-dimensional sampling function $\Psi(\mathbf{x})$ (a generalization of the 2-dimensional rectangular shah function) is defined as

$$\Psi(\mathbf{x}) \equiv \sum_{\mathbf{n}} \delta(\mathbf{x} - \mathbf{V}\mathbf{n}) \tag{2.25}$$

where the summation is over the sampling grid specified by the 2-dimensional integer column vector $\mathbf{n}$, and $\delta(\mathbf{x})$ is the 2-dimensional Dirac delta function.

The geometry of the sampling grid is determined by $\mathbf{v_1}$ and $\mathbf{v_2}$ as shown in figure 2.8(a) for rectangular sampling and 2.8(b) for hexagonal sampling. The matrix $\mathbf{V}$ acts as a transformation matrix for converting from the *normalized* sampling coordinate system with integer coordinates $\mathbf{n}$ to the reference orthogonal coordinate system $\mathbf{x}$. Because of this normalization, the sampling points are a unit distance apart in the sampling coordinate system. The rectangular sampling function described in equation 2.23 and shown in figure 2.8(a) is a special case of $\Psi(\mathbf{x})$ corresponding to

$$\mathbf{V} = \begin{bmatrix} \Delta x_1 & 0 \\ 0 & \Delta x_2 \end{bmatrix}. \tag{2.26}$$

Similarly, the hexagonal sampling function shown in figure 2.8(b) corresponds to

$$\mathbf{V} = \begin{bmatrix} \Delta x_1 & \Delta x_1 \\ -\Delta x_2 & \Delta x_2 \end{bmatrix}. \tag{2.27}$$

The sampling function $\Psi(\mathbf{x})$ is used by Ulichney [17] in his analysis of half-toning algorithms and corresponds to the 2-dimensional version of the general multidimensional sampling function presented by previous researchers [11,18–20]. An important property of the Ψ function is that its Fourier transform is a scaled version of itself [11,17], i.e.

$$\sum_{\mathbf{n}} \delta(\mathbf{x} - \mathbf{V}\mathbf{n}) \overset{\mathcal{F}}{\longleftrightarrow} \frac{1}{|\det \mathbf{V}|} \sum_{\mathbf{k}} \delta(\omega - \mathbf{U}\mathbf{k}) \tag{2.28}$$

where, again, ω is a real 2-dimensional column vector describing the frequency domain reference coordinate system (analogous to the spatial domain reference coordinate system

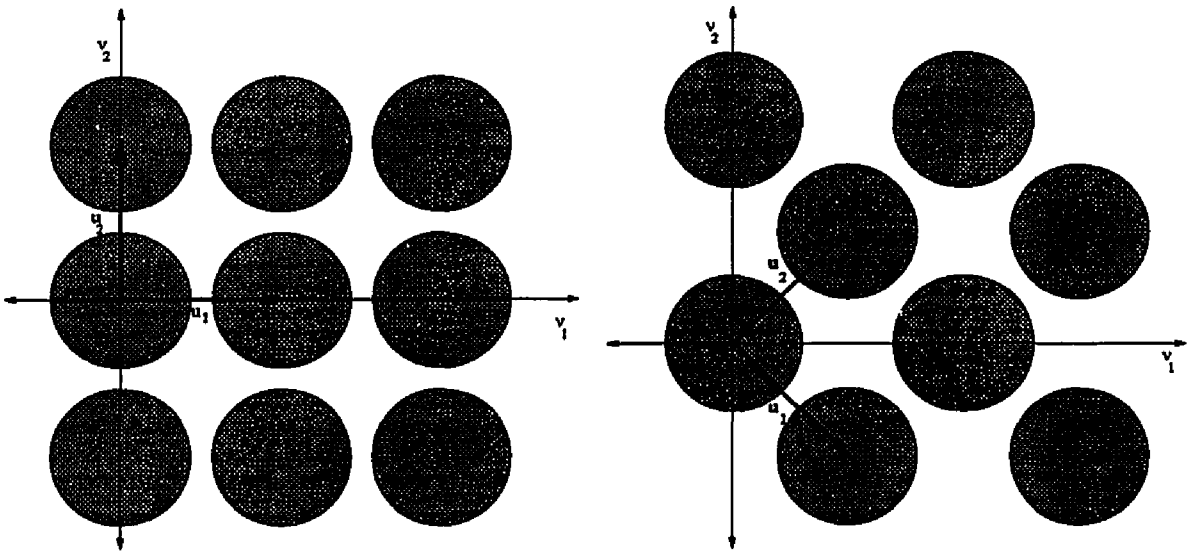

(a) Rectangular (b) Hexagonal

Figure 2.9: Periodic Baseband Replication

described by x), U is the frequency domain baseband replication (periodicity) matrix corresponding to the spatial domain sampling matrix V, i.e. $\mathbf{U} = (\mathbf{V}^T)^{-1}$, k is a 2-dimensional integer column vector, and $\sum_{\mathbf{k}}$ represents summation over the reciprocal frequency domain grid defined by U, where

$$\mathbf{U} = [\mathbf{u_1}|\mathbf{u_2}] = \begin{bmatrix} u_{11} & u_{12} \\ u_{21} & u_{22} \end{bmatrix} \tag{2.29}$$

This Fourier transform result is central in the following development of fidelity loss metrics.

The frequency domain baseband replication matrix U corresponding to the rectangular spatial sampling grid defined by equation 2.26 and shown in figure 2.8(a) is

$$\mathbf{U} = \begin{bmatrix} \frac{1}{\Delta x_1} & 0 \\ 0 & \frac{1}{\Delta x_2} \end{bmatrix}, \tag{2.30}$$

which is shown in figure 2.9(a). Similarly figure 2.9(b) shows the frequency domain baseband replication matrix for the hexagonal spatial sampling grid defined by equation 2.27, and shown in figure 2.8(b), where

$$\mathbf{U} = \begin{bmatrix} \frac{1}{2\Delta x_1} & \frac{1}{2\Delta x_1} \\ -\frac{1}{2\Delta x_2} & \frac{1}{2\Delta x_2} \end{bmatrix}. \tag{2.31}$$

Equation 2.28 shows the correspondence between the spatial domain sampling function and the frequency domain sampling function. Just as the matrix $\mathbf{V}$ determines the locations of the sampling points in the spatial domain, the matrix $\mathbf{U}$ determines the locations of the periodically replicated band-regions in the frequency domain. The relationship between the band-region of the formed image (the scene filtered by the image formation OTF) and the sampling density defined by $\mathbf{V}$, or equivalently the sampling passband defined by $\mathbf{U}$, determines if aliasing can occur. If the sampling density is greater than necessary for a given formed image band-region, as shown in figure 2.10(a), no aliasing will occur but some of the capabilities of the sampling density are wasted. This is called oversampling. If the sampling density is not great enough for the band-region, called undersampling and shown in figure 2.10(b), aliasing will occur. The degree of aliasing possible depends on the amount of overlap between adjacent band-regions. If the sampling density is just enough for the given band-region, as shown in figure 2.10(c), then no aliasing will occur. Sampling at this minimum sampling density is called sufficient sampling. In order to completely reconstruct an image from its sampled values, the image has to have been either over or sufficiently sampled. The point where two adjacent band-regions meet (halfway between the centers of the two band-regions) is often call the Nyquist limit or the Nyquist region.

2.4 Reconstruction

The reconstruction operation is the inverse of the image acquisition (optics and sampling) process in the sense that the sampled image $g[\mathbf{n}]$ is mapped from the discrete sampling coordinate space $\mathbf{n}$ to the continuous scene coordinate space via $\mathbf{x} - \mathbf{V}\mathbf{n}$ and the resulting image is filtered by the reconstruction function $r(\cdot)$ as shown in equation 2.32. The reconstruction operation is accomplished via convolution in the spatial domain, i.e.

$$s'(\mathbf{x}) = \sum_{\mathbf{n}}^{\mathbf{N}} r(\mathbf{x} - \mathbf{V}\mathbf{n}) g[\mathbf{n}] \tag{2.32}$$

or multiplication in the frequency domain

$$\hat{s}'[\boldsymbol{\nu}] = \hat{r}(\boldsymbol{\nu}^t \mathbf{N}^{-1}) \hat{g}[\boldsymbol{\nu}], \tag{2.33}$$

producing the reconstructed image $s'(\mathbf{x})$ or the Fourier series representation of the reconstructed image $\hat{s}'[\boldsymbol{\nu}]$. The reconstruction function $r(\cdot)$ can take many forms and is applicable to various (related) fields of study. Typically in a digital imaging system, the reconstruction operation is handled by the display device or the hard-copy output device, often referred to as the *display* reconstruction function. In other fields the reconstruction function is used to create a continuous function from its sampled data by interpolation. A reconstruction function that exactly recreates a sufficiently sampled continuous function from its sampled values is considered an *ideal* reconstruction function. Using a reconstruction or interpolation

functions that approximate the ideal reconstruction function, i.e. the infinite sinc(·) function, but which is finite in extent [21–25]. For the purposes of this dissertation two types of reconstruction functions are studied, the *ideal* reconstruction function and the *display* reconstruction function.

2.4.1 Ideal Reconstruction Function

An *ideal* reconstruction function exactly reproduces a band-limited, sufficiently sampled function from its sampled values. Petersen and Middleton [18] characterized the family of ideal reconstruction functions as those having a Fourier transform with a constant non-zero value over the base band-region of the sampled function, and with a value of zero wherever the periodically replicated band-regions of the sampled function are non-zero. For this dissertation, the ideal reconstruction functions for both the hexagonal and the rectangular sampling grids were defined in the frequency domain as having a constant, non-zero value over the sampling passband, and having a value of zero elsewhere. For the rectangular sampling grid the sampling passband was a square region as shown in figure 2.11. For the hexagonal sampling grid the sampling passband was a regular hexagon as shown in figure 2.12.

2.4.2 Display Reconstruction Function

In an actual digital imaging system, reconstruction of a digital image is accomplished by the display device, often a Cathode Ray Tube (CRT). Unfortunately the display device cannot accurately realize the ideal reconstruction function (which, in the spatial domain is a two-dimensional form of the sinc(·) function) due to the infinite extent of the sinc(·) function and the negative values present in the sinc(·) function [15]. A frequently used model for a CRT display device proposed by Schade [26], and used in simulations similar to this [8, 9], is the sum of two Gaussian-spot functions consisting of a strongly peaked central portion that represents the electron beam striking the phosphor, and a broad flare surrounding the central portion representing "the finite thickness of the phosphor and the optical reflections of the faceplate surfaces" [26] , i.e.

$$\hat{r}(\omega_1,\omega_2) = D_1 \exp\left(-\left(\frac{\sqrt{\omega_1^2+\omega_2^2}}{\alpha_1}\right)^2\right) + D_2 \exp\left(-\left(\frac{\sqrt{\omega_1^2+\omega_2^2}}{\alpha_2}\right)^2\right) \tag{2.34}$$

with $D_1 = 0.76, \alpha_1 = 0.4301484, D_2 = 0.24$, and $\alpha_2 = 0.0323814$. An example display transfer function is show in figure 2.13.

2.5 Summary

A continuous simulated scene $s(\mathbf{x})$ can be represented in terms of the Fourier series coefficients $C[\nu]$. The image formation operation is simulated by the continuous PSF (point spread function) $h(\mathbf{x})$, or its Fourier transform counterpart the continuous OTF (optical transfer function) $\hat{h}(\omega)$. The sampling operation digitizes the formed image $g(\mathbf{x})$, with one point in the sampled image representing an area of size $|\det \mathbf{V}|$ in the formed image. The reconstruction operation attempts to undo the sampling operation by interpolating the sampled values using $r(\mathbf{x})$ producing the reconstructed image $s'(\mathbf{x})$. The next chapter will describe the metrics used to measure the amount of fidelity loss occurring in the image formation, sampling, and reconstruction operations.

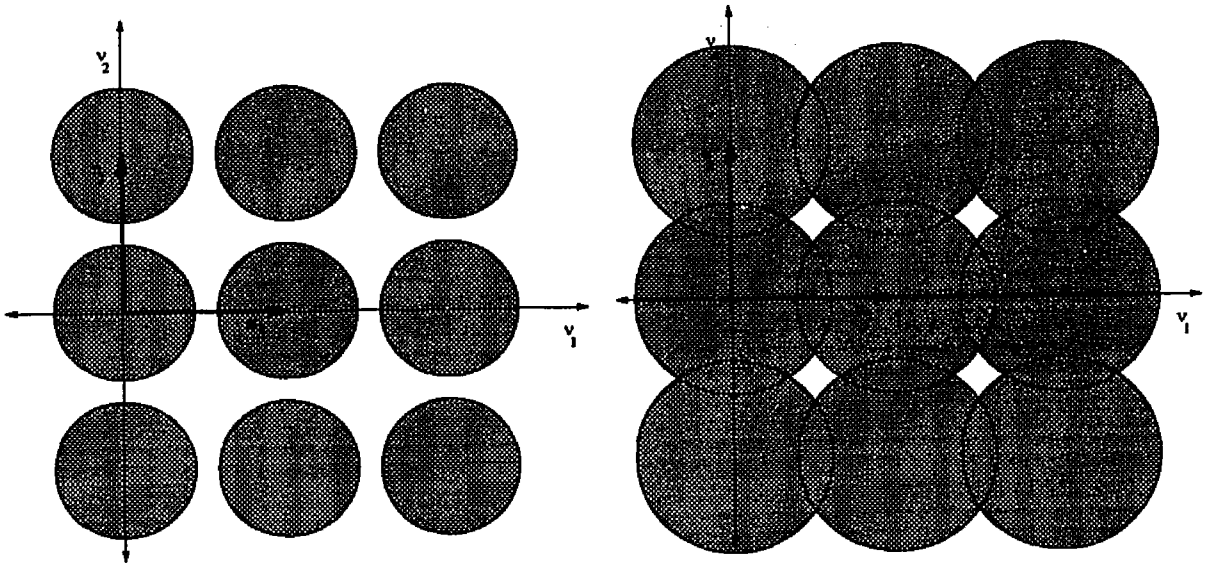

(a) Oversampling

(b) Undersampling

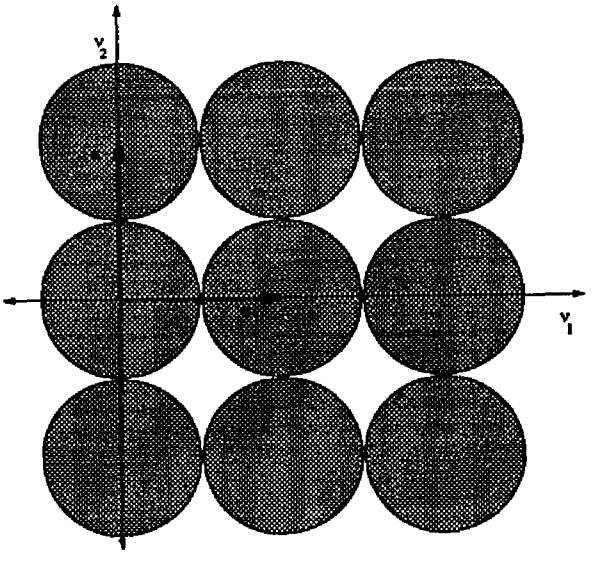

(c) Sufficient Sampling

Figure 2.10: Frequency Domain Sampling Regimes

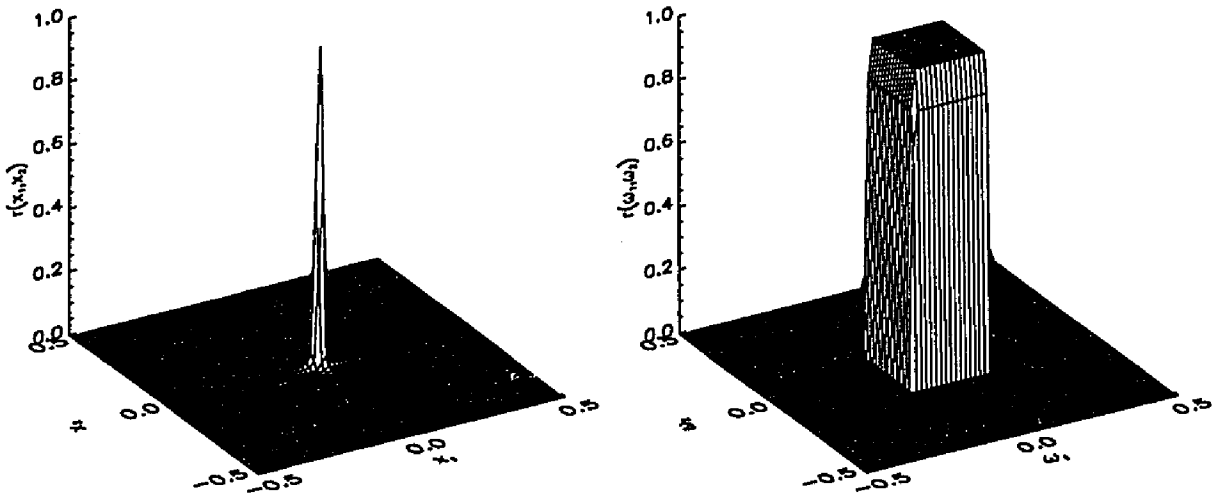

(a) Spatial Domain (PSF) (b) Frequency Domain (OTF)

Figure 2.11: Ideal Rectangular Reconstruction Function

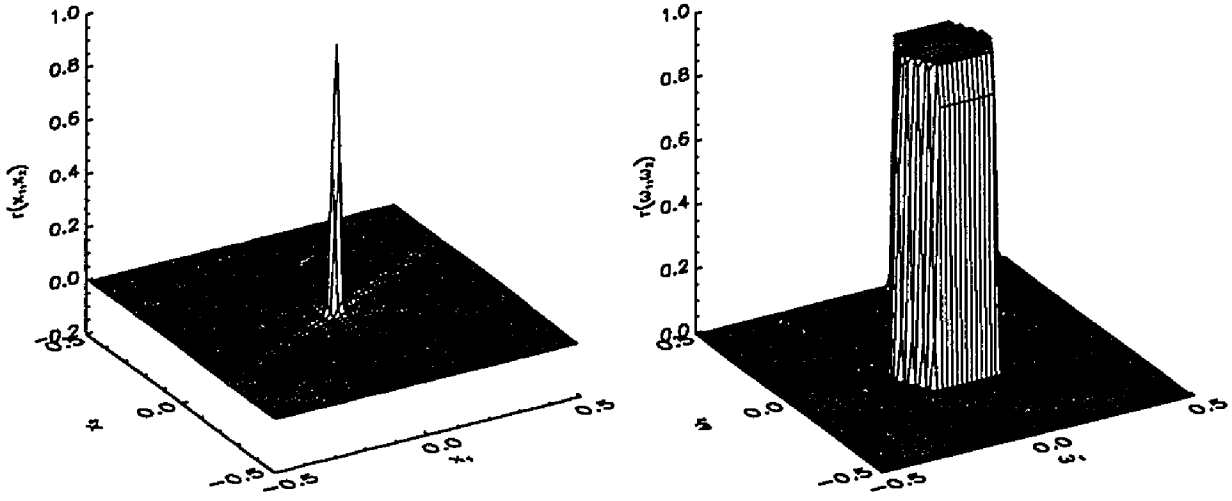

(a) Spatial Domain (PSF) (b) Frequency Domain (OTF)

Figure 2.12: Ideal Hexagonal Reconstruction Function

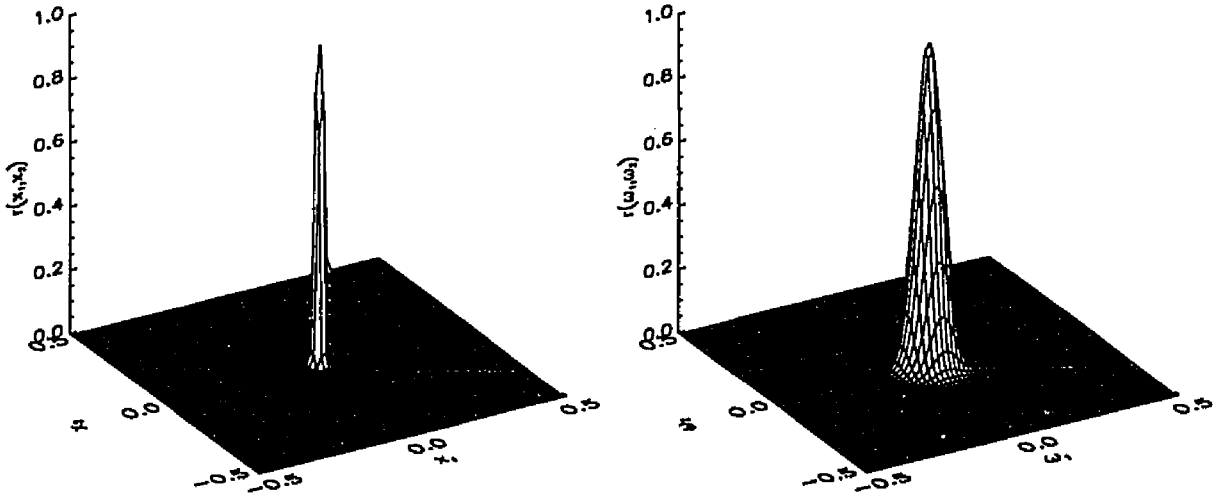

(a) Spatial Domain (PSF)

(b) Frequency Domain (OTF)

Figure 2.13: Display Optical Transfer Function

References

[1] Stephen K. Park. *Discrete Linear Systems.* Unpublished Lecture Notes (Computer Science Department, College of William and Mary), 1988.

[2] Stephen K. Park. Linear digital imaging system fidelity analysis. In *Visual Information Processing for Television and Telerobotics*, pages 3–10. NASA Conf. Pub. 3053, 1989.

[3] Stephen E. Reichenbach and Stephen K. Park. Computer generated scenes and simulated imaging. In *Optical Society of America Annual Meeting*, volume 11, page 170. OSA Technical Digest 11, 1988.

[4] Stephen K. Park. Image gathering, interpolation and restoration: A fidelity analysis. In *SPIE 1992 Technical Symposium on Visual Information Processing.* SPIE, 1992.

[5] John C. Burton, Stephen K. Park, and Keith W. Miller. Hexagonally sampled digital imaging system analysis. In *SPSE's 43rd Annual Conf.*, pages 238–241. SPSE, 1990.

[6] John C. Burton, Keith W. Miller, and Stephen K. Park. Fidelity metrics for hexagonally sampled digital imaging systems. *Journal of Imaging Technology*, 17(6):279–283, 1991.

[7] Stephen K. Park and Stephen E. Reichenbach. Digital image gathering and minimum mean-square error restoration. In *Visual Communications and Image Processing V*, pages 1578–1589. Proc. SPIE 1360, 1990.

[8] Stephen E. Reichenbach. *Small-Kernel Image Restoration.* PhD thesis, College of William and Mary, July 1989.

[9] Stephen E. Reichenbach, Stephen K. Park, Rachel Alter-Gartenberg, and Zia-ur Rahman. Artificial scenes and simulated imaging. In *Stochastic and Neural Methods in Signal Processing, Image Processing, and Computer Vision*, volume 1569, pages 422–433. SPIE, 1991.

[10] Stephen K. Park and Robert A. Schowengerdt. Image sampling, reconstruction, and the effect of sample-scene phasing. *Applied Optics*, 21(17):3142–3151, 1982.

[11] Dan E. Dudgeon and Russell M. Mersereau. *Multidimensional Digital Signal Processing.* Prentice-Hall, Englewood Cliffs, NJ, 1984.

[12] H. Joseph Weaver. *Applications of Discrete and Continuous Fourier Analysis.* John Wiley and Sons, New York, NY, 1983.

[13] Ronald N. Bracewell. *The Fourier Transform and Its Applications.* McGraw-Hill, New York, NY, revised second edition, 1986.

[14] Alan V. Oppenheim, Alan S. Willsky, and Ian T. Young. *Signals and Systems.* Prentice-Hall, Englewood Cliffs, NJ, 1983.

[15] H. C. Andrews and B. R. Hunt. *Digital Image Restoration.* Prentice-Hall, Englewood Cliffs, NJ, 1977.

[16] William K. Pratt. *Digital Image Processing.* John Wiley and Sons, New York, NY, 1978.

[17] Robert Ulichney. *Digital Halftoning.* MIT Press, Cambridge, MA, 1987.

[18] Daniel P. Petersen and David Middleton. Sampling and reconstruction of wave-number-limited functions in n-dimensional euclidean spaces. *Information and Control*, 5(4):279–323, 1962.

[19] Russell M. Mersereau and Theresa C. Speake. The processing of periodically sampled multidimensional signal. *IEEE Transactions on Acoustics, Speech, and Signal Processing*, 31(5):188–194, 1983.

[20] Kwan F. Cheung and Robert J. Marks. Image sampling below the nyquist density without aliasing. *Journal of the Optical Society of America A*, 7(1):92–105, 1990.

[21] Robert H. Norton and Reinhard Beer. New apodizing functions for Fourier spectrometry. *Journal of the Optical Society of America*, 66(3):259–264, 1976.

[22] Jae H. Park. Effect of interferogram smearing on atmospheric limb sounding by Fourier transform spectroscopy. *Applied Optics*, 21(8):1356–1366, 1982.

[23] John E. Bertie. Apodization and phase correction. In J. R. Durig, editor, *Analytical Applications of FT-IR to Molecular and Biological Systems*, pages 25–50. D. Reidel Publishing, 1980.

[24] Stephen K. Park and Robert A. Schowengerdt. Image reconstruction by parametric cubic convolution. *Computer Vision, Graphics, and Image Processing*, 23:258–272, 1983.

[25] Robert Schowengerdt, Stephen K. Park, and Robert Gray. Topics in the two-dimensional sampling and reconstruction of images. *International Journal of Remote Sensing*, 5(2):333–347, 1984.

[26] Sr. Schade, Otto H. Image reproduction by a line raster process. In Lucien M. Biberman, editor, *Perception of Displayed Information*, chapter 6, pages 233–278. Plenum Press, New York, NY, 1973.

Chapter 3

Fidelity Loss Metrics

This chapter provides a mathematical framework for analyzing image fidelity losses in hexagonally and rectangularly sampled digital imaging systems. These losses are due to blurring during image formation, aliasing due to undersampling, and imperfect reconstruction. The analysis of the individual and combined effects of these losses is based upon the idealized (noiseless) continuous/discrete/continuous imaging system model described in chapter 2. The following development of the fidelity loss metrics was previously presented by the author in [2].

Quantification of the image fidelity losses is accomplished via three mean–squared–error (MSE) metrics: *imaging fidelity loss*, *sampling and reconstruction fidelity loss*, and *end–to–end fidelity* loss. Sub–pixel shift–variant sampling effects are accounted for with an expected value analysis. These image fidelity loss metrics [1, 2] are an extension of the image fidelity analysis by Park, et.al. for a 1-dimensional sampled imaging system [3, 4] and a normalized rectangular 2-dimensional sampled imaging system [5, 6]. The extension accounts for both hexagonal and rectangular sampling grids as special cases. This extension is based on the work by Mersereau [7, 8] and Ulichney [9] concerning generalized sampling grids. The three generalized fundamental fidelity loss metrics are shown in figure 3.1.

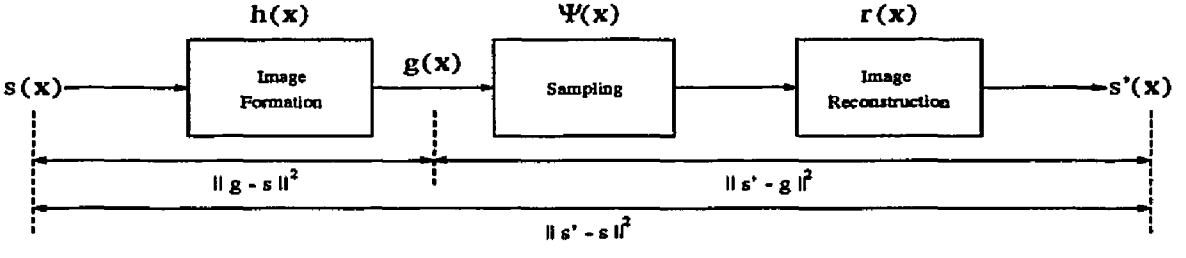

Figure 3.1: Digital Imaging System Model

Imaging fidelity loss ($\|s - g\|^2$) measures the loss of fidelity during image gathering.

Sampling/reconstruction fidelity loss ($\|g - s'\|^2$) measures the loss of fidelity caused by undersampling (aliasing) and imperfect reconstruction. End-to-end fidelity loss ($\|s - s'\|^2$) measures the net loss of fidelity caused by the combined effects of image gathering, sampling, and reconstruction. The use of the MSE metric in the development of the fidelity loss metrics provides an easy transition from the spatial domain to the frequency domain via Parseval's energy theorem.

3.1 Imaging fidelity loss

Consistent with equation (3.1), the image gathering component of the system model is considered to be a linear, shift-invariant process characterized by spatial domain convolution. Equivalently, in the frequency domain image gathering is characterized by multiplication; $\hat{g}(\omega) = \hat{h}(\omega)\hat{s}(\omega)$ where $\hat{g}$, $\hat{h}$, and $\hat{s}$ are the Fourier transforms of g, h, and s respectively.

Imaging fidelity loss is defined as

$$\|s - g\|^2 = \int_{\mathbf{x}} [s(\mathbf{x}) - g(\mathbf{x})]^2 \, d\mathbf{x}. \tag{3.1}$$

Applying Parseval's theorem to (3.1) we find that

$$\begin{aligned} \|s - g\|^2 &= \int_{\omega} |\hat{s}(\omega) - \hat{g}(\omega)|^2 d\omega \\ &= \int_{\omega} |1 - \hat{h}(\omega)|^2 |\hat{s}(\omega)|^2 d\omega. \end{aligned} \tag{3.2}$$

The integrals $\int_{\mathbf{x}}$ and $\int_{\omega}$ are over all $\mathbf{x}$ and ω respectively.

Equation (3.2) provides significant insight into the image gathering operation.

- Imaging fidelity loss is significant if and only if there is significant scene energy $|\hat{s}(\omega)|^2$ at frequencies ω where $\hat{h}(\omega)$ is significantly different from 1.
- $\hat{h}(\omega)$ typically acts as a low pass filter, decreasing in magnitude from 1 at low frequencies to 0 at high frequencies. Thus imaging fidelity loss is caused by the suppression of higher frequencies.
- Since most natural scenes are not band-limited (i.e. natural scenes typically have energy at all frequencies) and since $\hat{h}(\omega)$ acts as a low pass filter, some imaging fidelity loss is inevitable.

The fact that these well-known observations can be deduced from a single equation emphasizes the utility of the imaging fidelity loss metric, equation (3.2). The remainder of this chapter describes the development of similar equations for sampling/reconstruction fidelity loss and end-to-end fidelity loss.

3.2 Sample/scene phase averaging

Consistent with equation (3.2), the sampling component of the imaging system in figure 3.1 is modelled as a grid of regularly spaced discrete sample locations. The distance between two adjacent sample locations in a 1-dimensional grid is the *sampling interval.* One dimensional sampling is shift-invariant only when the shift is by an integer number of sampling intervals. For sub-interval shifts, the sampled image varies periodically with the sample/scene phase, with a period of one sampling interval [4]. (Sample/scene phase describes the position of a point in the scene relative to the sampling grid.) The concept of sample/scene phase was extended to a 2-dimensional normalized rectangular sampling grid in previous work [5, 6]. This chapter (and [2]) further extends the concept to include a generalized sampling grid.

The area between adjacent sample locations in a generalized 2-dimensional sampling grid is the *sampling cell* as shown in figures 3.2(b) and 3.2(a). These cells completely tessellate the sampling plane. Analogous to the 1-dimensional case, 2-dimensional sampling is shift-invariant only when the shift is by an integer number of sampling cells. For sub-cell shifts, the sampled image varies periodically with the sample/scene phase, with the (2-dimensional) period being one sampling cell. The phase between the the sampling grid and the scene is modeled as a uniformly distributed random variable (i.e. all phases have an equal probability of occurring), hence the *expected* value of the sample/scene phase (and consequently the *expected* values of sampling and reconstruction fidelity loss, and end-to-end fidelity loss) are obtained by averaging over one phase period (one sampling grid cell). The area of the sampling cell is 1 when measured with respect to the normalized sampling coordinate system and equal to $|\det \mathbf{V}|$ when measured relative to the reference orthogonal coordinate system.

Sample/scene phase averaging is used to account for shift-variance in the formulation of sampling and reconstruction fidelity loss and end-to-end fidelity loss. Conceptually sample/scene phase averaging is accomplished via the following procedure:

- Shift the input scene $s(\mathbf{x})$ by an amount $\mathbf{z}$ relative to the sampling grid defined by $\mathbf{V}$ i.e. $s(\mathbf{x}) \longrightarrow s(\mathbf{x} - \mathbf{V}\mathbf{z})$.
- Generate the shifted pre-sampling image $g(\mathbf{x} - \mathbf{V}\mathbf{z})$ and the shifted reconstructed image $s'(\mathbf{x}\,; \mathbf{V}\mathbf{z}) = [g(\mathbf{x} - \mathbf{V}\mathbf{z})\Psi(\mathbf{x})] * r(\mathbf{x})$ based on the shifted scene.
- Calculate the appropriate fidelity loss metrics ($\|g - s'\|^2$ and $\|s - s'\|^2$) for the shifted images.
- Repeat the first three steps for different values of $\mathbf{z}$, then average to determine *expected* values for $\|g - s'\|^2$ and $\|s - s'\|^2$.

This procedure is the basis for the definitions of sampling/reconstruction fidelity loss and

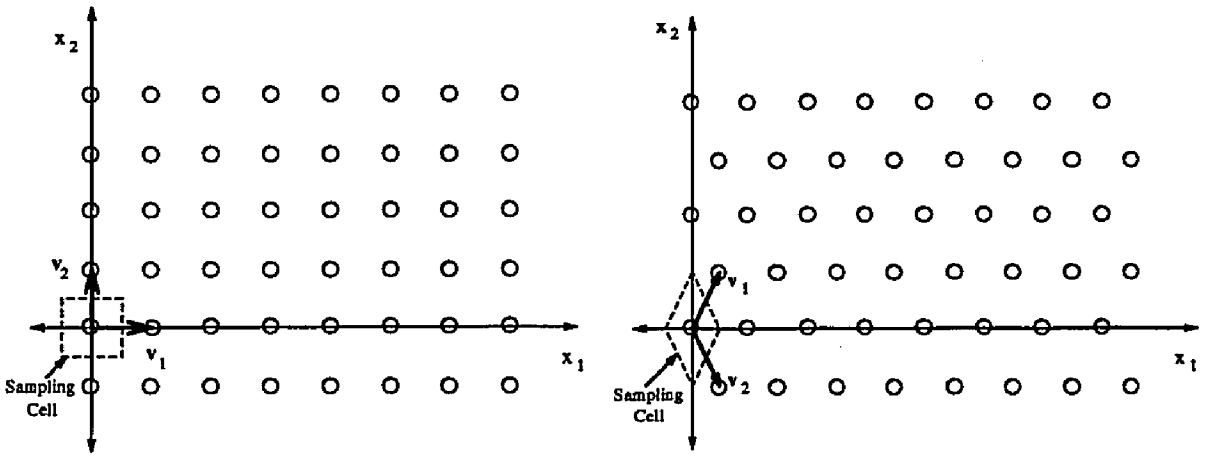

(a) Rectangular (b) Hexagonal

Figure 3.2: Sampling Grid

end-to-end fidelity loss given by equations (3.3) and (3.4) respectively.

$$E\left[\|g - s'\|^2\right] = \int_{\mathbf{z}} \|g - s'\|^2 dz \tag{3.3}$$

$$E\left[\|s - s'\|^2\right] = \int_{\mathbf{z}} \|s - s'\|^2 dz \tag{3.4}$$

where

$$\int_{\mathbf{z}} (\cdot)\, dz = \int_{-\frac{1}{2}}^{\frac{1}{2}} \int_{-\frac{1}{2}}^{\frac{1}{2}} (\cdot)\, dz_1\, dz_2 \tag{3.5}$$

is the expected value integral over one cell in the sampling grid. Since we have assumed that the image gathering operation is shift-invariant, the expected value of imaging fidelity loss is equal to the actual imaging fidelity loss, i.e. $E\left[\|s - g\|^2\right] = \|s - g\|^2$.

3.3 Sampling/reconstruction fidelity loss

Sampling/reconstruction fidelity loss is the *mean-square* difference between the pre-sampling image $g(\mathbf{x})$ and the reconstructed image $s'(\mathbf{x})$ defined as

$$E\left[\|g - s'\|^2\right] = \int_{\mathbf{z}} \int_{\mathbf{x}} \left[g(\mathbf{x} - \mathbf{V}\mathbf{z}) - s'(\mathbf{x}\,;\mathbf{V}\mathbf{z})\right]^2 d\mathbf{x}\, dz. \tag{3.6}$$

In order to apply Parseval's theorem to equation (3.6) (as was done in the development of the imaging fidelity loss equation (3.2)) we need the frequency domain representation of

$[g(\mathbf{x}-\mathbf{Vz})-s'(\mathbf{x};\mathbf{Vz})]$ which can be determined from

$$g(\mathbf{x}-\mathbf{Vz}) \overset{\mathcal{F}}{\longleftrightarrow} \hat{g}(\omega)\exp\left(-\imath 2\pi\omega^{\mathrm{T}}\mathbf{Vz}\right) \tag{3.7}$$

$$s'(\mathbf{x};\mathbf{Vz}) \overset{\mathcal{F}}{\longleftrightarrow} \frac{\hat{r}(\omega)}{|\det\mathbf{V}|}\sum_{\mathbf{k}}\hat{g}(\omega-\mathbf{Uk})\exp\left(-\imath 2\pi(\omega-\mathbf{Uk})^{\mathrm{T}}\mathbf{Vz}\right). \tag{3.8}$$

Combining equations (3.7) and (3.8) we obtain

$$[g(\mathbf{x}-\mathbf{Vz})-s'(\mathbf{x};\mathbf{Vz})] \overset{\mathcal{F}}{\longleftrightarrow} \tag{3.9}$$
$$\exp(-\imath 2\pi\omega^{\mathrm{T}}\mathbf{Vz})\sum_{\mathbf{k}}\left[\delta_{\mathbf{k}}-\frac{\hat{r}(\omega)}{|\det\mathbf{V}|}\right]\hat{g}(\omega-\mathbf{Uk})\exp(\imath 2\pi(\mathbf{Uk})^{\mathrm{T}}\mathbf{Vz})$$

where:

$$\delta_{\mathbf{k}} = \begin{cases} 1 & \text{for } \mathbf{k} = \begin{bmatrix} 0 \\ 0 \end{bmatrix} \\ 0 & \text{otherwise} \end{cases} \tag{3.10}$$

Recalling that $\mathbf{U} = (\mathbf{V}^T)^{-1}$ allows us to express sampling and reconstruction fidelity loss as

$$E\left[\|g-s'\|^2\right] = \int_{\mathbf{z}}\int_{\omega}\left|\exp\left(-\imath 2\pi\omega^{\mathrm{T}}\mathbf{Vz}\right)\sum_{\mathbf{k}}\left[\delta_{\mathbf{k}}-\frac{\hat{r}(\omega)}{|\det\mathbf{V}|}\right]\right.$$
$$\left.\times\,\hat{g}(\omega-\mathbf{Uk})\exp\left(\imath 2\pi\mathbf{k}^{\mathrm{T}}\mathbf{z}\right)\right|^2 d\omega\,d\mathbf{z} \tag{3.11}$$

$$\vdots$$

$$= \int_{\omega}\sum_{\mathbf{k}}\sum_{\mathbf{k}'}\left[\delta_{\mathbf{k}}-\frac{\hat{r}(\omega)}{|\det\mathbf{V}|}\right]\left[\delta_{\mathbf{k}'}-\frac{\hat{r}^*(\omega)}{|\det\mathbf{V}|}\right]$$
$$\times\hat{g}(\omega-\mathbf{Uk})\hat{g}^*(\omega-\mathbf{Uk}')\mathrm{sinc}\,(\mathbf{k}-\mathbf{k}')\,d\omega \tag{3.12}$$

where the $*$ superscript indicates the complex conjugate. Equation (3.12) can be separated into two parts based on possible values of $\mathbf{k}$ and $\mathbf{k}'$ (and recalling that $\hat{g}(\omega)=\hat{h}(\omega)\hat{s}(\omega)$)

$$E\left[\|g-s'\|^2\right] = \epsilon_r^2+\epsilon_s^2 \tag{3.13}$$

where:

$$\epsilon_r^2 = \int_{\omega}\left|1-\frac{\hat{r}(\omega)}{|\det\mathbf{V}|}\right|^2\left|\hat{h}(\omega)\hat{s}(\omega)\right|^2 d\omega \tag{3.14}$$

$$\epsilon_s^2 = \int_{\omega}\left|\frac{\hat{r}(\omega)}{|\det\mathbf{V}|}\right|^2\sum_{\mathbf{k}\neq\mathbf{0}}\left|\hat{h}(\omega-\mathbf{Uk})\hat{s}(\omega-\mathbf{Uk})\right|^2 d\omega. \tag{3.15}$$

Equations (3.13), (3.14) and (3.15) are analogous to equation (3.2) and provide the following insight.

- $\hat{r}(\omega)$ is a low pass filter with value $|\det \mathbf{V}|$ at zero frequency.
- The term ϵ_r^2 accounts for loss of image fidelity due to imperfect reconstruction. It measures the fidelity loss caused by the presence of significant image energy $|\hat{h}(\omega)\hat{s}(\omega)|^2$ at frequencies where $\hat{r}(\omega) \neq |\det \mathbf{V}|$.
- The term ϵ_s^2 accounts for loss of image fidelity due to aliasing caused by undersampling. It measures the fidelity loss caused by the folding of significant image energy at frequencies beyond the Nyquist limit into lower frequencies where $\hat{r}(\omega) \neq 0$.
- The sum $\epsilon_r^2 + \epsilon_s^2 = 0$ defines the conditions under which complete reconstruction of the pre-sampling image ($g(\mathbf{x})$) from its sampled data is possible. Complete reconstruction can occur only when both ϵ_r^2 and ϵ_s^2 are simultaneously zero since both quantities are non-negative. The conditions required for complete reconstruction are:
  1. $\hat{r}(\omega)$ must equal $|\det \mathbf{V}|$ over the region where the band-region of the pre-sampling image contains energy ($\hat{h}(\omega)\hat{s}(\omega) \neq 0$).
  2. $\hat{r}(\omega)$ must equal zero over the region where the instances of the periodic extension of $\hat{g}(\omega)$ contain energy ($\hat{h}(\omega - \mathbf{Uk})\hat{s}(\omega - \mathbf{Uk}) \neq 0$).
  3. The sampling matrix $\mathbf{V}$ (and hence the periodicity matrix $\mathbf{U}$) must be defined such that adjacent instances of the periodic extension of $\hat{g}(\omega)$ do not overlap.

  These conditions are equivalent to the conditions presented by Petersen and Middleton [10] for a universal reconstruction function which will reproduce any function that is band-limited to a given band-region.

3.4 End-to-End Fidelity Loss

End-to-end fidelity loss is the *mean-square* difference between the original scene $s(\mathbf{x})$ and the reconstructed image $s'(\mathbf{x})$ and is defined as

$$E\left[\|s - s'\|^2\right] = \int_{\mathbf{z}}\int_{\omega} \left[s(\mathbf{x} - \mathbf{Vz}) - s'(\mathbf{x}\,;\mathbf{Vz})\right]^2 d\mathbf{x}\, d\mathbf{z}. \tag{3.16}$$

In a development strictly analogous to that of equation (3.9) we find that

$$\begin{aligned}&[s(\mathbf{x} - \mathbf{Vz}) - s'(\mathbf{x}\,;\mathbf{Vz})] \xleftrightarrow{\mathcal{F}} \\ &\quad \exp\left(-\imath 2\pi\omega^{\mathrm{T}}\mathbf{Vz}\right) \sum_{\mathbf{k}} \left[\delta_{\mathbf{k}} - \frac{\hat{r}(\omega)}{|\det \mathbf{V}|}\hat{h}(\omega - \mathbf{Uk})\right] \hat{s}(\omega - \mathbf{Uk}) \exp\left(\imath 2\pi(\mathbf{Uk})^{\mathrm{T}}\mathbf{Vz}\right).\end{aligned} \tag{3.17}$$

Again, in a development strictly analogous to that of equation (3.12) we see

$$E\left[\|s-s'\|^2\right] = \int_\omega \sum_{\mathbf{k}} \sum_{\mathbf{k}'} \left[\delta_{\mathbf{k}} - \frac{\hat{r}(\omega)}{|\det \mathbf{V}|}\hat{h}(\omega - \mathbf{U}\mathbf{k})\right] \tag{3.18}$$

$$\times \left[\delta_{\mathbf{k}'} - \frac{\hat{r}^*(\omega)}{|\det \mathbf{V}|}\hat{h}^*(\omega - \mathbf{U}\mathbf{k})\right] \hat{s}(\omega - \mathbf{U}\mathbf{k})\hat{s}^*(\omega - \mathbf{U}\mathbf{k}')\mathrm{sinc}\,(\mathbf{k}-\mathbf{k}')\,d\omega. \tag{3.19}$$

Equation (3.18) can be separated into two parts

$$E\left[\|s-s'\|^2\right] = \epsilon_e^2 + \epsilon_s^2 \tag{3.20}$$

where ϵ_s^2 is given in equation (3.15) and

$$\epsilon_e^2 = \int_\omega \left|1 - \frac{\hat{r}(\omega)}{|\det \mathbf{V}|}\hat{h}(\omega)\right|^2 |\hat{s}(\omega)|^2\,d\omega \tag{3.21}$$

Equations (3.20) and (3.21) provide the following additional insight.

- The term ϵ_e^2 accounts for the end–to–end loss of fidelity caused by significant scene energy $|\hat{s}(\omega)|^2$ at frequencies where the cascaded response $\hat{r}(\omega)\hat{h}(\omega) \neq |\det \mathbf{V}|$.
- ϵ_e^2 measures how well the reconstruction function $\hat{r}(\omega)$ is able to restore the frequencies that were suppressed prior to sampling by the image gathering function $\hat{h}(\omega)$.
- Analogous to the individual terms for sampling/reconstruction fidelity loss ϵ_e^2 and ϵ_s^2 are both non-negative quantities. In order to have zero end-to-end fidelity loss, both ϵ_e^2 and ϵ_s^2 must be simultaneously zero.
- The sum $\epsilon_e^2 + \epsilon_s^2 = 0$ defines the conditions necessary for complete reconstruction of the original scene $s(\mathbf{x})$ to occur.
  1. The cascaded response $\hat{r}(\omega)\hat{h}(\omega)$ must equal $|\det \mathbf{V}|$ over the region where the band-region of the original scene contains energy ($\hat{s}(\omega) \neq 0$).
  2. $\hat{r}(\omega)$ must equal zero over the region where the instances of the periodic extension of $\hat{g}(\omega)$ contain energy ($\hat{h}(\omega - \mathbf{U}\mathbf{k})\hat{s}(\omega - \mathbf{U}\mathbf{k}) \neq 0$).
  3. The sampling matrix $\mathbf{V}$ (and hence the periodicity matrix $\mathbf{U}$) must be defined such that adjacent instances of the periodic extension of $\hat{g}(\omega)$ do not overlap.

3.5 Fidelity Loss Budget

The three fundamental fidelity loss metrics; imaging fidelity loss, sampling/reconstruction fidelity loss, and end-to-end fidelity loss, can be expressed in terms of four quantities ϵ_i^2, ϵ_s^2,

ϵ_r^2, and ϵ_e^2. These fidelity loss metrics can be summarized by the fidelity loss budget given below.

$$E\left[\|s-g\|^2\right] = \epsilon_i^2 \tag{3.22}$$

$$E\left[\|g-s'\|^2\right] = \epsilon_s^2 + \epsilon_r^2 \tag{3.23}$$

$$E\left[\|s-s'\|^2\right] = \epsilon_s^2 + \epsilon_e^2 \tag{3.24}$$

where:

$$\epsilon_i^2 = \int_\omega \left|1-\hat{h}(\omega)\right|^2 |\hat{s}(\omega)|^2\, d\omega \tag{3.25}$$

$$\epsilon_e^2 = \int_\omega \left|1-\frac{\hat{r}(\omega)}{|\det \mathbf{V}|}\hat{h}(\omega)\right|^2 |\hat{s}(\omega)|^2\, d\omega \tag{3.26}$$

$$\epsilon_r^2 = \int_\omega \left|1-\frac{\hat{r}(\omega)}{|\det \mathbf{V}|}\right|^2 \left|\hat{h}(\omega)\hat{s}(\omega)\right|^2 d\omega \tag{3.27}$$

$$\epsilon_s^2 = \int_\omega \left|\frac{\hat{r}(\omega)}{|\det \mathbf{V}|}\right|^2 \sum_{\mathbf{k}\neq 0} \left|\hat{h}(\omega-\mathbf{Uk})\hat{s}(\omega-\mathbf{Uk})\right|^2 d\omega. \tag{3.28}$$

The four ϵ^2 terms can be readily calculated based on a knowledge of the input scene, the image gathering point spread function, the sampling grid geometry, and the reconstruction function. The four ϵ^2 terms are interrelated and any attempt to minimize one could potentially increase the others. For example, reducing the amount of aliasing present in a sampled image (reducing ϵ_s^2) by defocussing the pre-sampling image (i.e. by decreasing the passband of $\hat{h}(\omega)$) would increase the fidelity loss due to image formation (ϵ_i^2) and the fidelity loss due to the inability of the reconstruction function to restore the frequencies suppressed by defocussing (ϵ_e^2). Equations (3.25) - (3.28) explicitly quantify these interdependencies.

3.6 Application to Periodic Scenes

The preceding theoretical development of the generalized fidelity loss metrics assumes that the input scene is a continuous *aperiodic* function, whose Fourier transform is itself a continuous aperiodic function. Parseval's equation for a continuous aperiodic function is

$$\|s\|^2 = \int_\omega |\hat{s}(\omega)|^2 d\omega.$$

This results in the continuous integral form of the fidelity loss metrics given in equations 3.25) - (3.28. While this form is valuable for theoretical developments, it does not lend itself well to implementation on a digital computer.

A simplifying assumption made in the previous chapter is that the input scene is a continuous *periodic* function. The Fourier transform of a continuous periodic function is a

discrete aperiodic sequence, with Parseval's equation being defined as

$$\|s\|^2 = \sum_{\nu} |\hat{s}[\nu]|^2.$$

This form of Parseval's equation results in the discrete form of the fidelity loss metrics shown below in equations 3.32 – 3.35.

$$E\left[\|s-g\|^2\right] = \epsilon_i^2 \tag{3.29}$$

$$E\left[\|g-s'\|^2\right] = \epsilon_s^2 + \epsilon_\tau^2 \tag{3.30}$$

$$E\left[\|s-s'\|^2\right] = \epsilon_s^2 + \epsilon_e^2 \tag{3.31}$$

where:

$$\epsilon_i^2 = \sum_{\nu} \left|1 - \hat{h}[\nu]\right|^2 |\hat{s}[\nu]|^2 \tag{3.32}$$

$$\epsilon_e^2 = \sum_{\nu} \left|1 - \frac{\hat{r}[\nu]}{|\det \mathbf{V}|}\hat{h}[\nu]\right|^2 |\hat{s}[\nu]|^2 \tag{3.33}$$

$$\epsilon_\tau^2 = \sum_{\nu} \left|1 - \frac{\hat{r}[\nu]}{|\det \mathbf{V}|}\right|^2 \left|\hat{h}[\nu]\hat{s}[\nu]\right|^2 \tag{3.34}$$

$$\epsilon_s^2 = \sum_{\nu} \left|\frac{\hat{r}[\nu]}{|\det \mathbf{V}|}\right|^2 \sum_{\mathbf{k}\neq\mathbf{0}} \left|\hat{h}[\nu - \mathbf{Uk}]\hat{s}[\nu - \mathbf{Uk}]\right|^2. \tag{3.35}$$

and recalling from chapter that $\omega = \nu^t \mathbf{N}^{-1}$:

$$\hat{h}[\nu] = \hat{h}(\nu^t \mathbf{N}^{-1}) \tag{3.36}$$

$$\hat{r}[\nu] = \hat{r}(\nu^t \mathbf{N}^{-1}) \tag{3.37}$$

These discrete fidelity loss metrics can be directly implemented on a digital computer, facilitating the simulations detailed in the following chapters.

References

[1] John C. Burton, Stephen K. Park, and Keith W. Miller. Hexagonally sampled digital imaging system analysis. In *SPSE's 43rd Annual Conf.*, pages 238–241. SPSE, 1990.

[2] John C. Burton, Keith W. Miller, and Stephen K. Park. Fidelity metrics for hexagonally sampled digital imaging systems. *Journal of Imaging Technology*, 17(6):279–283, 1991.

[3] Stephen K. Park and Stephen E. Reichenbach. Digital image gathering and minimum mean-square error restoration. In *Visual Communications and Image Processing V*, pages 1578–1589. Proc. SPIE 1360, 1990.

[4] Stephen K. Park and Robert A. Schowengerdt. Image sampling, reconstruction, and the effect of sample-scene phasing. *Applied Optics*, 21(17):3142–3151, 1982.

[5] Stephen K. Park. Linear digital imaging system fidelity analysis. In *Visual Information Processing for Television and Telerobotics*, pages 3–10. NASA Conf. Pub. 3053, 1989.

[6] Stephen K. Park, Robert A. Schowengerdt, and Mary-Anne Kaczynski. Modulation-transfer-function analysis for sampled image systems. *Applied Optics*, 23(15):2572–2582, 1984.

[7] Dan E. Dudgeon and Russell M. Mersereau. *Multidimensional Digital Signal Processing.* Prentice-Hall, Englewood Cliffs, NJ, 1984.

[8] Russell M. Mersereau and Theresa C. Speake. The processing of periodically sampled multidimensional signal. *IEEE Transactions on Acoustics, Speech, and Signal Processing*, 31(5):188–194, 1983.

[9] Robert Ulichney. *Digital Halftoning.* MIT Press, Cambridge, MA, 1987.

[10] Daniel P. Petersen and David Middleton. Sampling and reconstruction of wave-number-limited functions in n-dimensional euclidean spaces. *Information and Control*, 5(4):279–323, 1962.

Chapter 4

Experimental Results - Band-limited Scenes

4.1 Implementation Details

The end–to–end model of a digital imaging system described in chapter 2 is based on the use of a Fourier series to describe a continuous scene and reconstructed image in the spatial domain. The imaging optical transfer functions and the reconstruction functions were described as continuous in both the spatial and frequency domain. To implement a simulation based on this model, several approximations are made. Primarily, the imaging OTFs and the reconstruction functions are specified in the frequency domain as two-dimensional discrete functions, i.e. $\hat{h}[\nu]$ and $\hat{r}[\nu]$. The fidelity loss metrics developed in chapter 3 based on the imaging system model described in chapter 2 are also modified slightly to allow for discrete implementation. The discrete representation of the scene, reconstructed image and various transfer functions necessitates the use of summations instead of integrals in the implementation of the fidelity loss metrics. One implementational restriction is that for the indexing function $\nu - \mathrm{Uk}$, U (and hence V) must be defined such that the indexing function yields integer coordinate values in order to properly access the data in the arrays holding the Fourier series coefficients for scene, $\hat{s}[\nu - \mathrm{Uk}]$, and the imaging OTF, $\hat{h}[\nu - \mathrm{Uk}]$. The precise definitions of the imaging OTFs, the reconstruction functions, and the fidelity loss metrics used in the simulation are presented in the following sections.

4.2 Experimental Design

The series of experiments presented in this chapter were designed to investigate the concepts and questions presented in chapter 1. Mersereau et. al. [1, 3] and Petersen and Middleton [5] suggest the superiority of hexagonal sampling based on a circularly band-limited scene.

Fales et. al. [2] compare the two sampling methods not by assuming a band-limited scene, but instead assuming a constant sampling density. The results presented in this chapter are a composite of these two approaches (circularly band-limited scene and constant sampling density) and are based on the following assumptions:

- Two possible models of the pre-sampling image path (image formation),
  - the pre-sampling image ($g(\mathbf{x})$) is only filtered by the lens PSF, i.e. $h(\mathbf{x}) = h_l(\mathbf{x})$ or equivalently $\hat{h}[\nu] = \hat{h}_l[\nu]$.
  - the pre-sampling image is filtered by both the lens PSF and the sensor PSF appropriate to the particular sampling grid, i.e. $h(\mathbf{x}) = h_l(\mathbf{x}) * h_s(\mathbf{x})$ or equivalently $\hat{h}[\nu] = \hat{h}_l[\nu]\,\hat{h}_s[\nu]$.
- Two possible sampling grids, rectangular and hexagonal, with a constant sampling density of 1 : 16 (i.e. 1 pixel in the sampled image represents 16 scenels in the scene) for both grids.
- Two possible models of the reconstruction function,
  - the *display* reconstruction function (i.e. an emulation of a video display screen),
  - the *ideal* reconstruction function for the particular sampling grid.

The frequency content of the pre-sampling image (i.e. the input scene with the optics OTF and sensor OTF, if any, applied) is controlled through the use of a synthetic scene with a specific (circular) band-region. The computed fidelity loss metrics described in chapter 3 are shown as a function of the band-region radius of the synthetic scene for each of the 8 conditions mentioned above.

4.2.1 Synthetic Band-limited Scene

The two-dimensional, circularly band-limited, synthetic scenes used for this experiment were generated using the methodology described in chapter 2. The synthetic scene is defined in terms of phase and amplitude in the frequency domain by the equation

$$\hat{s}[\nu] = \frac{1}{2}\left(\rho[\nu]\cos\left(\phi[\nu]\right) - i\rho[\nu]\sin\left(\phi[\nu]\right)\right). \tag{4.1}$$

where $\phi[\nu]$ is the phase and $\rho[\nu]$ is the amplitude of the location defined by the frequency coordinates ν. The phase term used for the experiment was a uniformly distributed random value from $-\pi$ to π, generated by the "minimal standard" random number generator proposed by Park and Miller [4]. The amplitude term was defined by

$$\rho[\nu] = \begin{cases} \eta_s\left(1 - \frac{\|\nu\|}{R}\right) & \text{for } \|\nu\| \le R \\ 0 & \text{otherwise} \end{cases} \tag{4.2}$$

where:

$$\begin{aligned} \eta_s &= E[s(\mathbf{x})], \text{the desired mean of the scene } s(\mathbf{x}) \\ R &= \text{the normalized radius of the (circular) band-region} \\ \|\nu\| &= \sqrt{\left(\frac{\nu_1}{N_1}\right)^2 + \left(\frac{\nu_2}{N_2}\right)^2}. \end{aligned}$$

The value of η_s was specified to produce a scene $s(\mathbf{x})$ with a mean value one-half of its maximum possible value. The normalized radius of the band-region was varied from a value of 0.004 to a value of 0.50 for a square 512×512 ($N_1 = 512$, $N_2 = 512$) simulated scene. Figure 4.1 presents the amplitude portion of a typical synthetic scene with $R = 0.25$.

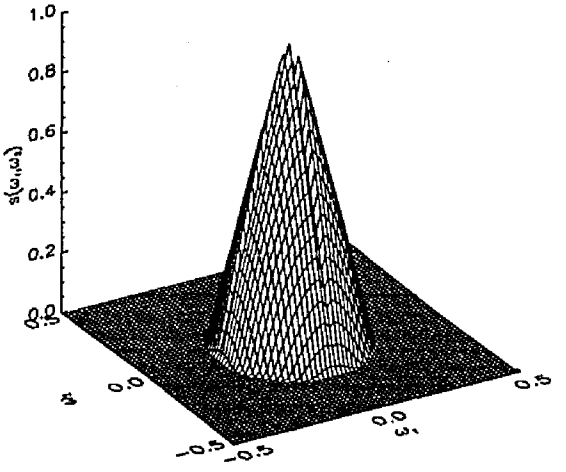

Figure 4.1: Synthetic Scene for $R = 0.25$

4.2.2 Image Formation

Three image formation OTFs were used for the purposes of this experiment,

$$\hat{h}[\nu] = \hat{h}_l[\nu] \tag{4.3}$$

$$\hat{h}[\nu] = \hat{h}_l[\nu]\,\hat{h}_{sh}[\nu] \tag{4.4}$$

$$\hat{h}[\nu] = \hat{h}_l[\nu]\,\hat{h}_{sr}[\nu] \tag{4.5}$$

where:

$$\begin{aligned} \hat{h}_l[\nu] &= \text{OTF for lens} \\ \hat{h}_{sh}[\nu] &= \text{OTF for hexagonally shaped sensor} \\ \hat{h}_{sr}[\nu] &= \text{OTF for rectangularly shaped sensor} \end{aligned}$$

The lens OTF $\hat{h}_l$ implemented is based on equation 2.22 in chapter 2 with $\alpha = 1.0$ and $\beta = 2$, i.e.

$$\hat{h}[\nu] = \exp\left(-\left(\frac{\|\nu\|}{1.0}\right)^2\right) \tag{4.6}$$

and as shown in figure 4.2.

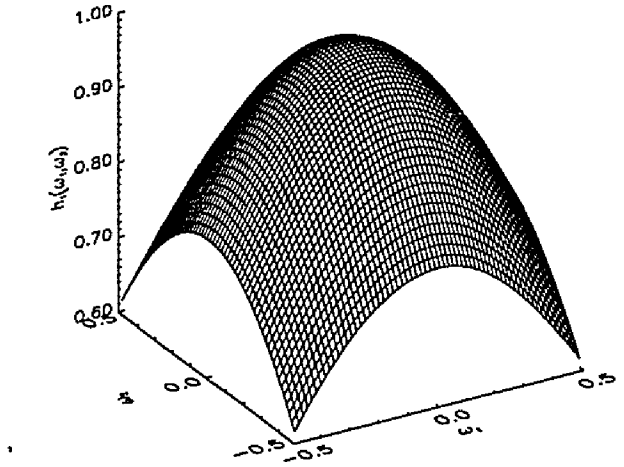

Figure 4.2: Lens OTF

The sensor OTFs used were based on a simple model of the spatial domain sensor array consisting of the following assumptions:

- The sensor is a non-infinitesimal active area of constant response surrounding the sample point.
- Each sensor is separated from adjacent sensors by a non-infinitesimal fill zone of zero response.
- The actual shape of the sensor depends upon the sampling grid used,
  - the sensor used for the hexagonal grid is a regular hexagon,
  - the sensor used for the rectangular grid is a square.
- The width of the fill zone between adjacent sensors is the same for both sampling grids.

The above assumptions lead to hexagonal and rectangular sensor PSFs having equal areas of constant response. Examples of rectangular and hexagonal sensor arrays, as described

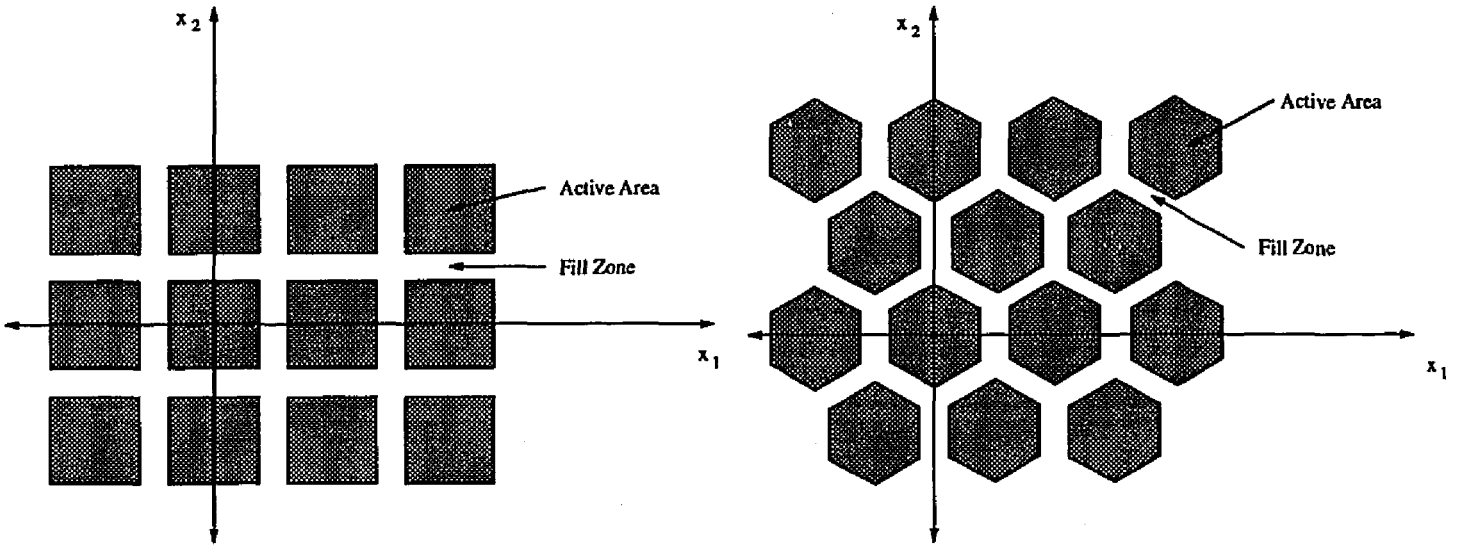

(a) Rectangular Sensors (b) Hexagonal Sensors

Figure 4.3: Sensor Array Model

above, are shown in figures 4.3(a) and 4.3(b). When applying this sensor model to a discrete simulation, the hexagonal and rectangular sensor PSFs continue to have equal areas of constant response, but due to the geometry of the simulated scene relative to the sensor shape, these equal areas do not contain an equal number of scenels. For the case of a simulated scene containing 512×512 scenels and a sampling density of $1 : 16$ the rectangular sensor PSF had 9 non-zero points, while the hexagonal sensor PSF had 11 non-zero points. The sensor OTF was then obtained by the Fourier transform of the sensor PSF. The hexagonal and rectangular sensor OTFs used are shown in figures 2.9 and 2.10 of chapter 2. The composite image formation OTFs described in equations 4.4 and 4.5 are shown in figures 4.4(a) and 4.4(b) respectively.

4.2.3 Sampling

The hexagonal and rectangular sampling grids are defined in terms of the spatial domain sampling matrix $\mathbf{V}$, where

$$\mathbf{V} = \begin{bmatrix} 2.0 & 2.0 \\ -4.0 & 4.0 \end{bmatrix} \tag{4.7}$$

for the hexagonal sampling grid used, and

$$\mathbf{V} = \begin{bmatrix} 4.0 & 0.0 \\ 0.0 & 4.0 \end{bmatrix} \tag{4.8}$$

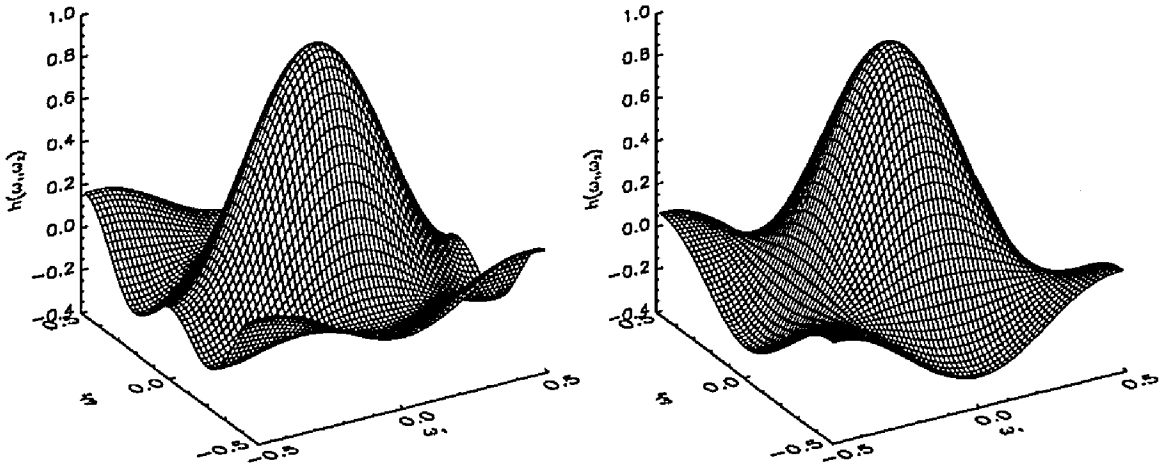

(a) Composite OTF - Hexagonal Sensor (b) Composite OTF - Rectangular Sensor

Figure 4.4: Image Formation OTF

for the rectangular sampling grid used. For both the hexagonal and the rectangular sampling grids, $|\det \mathbf{V}| = 16$.

4.2.4 Reconstruction Function

The ideal reconstruction function was defined to have a value of $|\det \mathbf{V}|$ over the sampling passband for the particular sampling geometry and have a value of 0 elsewhere, i.e.

$$\hat{r}[\nu] = \begin{cases} |\det \mathbf{V}| & \text{for } \nu \in B \\ 0 & \text{otherwise} \end{cases} \tag{4.9}$$

where B is the region enclosed by the baseband for the hexagonal or rectangular sampling geometry. Figures 4.5(a) and 4.5(b) show the ideal reconstruction function used for hexagonal sampling and rectangular sampling respectively.

The model used for the display reconstruction function is the sum of two Gaussian-spot functions [6] containing a strongly peaked central portion and a broad flare surrounding it, i.e.

$$\hat{r}[\nu] = 0.76 \exp\left(-\left(\frac{\|\nu\|}{0.4301484}\right)^2\right) + 0.24 \exp\left(-\left(\frac{\|\nu\|}{0.0323814}\right)^2\right), \tag{4.10}$$

as shown in figure 4.6.

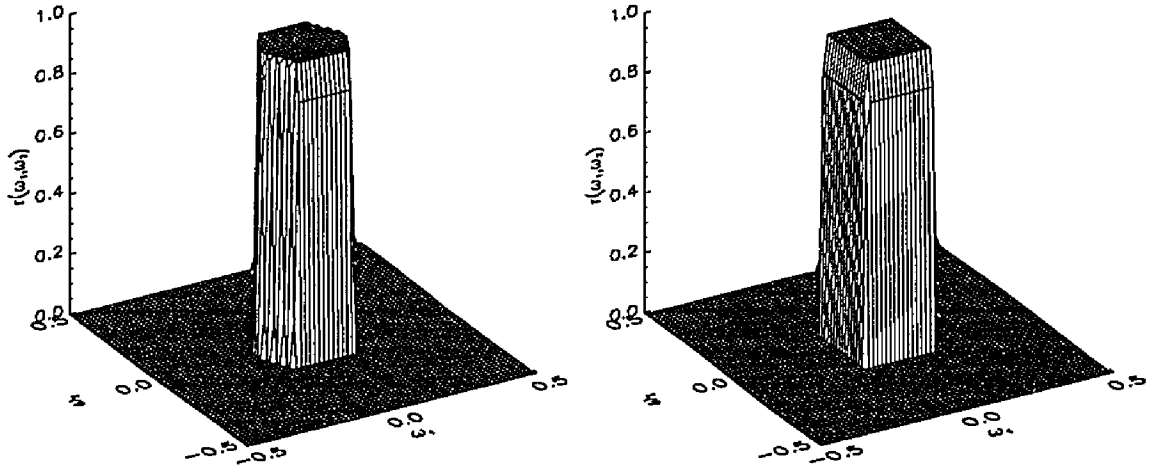

(a) Hexagonal (b) Rectangular

Figure 4.5: Ideal Reconstruction Functions

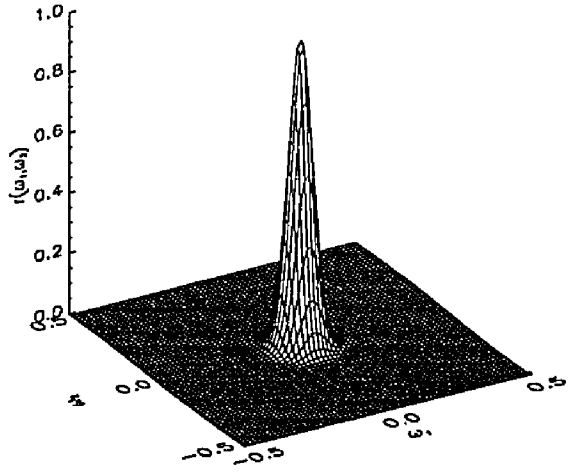

Figure 4.6: Display Reconstruction Function

4.3 Fidelity Loss Results

4.3.1 Imaging Fidelity Loss

Imaging fidelity loss is the mean-squared difference between the scene $s(\mathbf{x})$ and the pre-sampling image $g(\mathbf{x})$. The discrete frequency domain implementation of this metric is

$$\|s - g\|^2 = \sum_{\nu} |1 - \hat{h}[\nu]|^2 |\hat{s}[\nu]|^2. \tag{4.11}$$

Equation 4.11 indicates that imaging fidelity loss depends entirely on the image formation OTF $\hat{h}[\nu]$ and the input scene $\hat{s}[\nu]$. As mentioned previously, the input scene was varied by controlling the radius of the scene band-region. Figure 4.7(a) shows the fidelity loss due to the lens OTF as a function of scene band-region radius. As predicted by equation 4.11, the loss of image fidelity only becomes significant when there is significant scene energy at frequencies where the lens OTF is significantly different from one, i.e for larger values of the scene band-region radius.

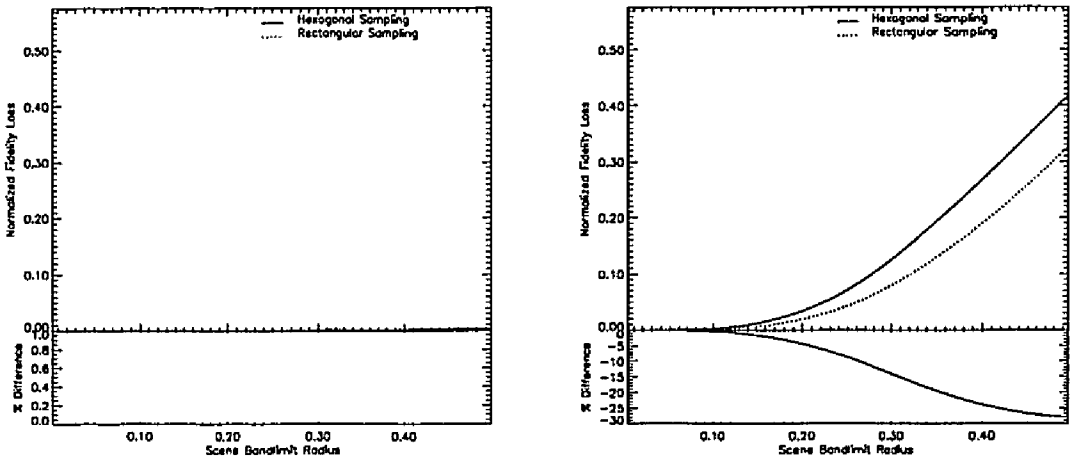

(a) No Sensor OTF

(b) Sensor OTF

Figure 4.7: Imaging Fidelity Loss

Figure 4.7(b) shows the fidelity loss due to the composite lens and sensor OTF as a function of scene band-region radius. The fidelity loss shown in figure 4.7, and throughout chapters 4 and 5, are normalized by the energy of the simulated scene. Immediately apparent is the large increase in fidelity loss, approximately two orders of magnitude, when compared with figure 4.7(a). This increase in fidelity loss is entirely due to the low pass filtering of the

sensor OTF. This increased fidelity loss is easily predictable upon comparison of the lens OTF to the composite OTFs in figure 4.4. Recall that the rectangular PSF kernel consisted of 9 scenels and the hexagonal PSF kernel consisted of 11 scenels, which translates to the hexagonal OTF providing slightly greater low pass filtering than the rectangular OTF. It is also predictable that the composite OTF containing the hexagonal sensor OTF would produce the greatest amount of imaging fidelity loss. This prediction is substantiated in figure 4.7(b). Also predictable from equation 4.11 is the observation that the particular reconstruction function used has no effect on imaging fidelity loss.

4.3.2 Sampling and Reconstruction Fidelity Loss

Sampling and reconstruction fidelity loss is the mean-square difference between the pre-sampling image $g(\mathbf{x})$ and the reconstructed image $s'(\mathbf{x})$, i.e.

$$E\left[\|g - s'\|^2\right] = \epsilon_r^2 + \epsilon_s^2 \tag{4.12}$$

where:

$$\epsilon_s^2 = \sum_{\boldsymbol{\nu}} \left| \frac{\hat{r}[\boldsymbol{\nu}]}{|\det \mathbf{V}|} \right|^2 \sum_{\mathbf{k} \neq 0} \left| \hat{h}[\boldsymbol{\nu} - \mathbf{U}\mathbf{k}] \hat{s}[\boldsymbol{\nu} - \mathbf{U}\mathbf{k}] \right|^2 \tag{4.13}$$

$$\epsilon_r^2 = \sum_{\boldsymbol{\nu}} \left| 1 - \frac{\hat{r}[\boldsymbol{\nu}]}{|\det \mathbf{V}|} \right|^2 \left| \hat{h}[\boldsymbol{\nu}] \hat{s}[\boldsymbol{\nu}] \right|^2 \tag{4.14}$$

for the discrete frequency domain implementation.

ϵ_s^2 Fidelity Loss Component

The ϵ_s^2 term, as defined by equation 4.13, accounts for the image fidelity loss due to aliasing caused by under-sampling. It is a measure of the fidelity loss caused by folding of significant image energy at frequencies beyond the Nyquist limit into lower frequencies where $\hat{r}[\boldsymbol{\nu}] \neq 0$. As indicated in equation 4.9, the ideal reconstruction function $\hat{r}[\boldsymbol{\nu}] \neq 0$ over the baseband for the given sampling geometry, and $\hat{r}[\boldsymbol{\nu}] = 0$ elsewhere. Using the ideal reconstruction function allows us to determine the Nyquist limit for the given sampling grid by finding the scene band-limit radius R where the transition from $\epsilon_s^2 = 0$ to $\epsilon_s^2 > 0$ occurs. From a careful examination of figures 4.8(a) and 4.8(b) it appears that the Nyquist limit occurs at approximately $R = 0.129$. For the conditions under investigation, i.e a sampling density of $1:16$ and a circularly band-limited scene, the Nyquist limit actually occurs at $R = 0.125$. However values for ϵ_s^2 were computed at $R = 0.121$ and $R = 0.129$ but not at $R = 0.125$.

Comparing figure 4.6 to figures 4.5(a) and 4.5(b) it is clear that the display reconstruction function has a much smaller passband. This is consistent with figure 4.8 where ϵ_s^2 is several orders of magnitude less when using the display reconstruction function, relative to the ideal reconstruction functions.

Inclusion of the sensor OTF significantly reduces the ϵ_s^2 values and also significantly impacts the relative differences in favor of hexagonal sampling. This is a predictable result because ϵ_s^2 is a measure of the high frequency image energy being folded back into lower frequencies, and the sensor OTFs filter out a considerable amount of high frequency energy as shown in figure 4.7, with the hexagonal sensor OTF filtering out slightly more high frequency energy than the rectangular sensor OTF.

ϵ_r^2 Fidelity Loss Component

The ϵ_r^2 term, as defined by equation 4.14 accounts for loss of image fidelity due to imperfect reconstruction. It is a measure of the fidelity loss caused by the presence of significant image energy, $|\hat{h}[\nu]\hat{s}[\nu]|^2$, at frequencies where $\hat{r}[\nu] \neq |\det \mathbf{V}|$. For the ideal reconstruction functions, the values obtained for ϵ_r^2 (figures 4.9(a) and 4.9(b)) are almost identical to the values obtained for ϵ_s^2 (figures 4.8(a) and 4.8(b)). This is due to the fact that the reconstruction function has a value of $|\det \mathbf{V}|$ over the sampling baseband (Nyquist region) and a value of zero elsewhere. ϵ_s^2 measures the amount of energy outside the Nyquist region, and ϵ_r^2 measures the amount of energy where $\hat{r}[\nu] \neq |\det \mathbf{V}|$, which define essentially the same regions. The display reconstruction function $\hat{r}[\nu] = |\det \mathbf{V}|$ at only one location, $\nu = [0,0]$. This implies that for values of $R > 0$ ϵ_r^2 will always be greater than zero, which is displayed graphically in figures 4.9(c) and 4.9(d).

Sampling and Reconstruction Fidelity Loss

The sum $\epsilon_r^2 + \epsilon_s^2 = 0$ defines the conditions under which perfect reconstruction of the pre-sampling image $g(\mathbf{x})$ from its sampled data is possible. Perfect reconstruction can occur only when both ϵ_r^2 and ϵ_s^2 are simultaneously zero since both quantities are non-negative. As mentioned in chapter 3 the conditions required for perfect reconstruction are:

1. $\hat{r}[\nu]$ must equal $|\det \mathbf{V}|$ where the band-region of the pre-sampling image contains energy ($\hat{h}[\nu]\hat{s}[\nu] \neq 0$).

2. $\hat{r}[\nu]$ must equal zero where the instances of the periodic extension of $\hat{g}[\nu]$ contain energy ($\hat{h}[\nu - \mathbf{Uk}]\hat{s}[\nu - \mathbf{Uk}] \neq 0$).

3. The sampling matrix $\mathbf{V}$ (and hence the periodicity matrix $\mathbf{U}$) must be defined such that adjacent instances of the periodic extension of $\hat{g}[\nu]$ ($\hat{h}[\nu - \mathbf{Uk}]\hat{s}[\nu - \mathbf{Uk}]$) do not overlap.

The ideal reconstruction functions meet all three of the above conditions as long as the scene band-region radius is less than $R = 0.125$. For $R \leq 0.125$ the scene, and hence the pre-sampling image, contains no energy at any point where $\hat{r}[\nu] \neq |\det \mathbf{V}|$. Also, none of the periodic extensions of the pre-sampling image contain energy in any region where $\hat{r}[\nu] \neq 0$.

Finally, none of the adjacent instances of the periodic extensions of the pre-sampling image overlap, folding energy at high frequencies back into lower frequencies. When $R > 0.125$, none of the above three conditions are met. This is clearly demonstrated in figures 4.10(a) and 4.10(b).

For any $R > 0$ the display reconstruction function does not meet the above conditions for complete reconstruction of the pre-sampling image. Primarily the first condition is not met because, as mentioned previously, there is only one location, $\nu = [0, 0]$, where $\hat{r}[\nu] = |\det \mathbf{V}|$, and the pre-sampling image contains energy at frequencies where $\hat{r}[\nu] \neq |\det \mathbf{V}|$. The second condition fails because $\hat{r}[\nu] > 0$ for all points on the ν plane. As with the ideal reconstruction functions, condition 3 fails for $R > 0.125$ because the band-region of the scene (and pre-sampling image) exceeds the Nyquist limit imposed by the sampling grid. This is shown in figures 4.10(c) and 4.10(d).

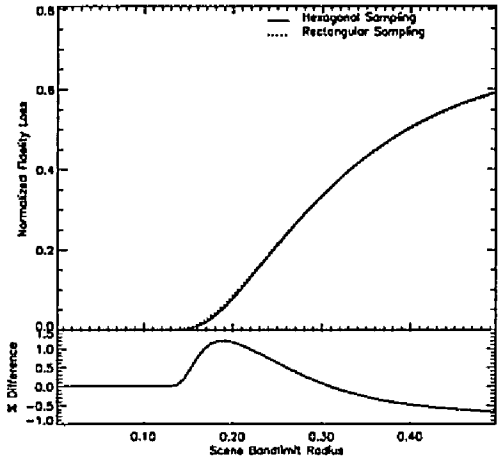

(a) No Sensor OTF - Ideal Reconstruction

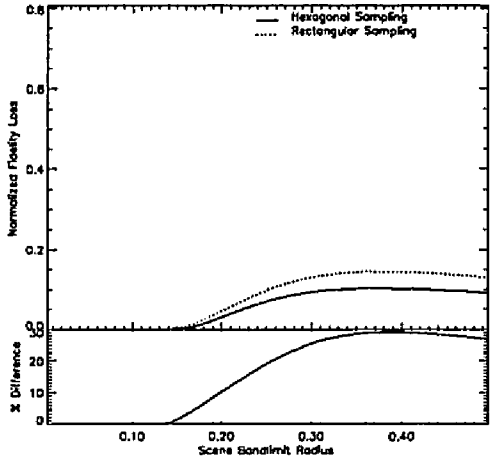

(b) Sensor OTF- Ideal Reconstruction

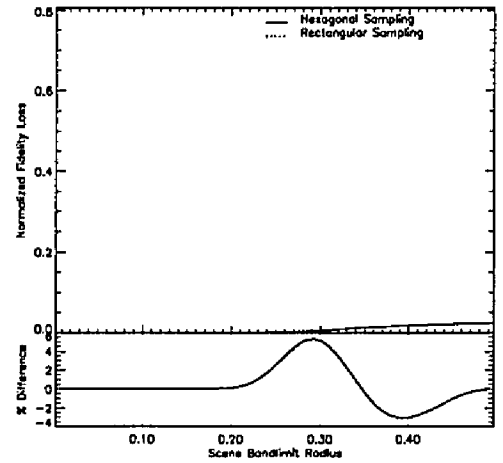

(c) No Sensor OTF - Display Reconstruction

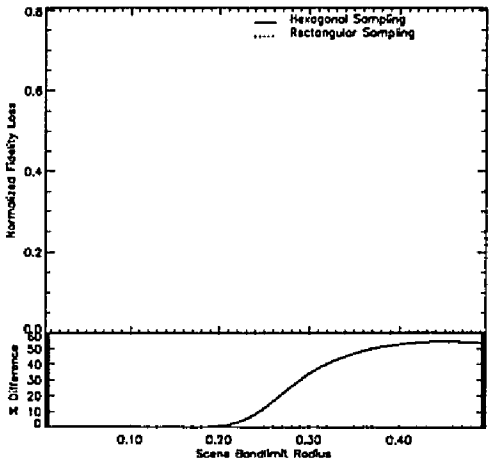

(d) Sensor OTF - Display Reconstruction

Figure 4.8: ϵ_s^2 Fidelity Loss Component

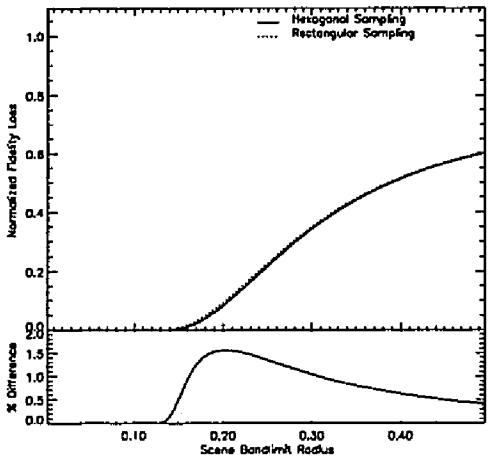

(a) No Sensor OTF - Ideal Reconstruction

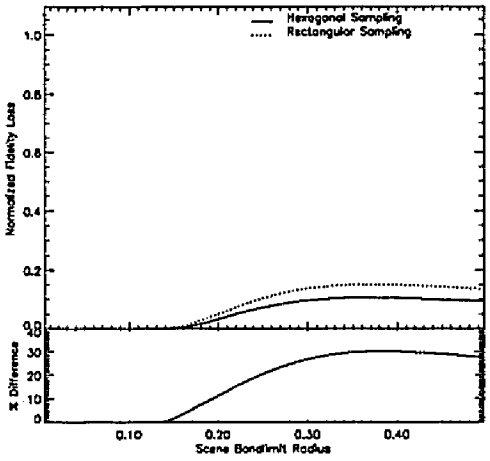

(b) Sensor OTF - Ideal Reconstruction

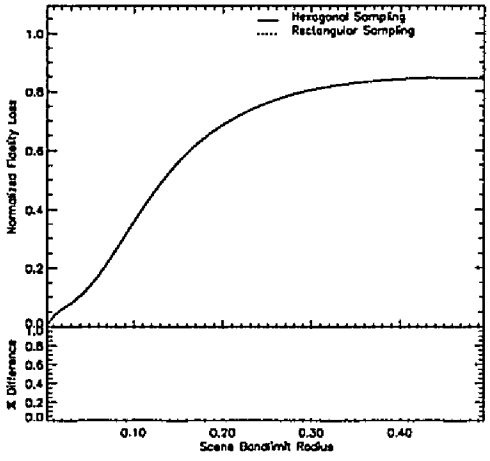

(c) No Sensor OTF - Display Reconstruction

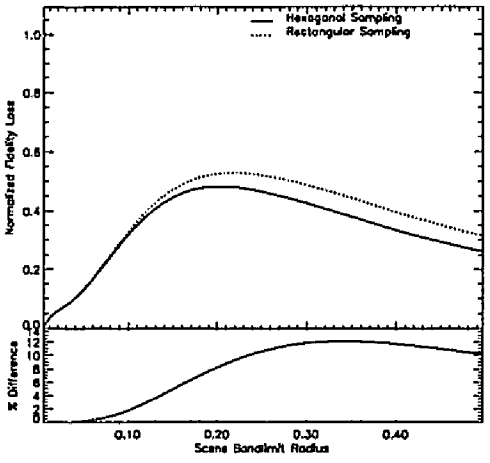

(d) Sensor OTF - Display Reconstruction

Figure 4.9: ϵ_f^2 Fidelity Loss Component

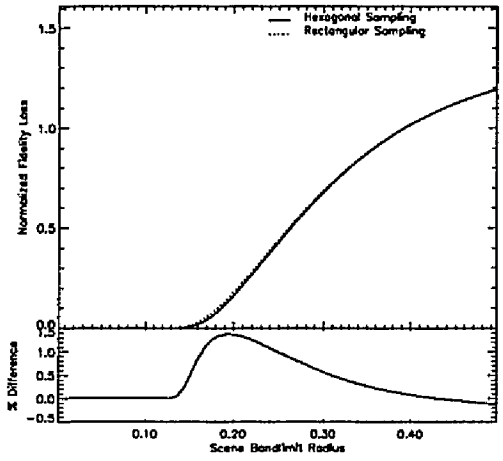

(a) No Sensor OTF - Ideal Reconstruction

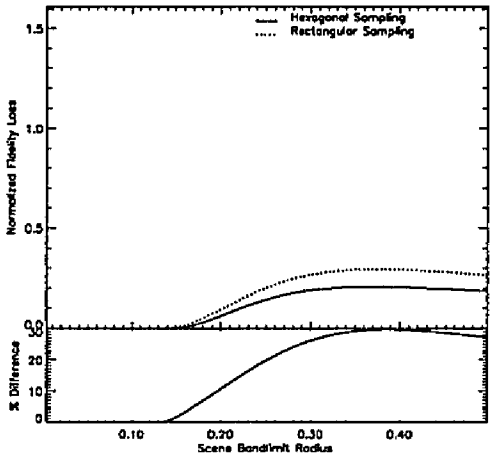

(b) Sensor OTF - Ideal Reconstruction

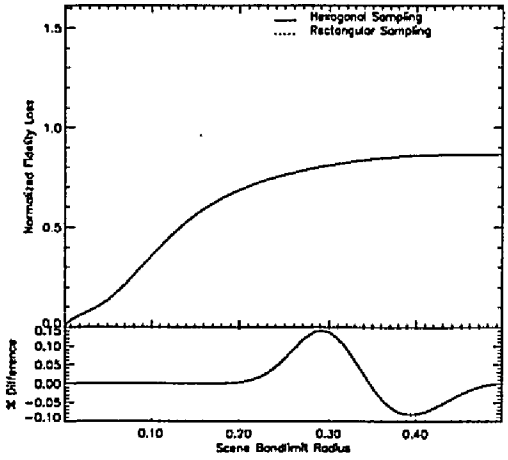

(c) No Sensor OTF - Display Reconstruction

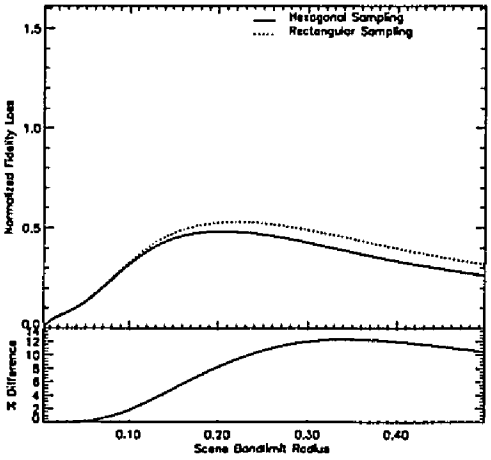

(d) Sensor OTF - Display Reconstruction

Figure 4.10: Sampling and Reconstruction Fidelity Loss

4.3.3 End-to-End Fidelity Loss

End-to-end fidelity loss is the mean-square difference between the original scene $s(\mathbf{x})$ and the reconstructed image $s'(\mathbf{x})$ i.e.

$$E\left[\|s - s'\|^2\right] = \epsilon_e^2 + \epsilon_s^2 \tag{4.15}$$

where

$$\epsilon_e^2 = \sum_{\boldsymbol{\nu}} \left|1 - \frac{\hat{r}[\boldsymbol{\nu}]}{|\det \mathbf{V}|}\hat{h}[\boldsymbol{\nu}]\right|^2 |\hat{s}[\boldsymbol{\nu}]|^2 . \tag{4.16}$$

and ϵ_s^2 is given in equation (4.13).

ϵ_e^2 Fidelity Loss Component

The term ϵ_e^2 accounts for the end-to-end loss of fidelity caused by significant scene energy $|\hat{s}[\boldsymbol{\nu}]|^2$ at frequencies where the cascaded response $\hat{r}[\boldsymbol{\nu}]\hat{h}[\boldsymbol{\nu}] \neq |\det \mathbf{V}|$. ϵ_e^2 measures how well the reconstruction function $\hat{r}[\boldsymbol{\nu}]$ is able to restore the frequencies that were suppressed prior to sampling by the image formation OTF $\hat{h}[\boldsymbol{\nu}]$. The cascaded response $\hat{r}[\boldsymbol{\nu}]\hat{h}[\boldsymbol{\nu}]$, where $\hat{r}[\boldsymbol{\nu}]$ is the ideal reconstruction function and $\hat{h}[\boldsymbol{\nu}]$ has no sensor OTF component, is effectively equal to $|\det \mathbf{V}|$ over the Nyquist region. This accounts for the insignificant ϵ_e^2 fidelity loss up to $R = 0.125$ as shown in figure 4.11(a). The composite OTFs in figure 4.4 decrease much more rapidly with increasing frequency compared to the lens OTF, which accounts for the much lower value of R at which ϵ_e^2 fidelity loss becomes apparent, as shown in figure 4.11(b).

The ϵ_e^2 results obtained for the display reconstruction function, figures 4.11(c) and 4.11(d), are analogous to those obtained for ϵ_r^2 in figures 4.9(c) and 4.9(d). As was the case for ϵ_r^2, this is primarily because the display reconstruction function has only one point where $\hat{r}[\boldsymbol{\nu}] = |\det \mathbf{V}|$, $\boldsymbol{\nu} = [0,0]$, which implies that for values of $R > 0$ ϵ_e^2 will always be greater than zero.

End–to–End Fidelity Loss

Analogous to the individual terms for sampling/reconstruction fidelity loss ϵ_e^2 and ϵ_s^2 are both non-negative quantities. In order to have zero end-to-end fidelity loss, both ϵ_e^2 and ϵ_s^2 must be simultaneously zero. As mentioned in chapter 3 the sum $\epsilon_e^2 + \epsilon_s^2 = 0$ defines the conditions necessary for complete reconstruction of the original scene $s(\mathbf{x})$ to occur.

1. The cascaded response $\hat{r}[\boldsymbol{\nu}]\hat{h}[\boldsymbol{\nu}]$ must equal $|\det \mathbf{V}|$ where the band-region of the original scene contains energy ($\hat{s}[\boldsymbol{\nu}] \neq 0$).

2. $\hat{r}[\boldsymbol{\nu}]$ must equal zero where the instances of the periodic extension of $\hat{g}[\boldsymbol{\nu}]$ contain energy ($\hat{h}[\boldsymbol{\nu} - \mathbf{Uk}]\hat{s}[\boldsymbol{\nu} - \mathbf{Uk}] \neq 0$).

3. The sampling matrix **V** (and hence the periodicity matrix **U**) must be defined such that adjacent instances of the periodic extension of $\hat{g}[\boldsymbol{\nu}]$ ($\hat{h}[\boldsymbol{\nu} - \mathbf{Uk}]\hat{s}[\boldsymbol{\nu} - \mathbf{Uk}]$) do not overlap.

The ideal reconstruction functions meet all three of the above conditions as long as the scene band-region radius is less than the Nyquist limit, i.e. $R = 0.125$. For $R \leq 0.125$ the scene contains no energy at any point where $\hat{r}[\boldsymbol{\nu}]\hat{h}[\boldsymbol{\nu}] \neq |\det \mathbf{V}|$. Also, none of the periodic extensions of the pre-sampling image, $\hat{g}[\boldsymbol{\nu} - \mathbf{Uk}]$, contain energy in any region where $\hat{r}[\boldsymbol{\nu}] \neq 0$. Finally, none of the adjacent instances of the periodic extensions of the pre-sampling image overlap, folding energy at high frequencies back into lower frequencies. When $R > 0.125$, none of the above three conditions are met. This is shown in figures 4.12(a) and 4.12(b).

For any $R > 0$, the display reconstruction function does not meet the above conditions for complete reconstruction of the original scene. Primarily the first condition is not met for values of $R > 0$ because, as mentioned previously, there is only one location, $\boldsymbol{\nu} = (0, 0)$, where $\hat{r}[\boldsymbol{\nu}]\hat{h}[\boldsymbol{\nu}] = |\det \mathbf{V}|$, and for $R > 0$ the pre-sampling image contains energy at frequencies where $\hat{r}[\boldsymbol{\nu}]\hat{h}[\boldsymbol{\nu}] \neq |\det \mathbf{V}|$. The second condition fails due to the fact that $\hat{r}[\boldsymbol{\nu}] > 0$ for all points on the (ν_1, ν_2) plane. As with the ideal reconstruction functions, condition 3 fails for $R > 0.125$ because the band-region of the scene (and pre-sampling image) exceeds the Nyquist limit imposed by the sampling grid. This is shown in figures 4.12(c) and 4.12(d). These figures also show that for the display reconstruction function, there is essentially no difference between hexagonal and rectangular sampling. Any gains due to the hexagonal sampling grid are completely overshadowed by the fidelity loss due to the display reconstruction function.

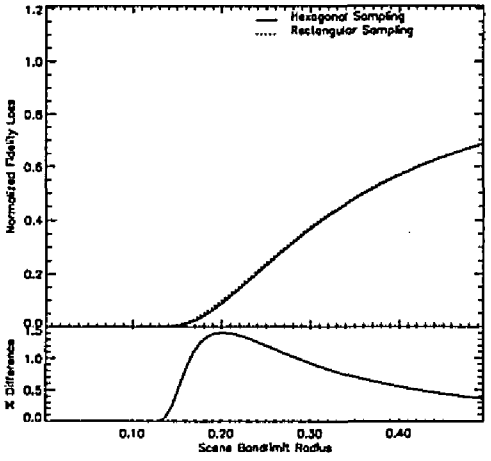

(a) No Sensor OTF - Ideal Reconstruction

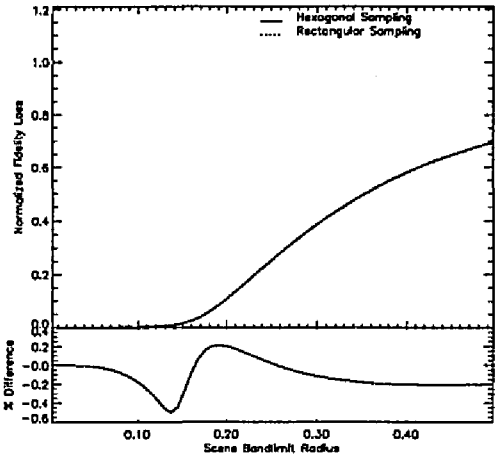

(b) Sensor OTF - Ideal Reconstruction

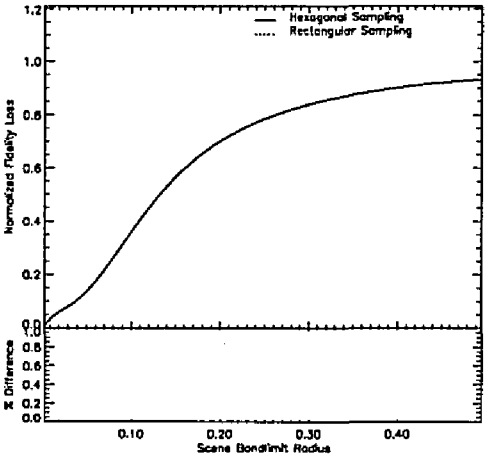

(c) No Sensor OTF - Display Reconstruction

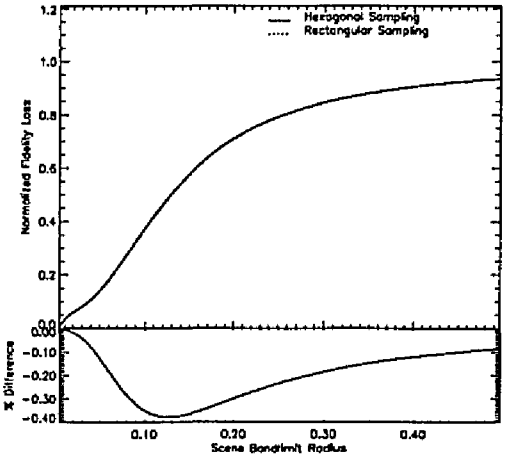

(d) Sensor OTF - Display Reconstruction

Figure 4.11: ϵ_e^2 Fidelity Loss Component

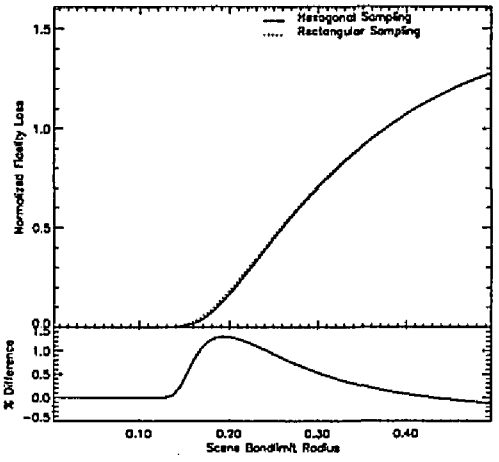

(a) No Sensor OTF - Ideal Reconstruction

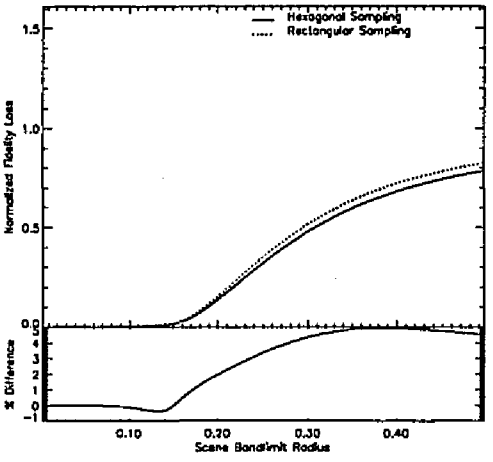

(b) Sensor OTF - Ideal Reconstruction

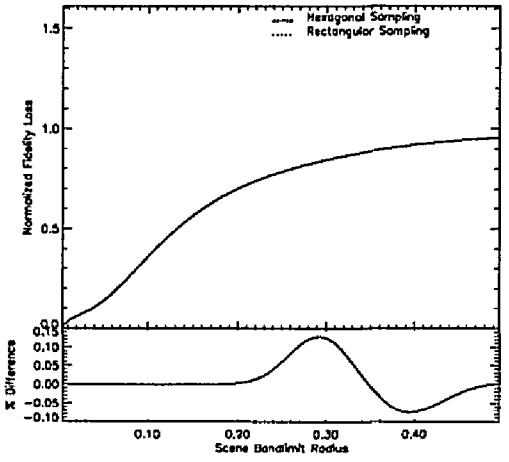

(c) No Sensor OTF - Display Reconstruction

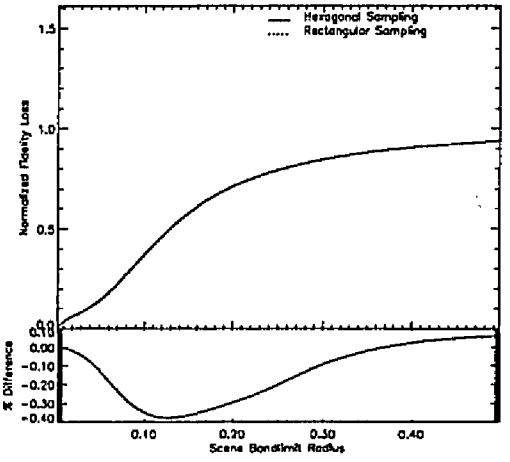

(d) Sensor OTF - Display Reconstruction

Figure 4.12: End-to-End Fidelity Loss

References

[1] Dan E. Dudgeon and Russell M. Mersereau. *Multidimensional Digital Signal Processing.* Prentice-Hall, Englewood Cliffs, NJ, 1984.

[2] Carl L. Fales, Friedrich O. Huck, and Richard W. Samms. Image system design for improved information capacity. *Applied Optics*, 23(6):872–888, 1984.

[3] Russel M. Mersereau. The processing of hexagonally sampled two-dimensional signals. *Proceedings of the IEEE*, 67(6):930–949, 1979.

[4] Stephen K. Park and Keith W. Miller. Random number generators: Good ones are hard to find. *Communications of the ACM*, 31(10):1192–1201, 1988.

[5] Daniel P. Petersen and David Middleton. Sampling and reconstruction of wave-number-limited functions in n-dimensional euclidean spaces. *Information and Control*, 5(4):279–323, 1962.

[6] Stephen E. Reichenbach. *Small-Kernel Image Restoration.* PhD thesis, College of William and Mary, July 1989.

Chapter 5

Experimental Results - Digital Scenes

5.1 Experimental Design

The use of synthetic scenes allows precise control of the frequency content of the scene, but provides little control over the spatial structure of the scene. The results obtained in chapter 4 provide significant insight into the mechanisms producing loss of fidelity in a digital imaging system, and provide supporting evidence for the observations made in chapter 3. Unfortunately those same results provide no information on how the various fidelity losses would be perceived by a human observer. The results presented in this chapter provide insight into how the various fidelity loss mechanisms affect the spatial structure of digital images. The experimental design is essentially the same as that used in the previous chapter. The primary difference is the use of the image formation OTF to vary the frequency content of the digital scene as opposed to directly specifying the frequency content of the band-limited synthetic scene. The frequency content of the pre-sampling image is controlled by the image formation OTF. The shape of the image formation OTF is determined by the inclusion or exclusion of the sensor OTF and by the α parameter for the optics OTF. The fidelity loss metrics described in chapter 3 are shown as a function of the optics OTF parameter α for each of the conditions mentioned above as applied to each of the digital scenes described below.

5.1.1 Digital Scenes

Four digital images obtained from various sources were used as digital scenes for the purposes of this simulation. Two of the images, *Cat* and *Mandril*, were 512 x 512 images with 256 gray-levels. The other two images *George* and *Circles* were 1024 x 1024 images with 256 gray-levels. The images used are by no means a representative sample of the possible

images that could have been used, although they were selected for particular features. *Cat* was picked as a typical image having some curved features and some straight features. *Mandril* was chosen as an extension to *Cat*, having a fair amount of vertical orientation. *George* was picked for the regular, periodic patterns visible. *Circles* was chosen because of the high frequency information present, and as a good test of the resolution of the sampling grid.

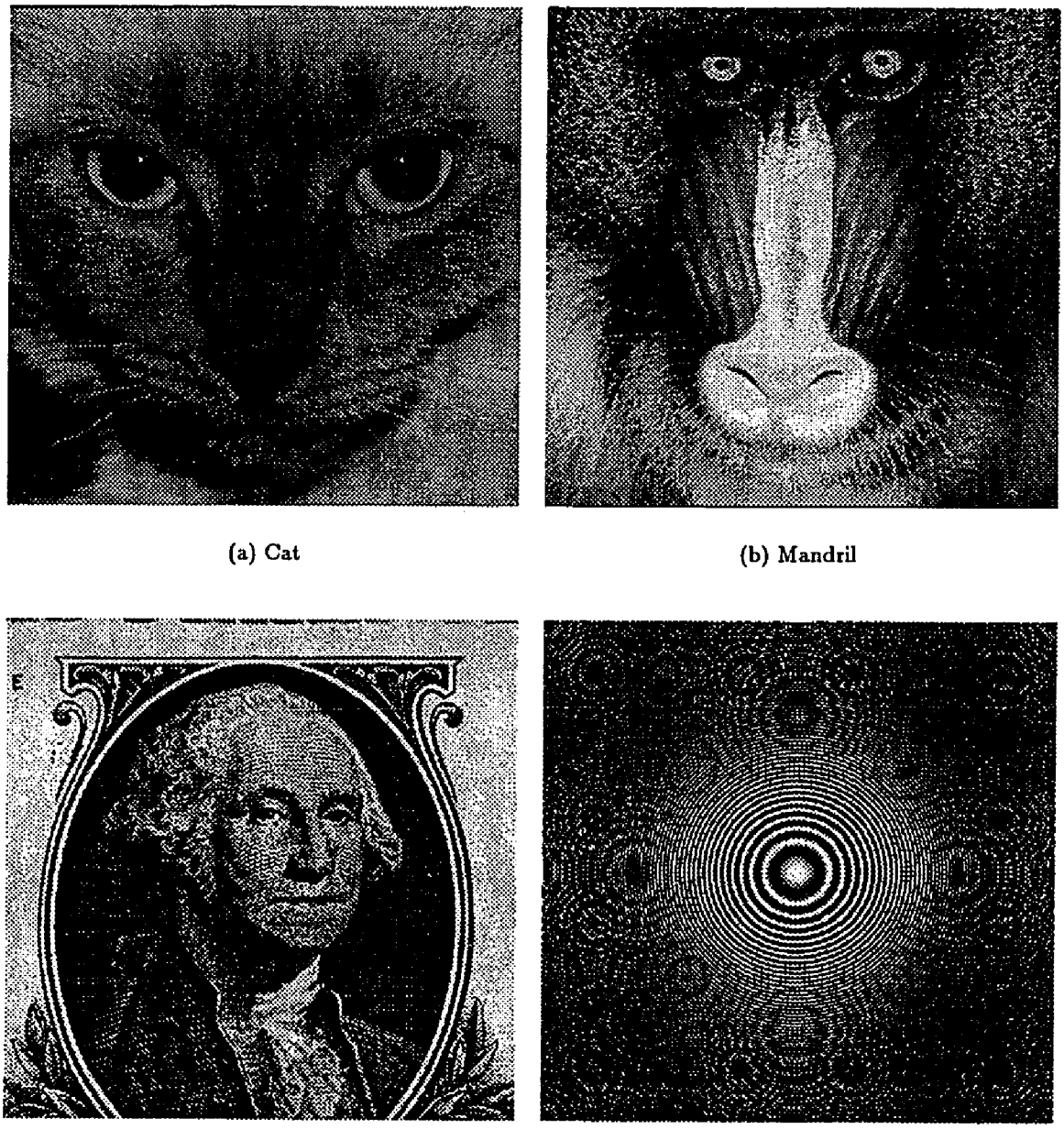

(a) Cat

(b) Mandril

(c) George

(d) Circles

Figure 5.1: Digital Scenes Used for Simulations

5.1.2 Image Formation

As in the previous chapter three image formation OTFs were used to manipulate the frequency content of the pre-sampling image,

$$\hat{h}[\nu] = \hat{h}_l[\nu] \tag{5.1}$$
$$\hat{h}[\nu] = \hat{h}_l[\nu]\,\hat{h}_{sh}[\nu] \tag{5.2}$$
$$\hat{h}[\nu] = \hat{h}_l[\nu]\,\hat{h}_{sr}[\nu] \tag{5.3}$$

where:

$$\hat{h}_l[\nu] = \text{OTF for lens}$$
$$\hat{h}_{sh}[\nu] = \text{OTF for hexagonally shaped sensor}$$
$$\hat{h}_{sr}[\nu] = \text{OTF for rectangularly shaped sensor}$$

The lens OTF is given by equation 2.22 in chapter 2 with $\beta = 2$ and α varying between 0.04 and 1.00, i.e.

$$\hat{h}[\nu] = \exp\left(-\left(\frac{\|\nu\|}{\alpha}\right)^2\right) \tag{5.4}$$

and as shown in figures 5.2(a) and 5.2(b).

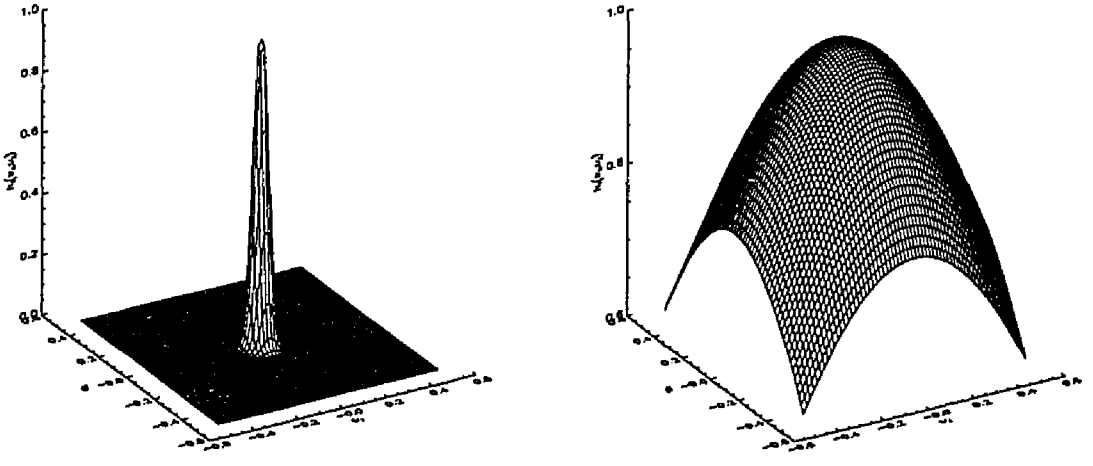

(a) $\alpha = 0.04$ (b) $\alpha = 1.00$

Figure 5.2: Image Formation Optical Transfer Function

Also as in the previous chapter, the sensor OTFs used were based on a simple model of the spatial domain sensor array consisting of the following assumptions:

- The sensor is a non-infinitesimal active area of constant response surrounding the sample point.
- Each sensor is separated from adjacent sensors by a non-infinitesimal fill zone of zero response.
- The actual shape of the sensor depends upon the sampling grid used,
  - the sensor used for the hexagonal grid is a regular hexagon,
  - the sensor used for the rectangular grid is a square.
- The width of the fill zone between adjacent sensors is the same for both sampling grids.

The above assumptions lead to hexagonal and rectangular sensor PSFs having equal areas of constant response. As was mentioned in the previous chapter, when applying this sensor model to a discrete simulation, the hexagonal and rectangular sensor PSFs do not contain an equal number of scenels. The hexagonal and rectangular sensor OTFs used are shown in figures 2.4 and 2.5 of chapter 2. The composite image formation OTFs described in equations 5.2 and 5.3 are shown in the previous chapter for $\alpha = 1.00$ and in figure 5.3 for $\alpha = 0.25$ and $\alpha = 0.75$.

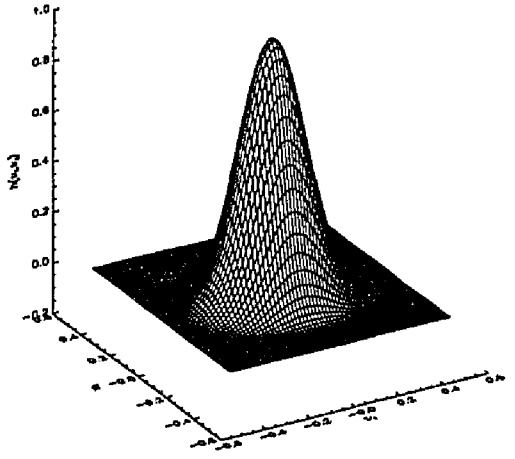

(a) Hexagonal Sensor - $\alpha = 0.25$

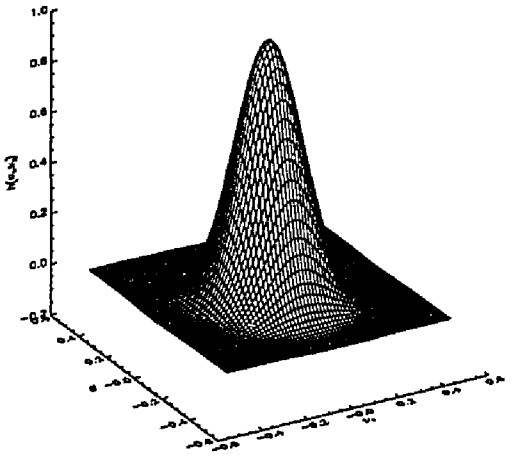

(b) Rectangular Sensor - $\alpha = 0.25$

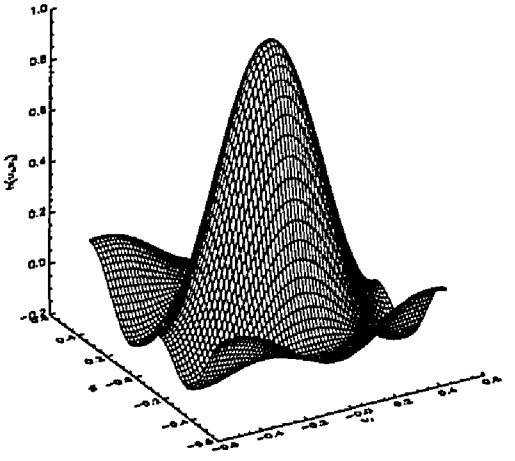

(c) Hexagonal Sensor - $\alpha = 0.75$

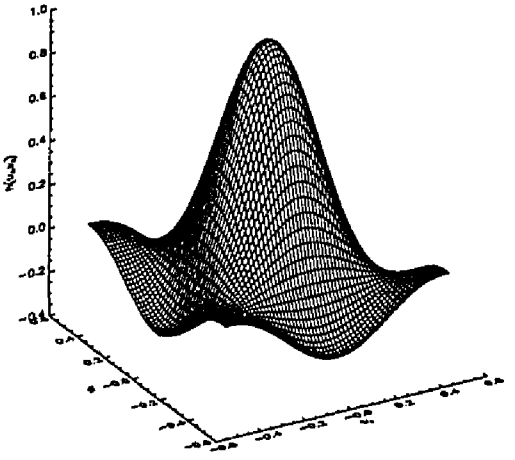

(d) Rectangular Sensor - $\alpha = 0.75$

Figure 5.3: Composite Image Formation OTF

5.2 Fidelity Loss Results

The results presented in the previous chapter provide little intuitive insight into how the various fidelity loss mechanisms relate to the appearance of the reconstructed digital image. The results presented here attempt to provide this insight by presenting numerical fidelity loss results, analogous to those presented in chapter 4, followed immediately by images displaying the measured fidelity losses.

5.2.1 Imaging Fidelity Loss

Imaging fidelity loss is defined in the frequency domain as

$$\|s - g\|^2 = \sum_{\nu} |1 - \hat{h}[\nu]|^2 |\hat{s}[\nu]|^2. \tag{5.5}$$

Equation 5.5 indicates that imaging fidelity loss depends entirely on the image formation OTF $\hat{h}[\nu]$ and the input scene $\hat{s}[\nu]$. Imaging fidelity loss becomes significant when there is significant scene energy at frequencies where the image formation OTF is significantly different from one, i.e for smaller values of the image formation OTF parameter α. For low values of α (i.e. $\alpha < 0.5$), the optics OTF is the dominant contributing factor to imaging fidelity loss. Conversely, for values of $\alpha > 0.5$ the sensor OTF is the dominating factor. This can be seen by comparing the composite OTFs shown in figure 5.3, and is shown graphically in figure 5.4. As was observed for band-limited scenes in the previous chapter, the hexagonal sensor OTF produces higher levels of imaging fidelity loss.

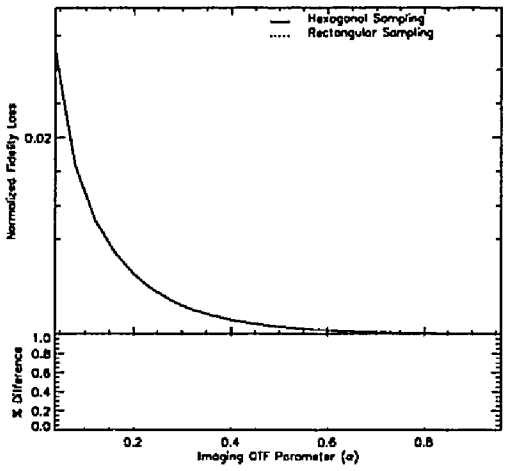

(a) Cat

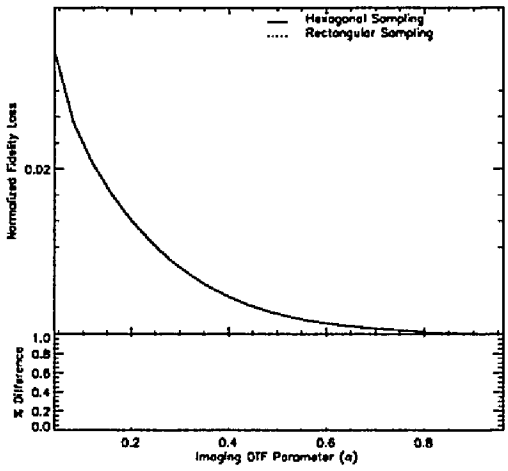

(b) Mandril

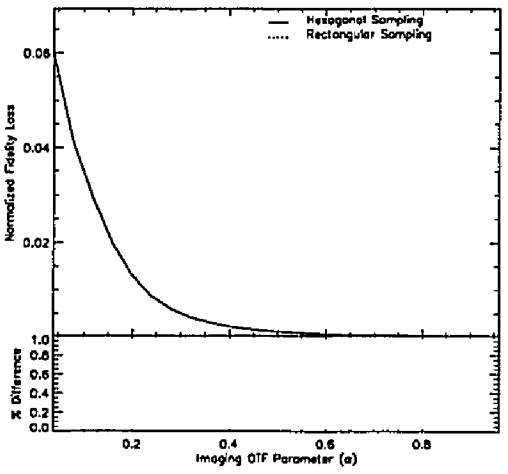

(c) George

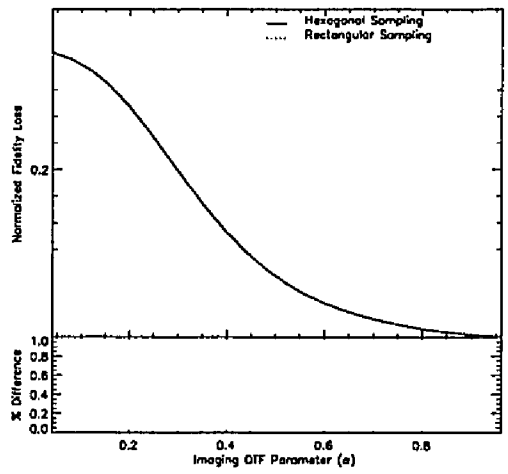

(d) Circles

Figure 5.4: Imaging Fidelity Loss - No sensor OTF

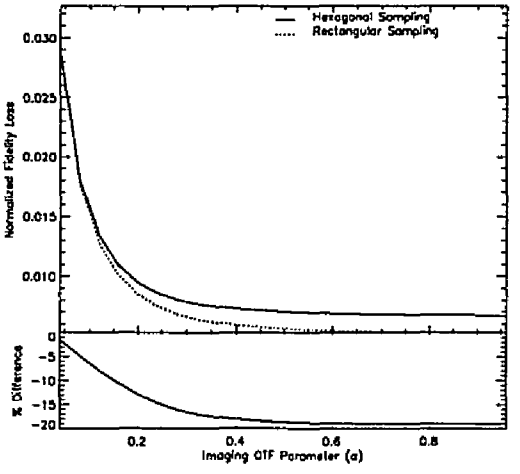

(a) Cat

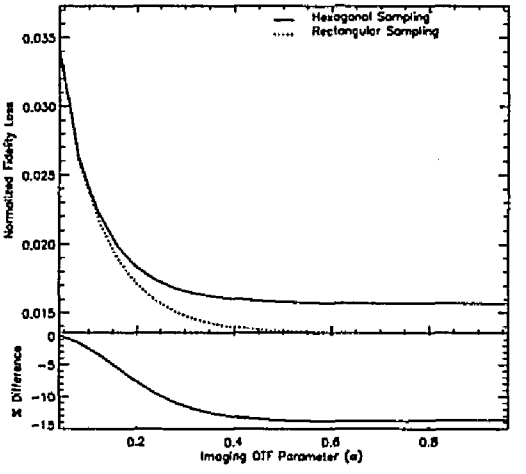

(b) Mandril

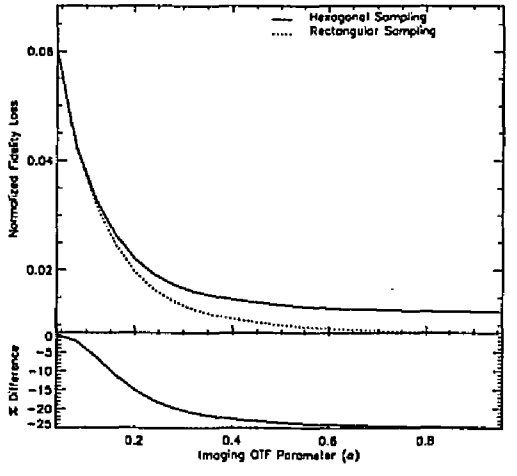

(c) George

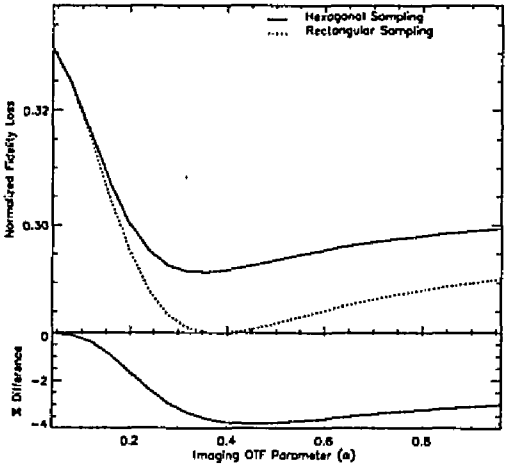

(d) Circles

Figure 5.5: Imaging Fidelity Loss - Sensor OTF

(a) Cat

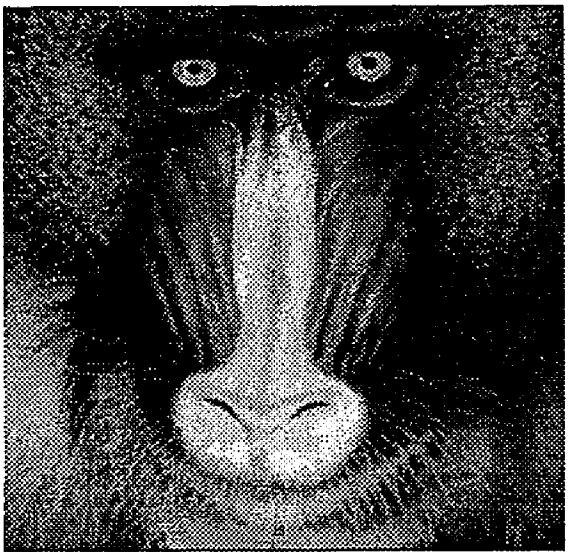

(b) Mandril

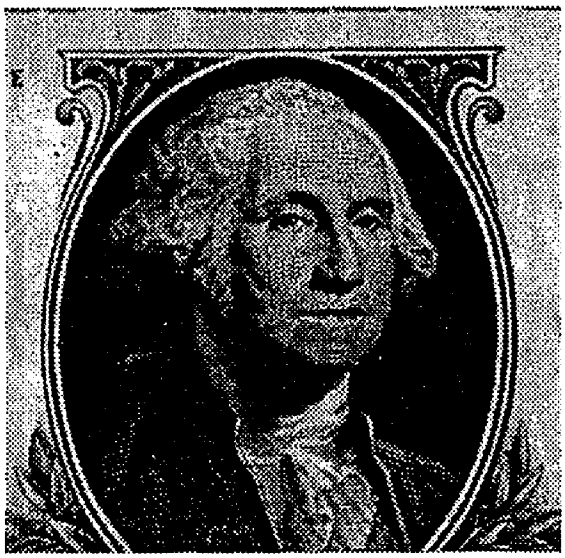

(c) George

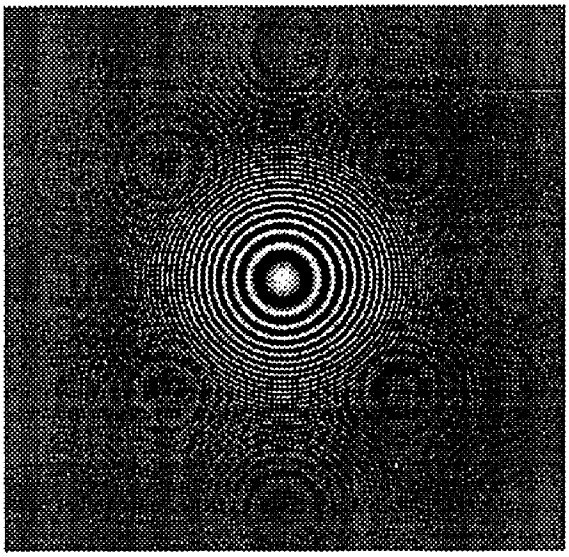

(d) Circles

Figure 5.6: Digital Scenes with Optics OTF $\alpha = 0.25$

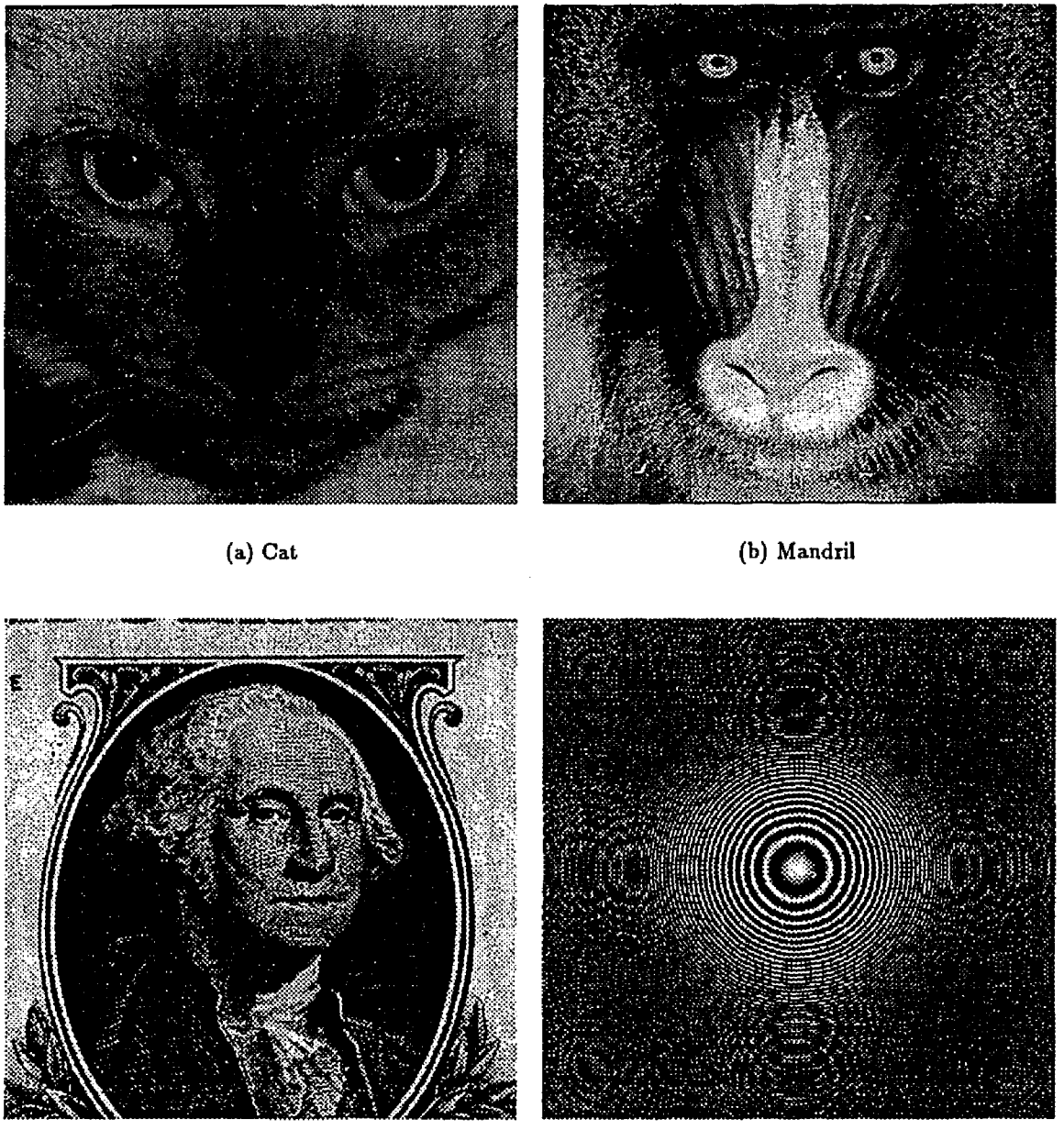

(a) Cat

(b) Mandril

(c) George

(d) Circles

Figure 5.7: Digital Scenes with Optics OTF $\alpha = 0.75$

(a) Cat

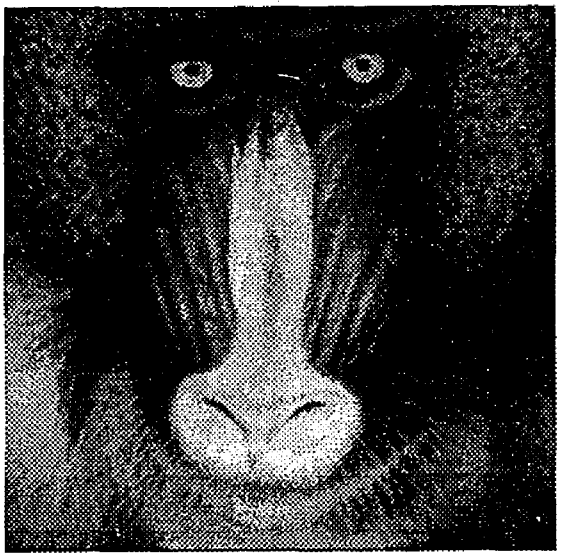

(b) Mandril

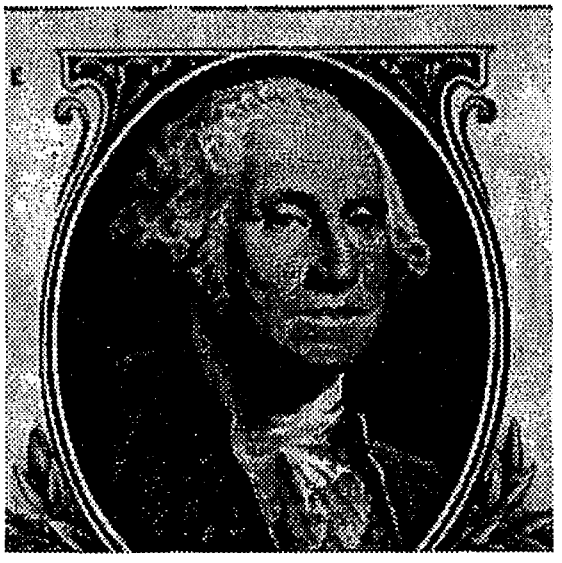

(c) George

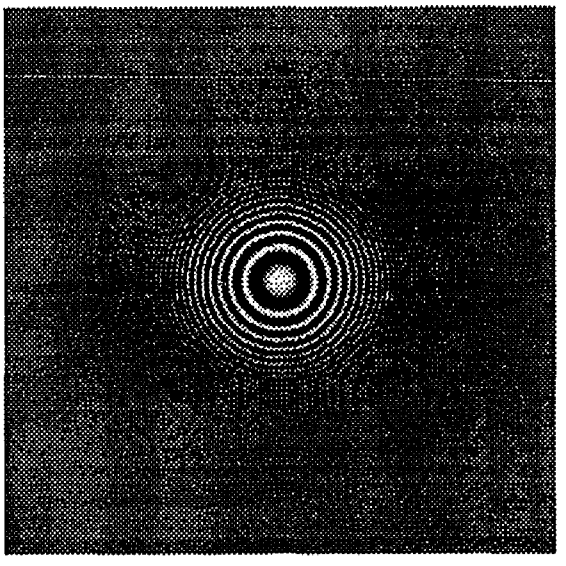

(d) Circles

Figure 5.8: Digital Scenes with Optics OTF $\alpha = 0.25$ and Hexagonal Sensor

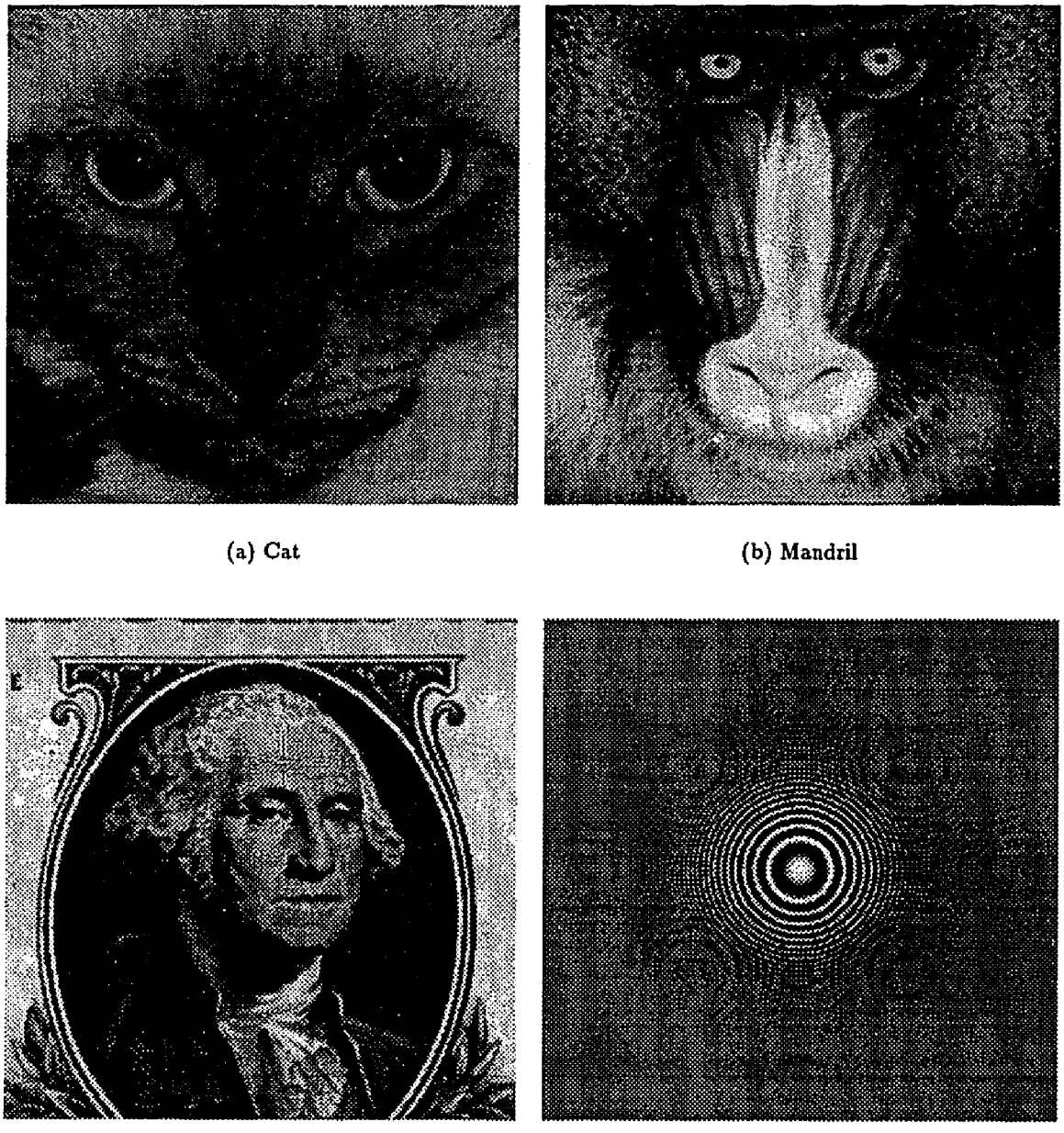

(a) Cat

(b) Mandril

(c) George

(d) Circles

Figure 5.9: Digital Scenes with Optics OTF $\alpha = 0.25$ and Rectangular Sensor

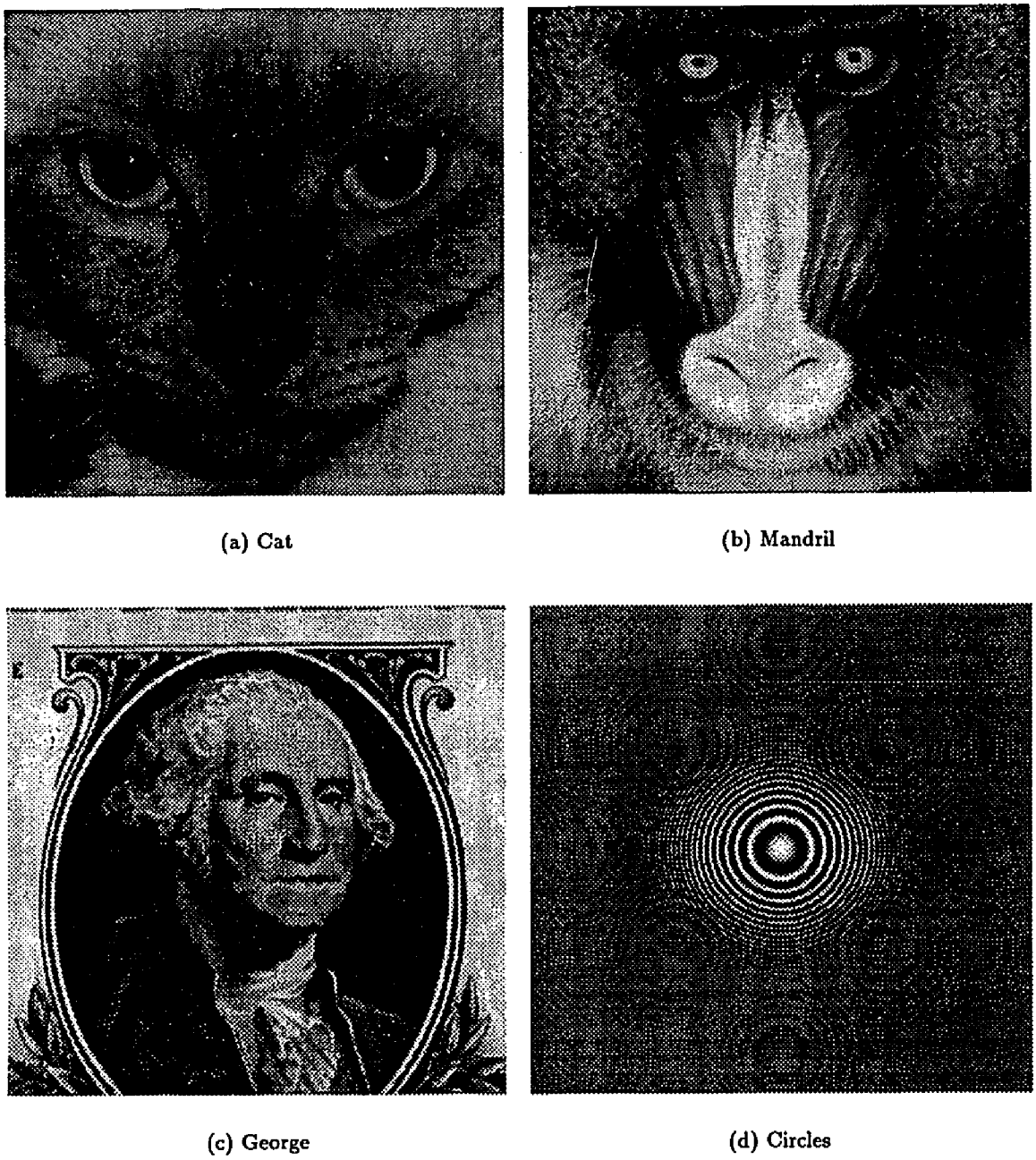

(a) Cat

(b) Mandril

(c) George

(d) Circles

Figure 5.10: Digital Scenes with Optics OTF $\alpha = 0.75$ and Hexagonal Sensor

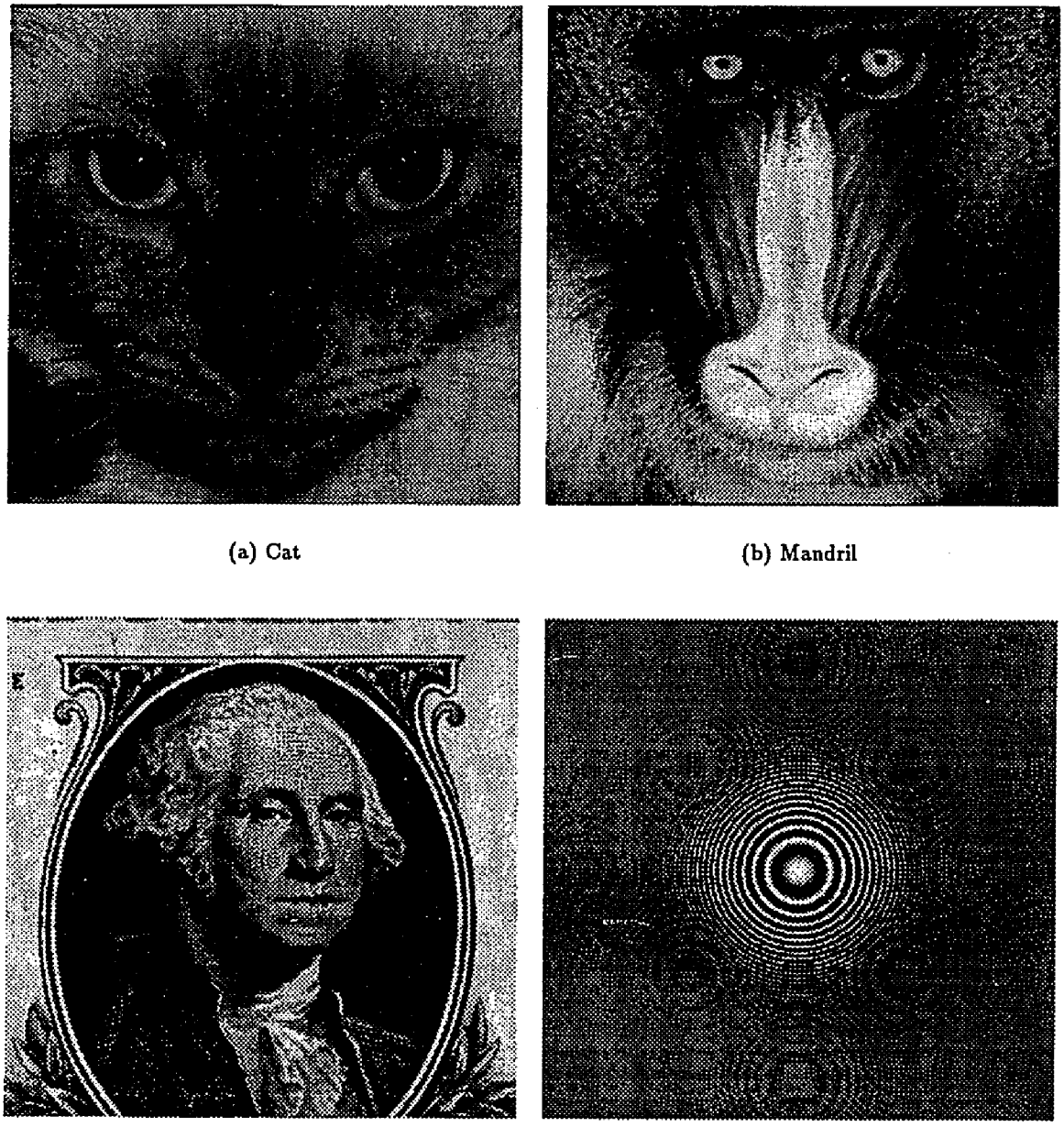

(a) Cat

(b) Mandril

(c) George

(d) Circles

Figure 5.11: Digital Scenes with Optics OTF $\alpha = 0.75$ and Rectangular Sensor

5.2.2 Sampling and Reconstruction Fidelity Loss

Sampling and reconstruction fidelity loss is defined in the frequency domain as

$$E\left[\|g - s'\|^2\right] = \epsilon_r^2 + \epsilon_s^2 \tag{5.6}$$

where:

$$\epsilon_s^2 = \sum_{\nu} \left| \frac{\hat{r}[\nu]}{|\det \mathbf{V}|} \right|^2 \sum_{\mathbf{k} \neq \mathbf{0}} \left| \hat{h}[\nu - \mathbf{Uk}] \hat{s}[\nu - \mathbf{Uk}] \right|^2 \tag{5.7}$$

$$\epsilon_r^2 = \sum_{\nu} \left| 1 - \frac{\hat{r}[\nu]}{|\det \mathbf{V}|} \right|^2 \left| \hat{h}[\nu] \hat{s}[\nu] \right|^2 . \tag{5.8}$$

ϵ_s^2 Fidelity Loss Component

The ϵ_s^2 term, as defined by equation 5.7, is a measure of the fidelity loss caused by folding of significant image energy at frequencies beyond the Nyquist limit into lower frequencies where $\hat{r}[\nu] \neq 0$. As indicated in the previous chapter, the ideal reconstruction function $\hat{r}[\nu] \neq 0$ over the baseband for the given sampling geometry and $\hat{r}[\nu] = 0$ elsewhere. The display reconstruction function has a much smaller area where $\hat{r}[\nu]$ is significantly greater than 0.

Inclusion of the sensor OTF significantly reduces the absolute ϵ_s^2 values and also significantly impacts the relative differences in favor of hexagonal sampling. This is a predictable result because ϵ_s^2 is a measure of the high frequency image energy being folded back into lower frequencies and the sensor OTFs filter out a considerable amount of high frequency energy as shown in figures 5.12 and 5.13 with the hexagonal sensor OTF filtering out slightly more high frequency energy than the rectangular sensor OTF.

ϵ_r^2 Fidelity Loss Component

The ϵ_r^2 term, as defined by equation 5.8 is a measure of the fidelity loss caused by the presence of significant image energy, $|\hat{h}[\nu]\hat{s}[\nu]|^2$, at frequencies where $\hat{r}[\nu] \neq |\det \mathbf{V}|$. For the ideal reconstruction functions, the values obtained for ϵ_r^2 (figures 5.16 and 5.17) are similar, but not identical, to the values obtained for ϵ_s^2 (figures 5.12 and 5.13). This is because while the reconstruction function has a value of $|\det \mathbf{V}|$ over the sampling baseband (Nyquist region) and a value of zero elsewhere, the pre-sampling image has energy outside the Nyquist region. ϵ_s^2 measures the amount of energy outside the Nyquist region, and ϵ_r^2 measures the amount of energy where $\hat{r}[\nu] \neq |\det \mathbf{V}|$, which define essentially the same regions. The display reconstruction function has only one point where $\hat{r}[\nu] = |\det \mathbf{V}|$, which is $\nu = [0, 0]$. This implies that for the digital scenes used ϵ_r^2 will always be greater than zero, which is displayed graphically in figures 5.18 and 5.19.

Sampling and Reconstruction Fidelity Loss

The sum $\epsilon_r^2 + \epsilon_s^2 = 0$ defines the conditions under which complete reconstruction of the pre-sampling image $g(\mathbf{x})$ from its sampled data is possible. Complete reconstruction can occur only when both ϵ_r^2 and ϵ_s^2 are simultaneously zero since both quantities are non-negative. As mentioned in chapter 3 the conditions required for complete reconstruction are:

1. $\hat{r}[\nu]$ must equal $|\det \mathbf{V}|$ over the region where the band-region of the pre-sampling image contains energy ($\hat{h}[\nu]\hat{s}[\nu] \neq 0$).

2. $\hat{r}[\nu]$ must equal zero over the region where the instances of the periodic extension of $\hat{g}[\nu]$ contain energy ($\hat{h}(\nu - \mathbf{Uk})\hat{s}(\nu - \mathbf{Uk}) \neq 0$).

3. The sampling matrix $\mathbf{V}$ (and hence the periodicity matrix $\mathbf{U}$) must be defined such that adjacent instances of the periodic extension of $\hat{g}[\nu]$ ($\hat{h}(\nu - \mathbf{Uk})\hat{s}(\nu - \mathbf{Uk})$) do not overlap.

For the band-limited scenes used in the previous chapter, the ideal reconstruction functions meet all three of the above conditions as long as the scene band-region radius is less than the Nyquist limit, i.e. $R = 0.125$. The digital scenes used in this chapter are not limited to a band-region that is less than the Nyquist limit, and the image formation OTFs used do not completely remove high frequency information outside the Nyquist region. This implies that for the digital images used there will always be some sampling and reconstruction fidelity loss, even when using an ideal reconstruction function, which is borne out in figures 5.20 and 5.21. For this reason and recalling that for any scene band-region radius greater than zero, the display reconstruction function does not meet the above conditions for complete reconstruction of the pre-sampling image, it is apparent that the display reconstruction function will also always induce some degree of sampling and reconstruction fidelity loss. This is shown in figures 5.22 and 5.23.

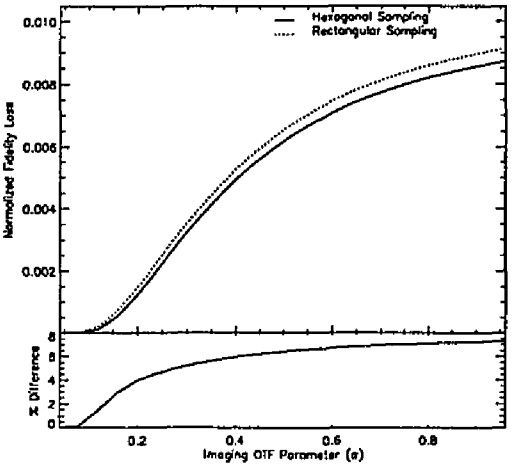

(a) Cat

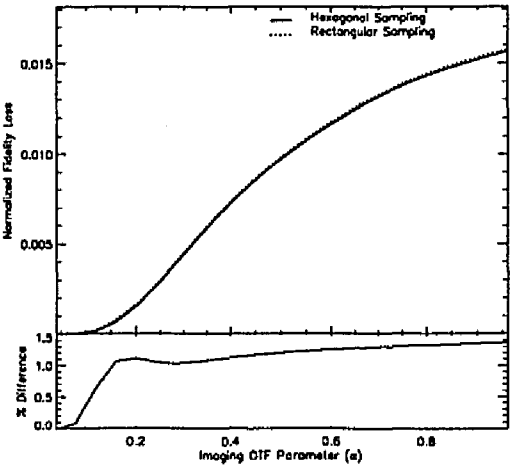

(b) Mandril

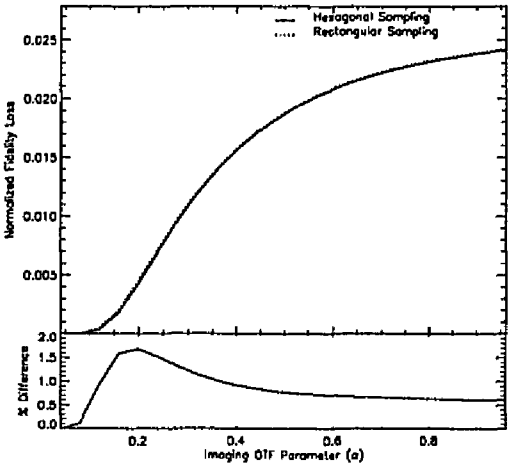

(c) George

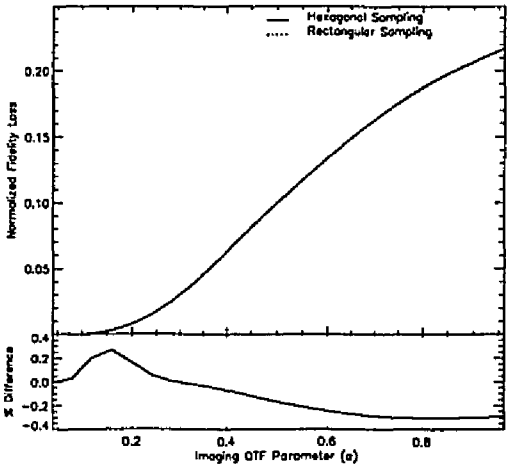

(d) Circles

Figure 5.12: ϵ_s^2 Fidelity Loss Component - No Sensor OTF - Ideal Reconstruction

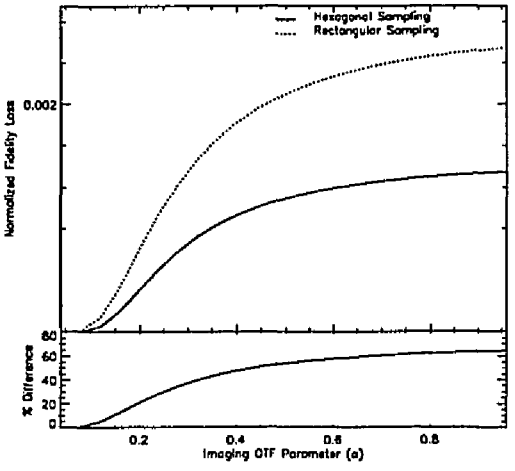

(a) Cat

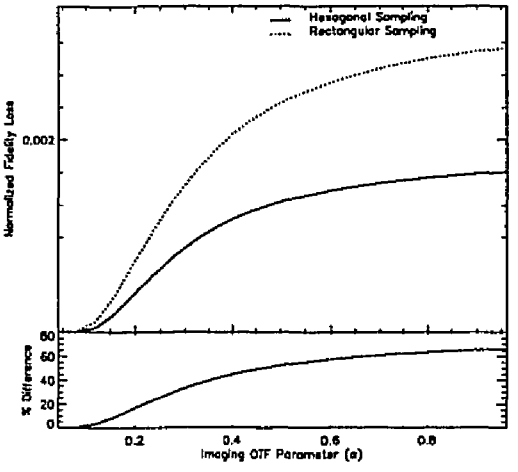

(b) Mandril

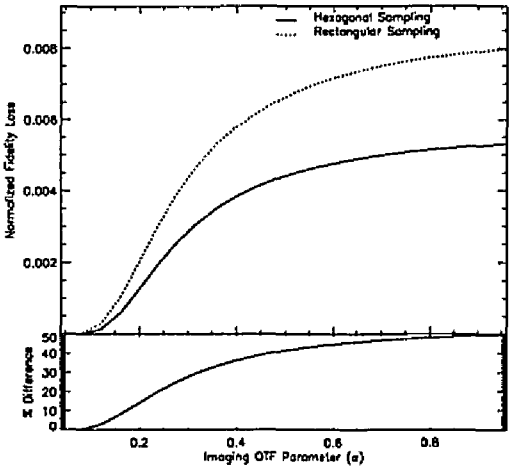

(c) George

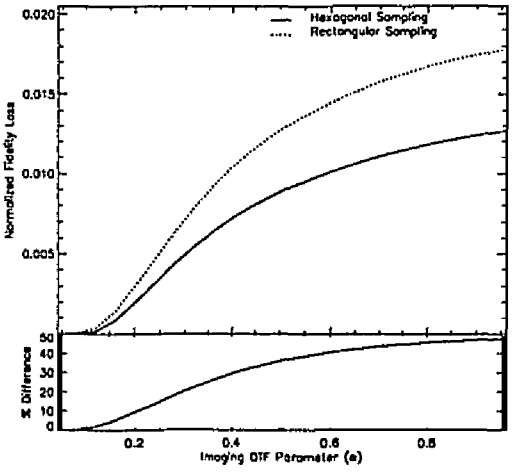

(d) Circles

Figure 5.13: ϵ_s^2 Fidelity Loss Component - Sensor OTF - Ideal Reconstruction

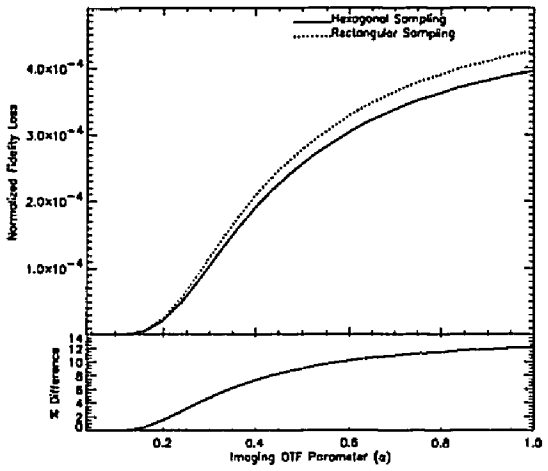

(a) Cat

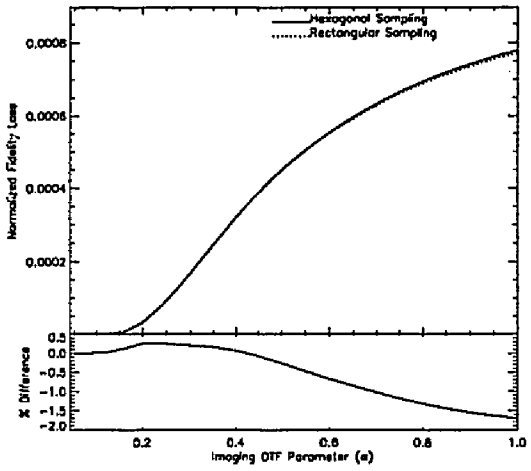

(b) Mandril

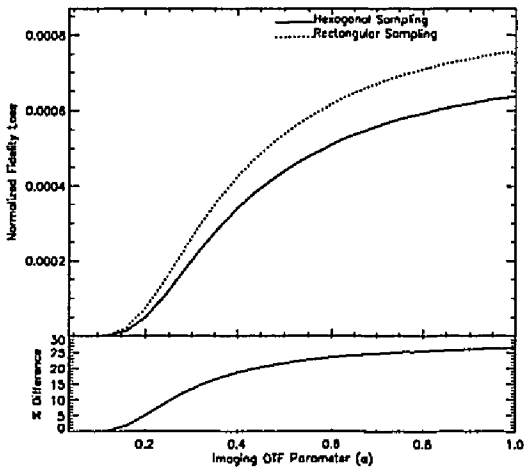

(c) George

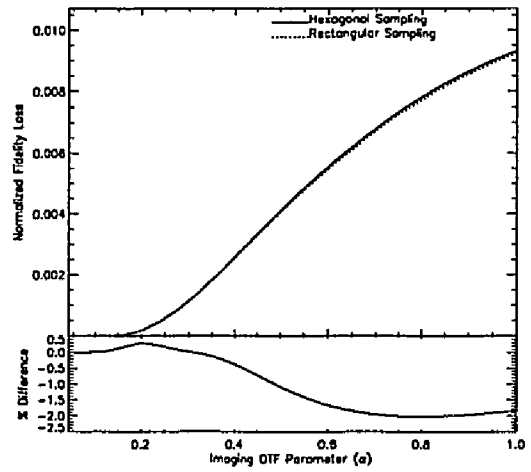

(d) Circles

Figure 5.14: ϵ_s^2 Fidelity Loss Component - No Sensor OTF - Display Reconstruction

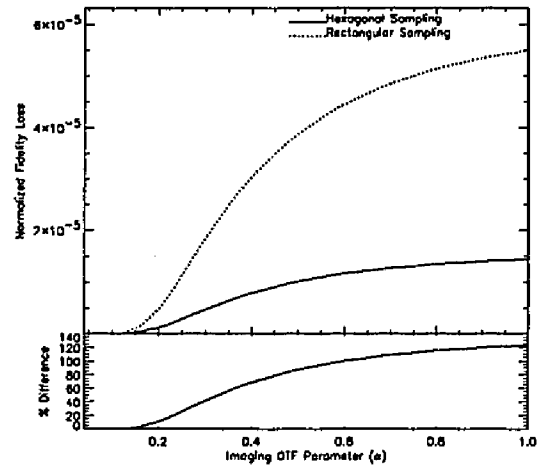

(a) Cat

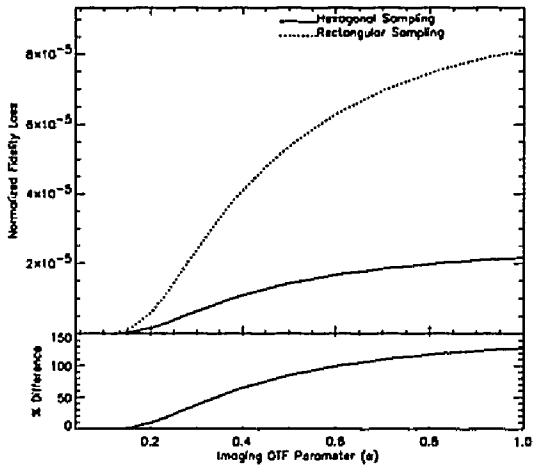

(b) Mandril

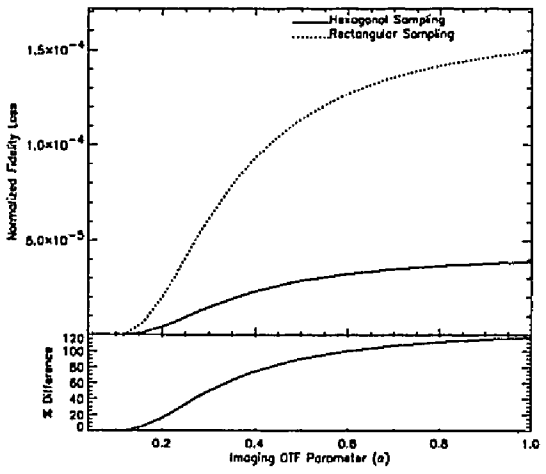

(c) George

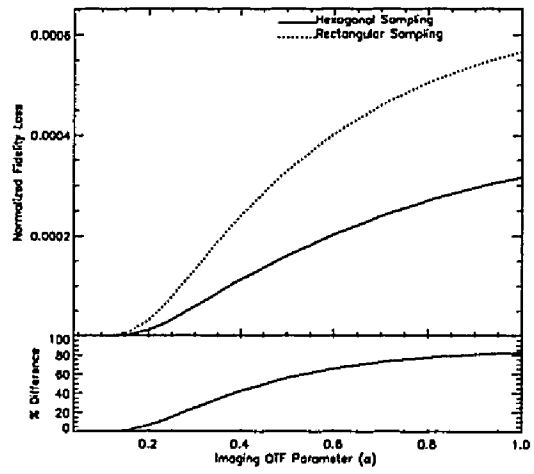

(d) Circles

Figure 5.15: ϵ_s^2 Fidelity Loss Component - Sensor OTF - Display Reconstruction

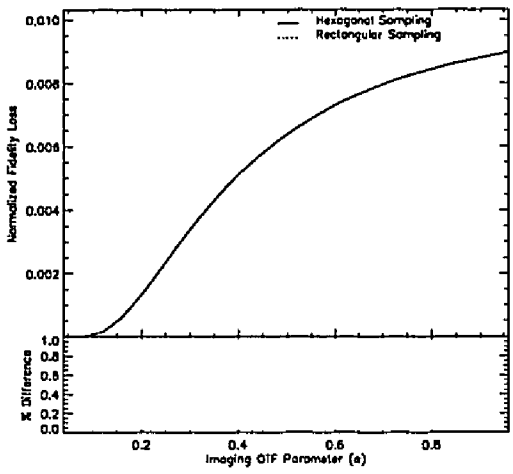

(a) Cat

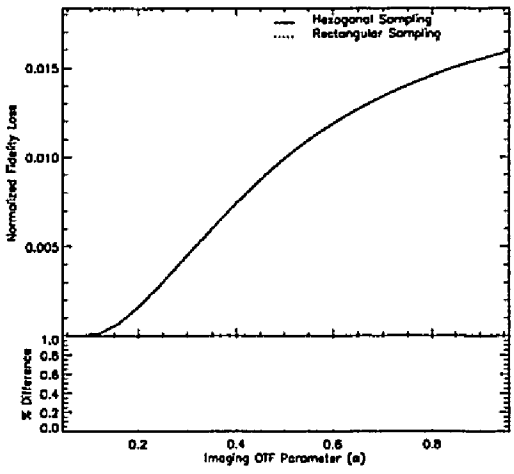

(b) Mandril

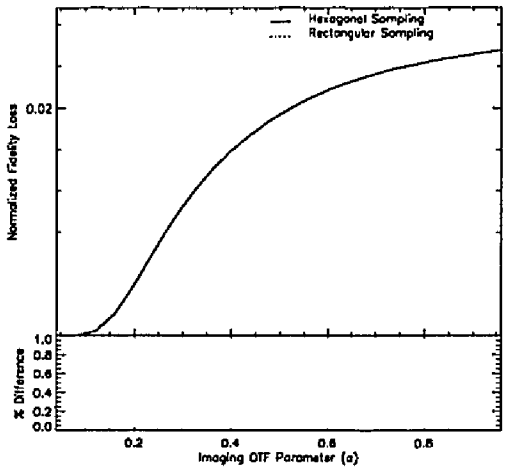

(c) George

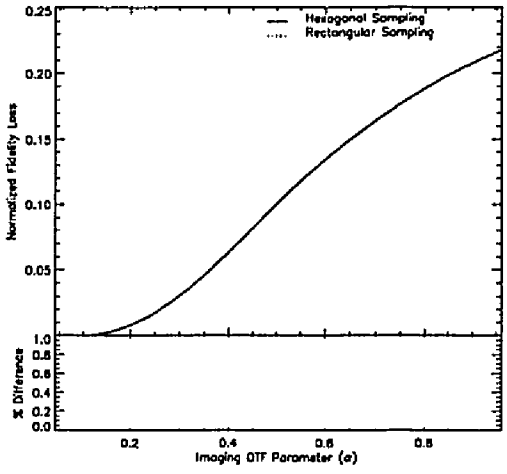

(d) Circles

Figure 5.16: ϵ_r^2 Fidelity Loss Component - No Sensor OTF -Ideal Reconstruction

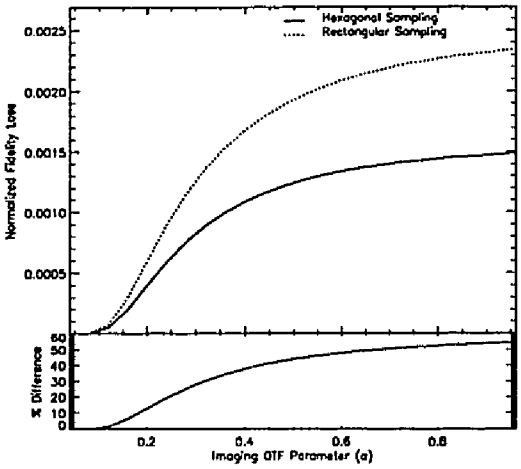

(a) Cat

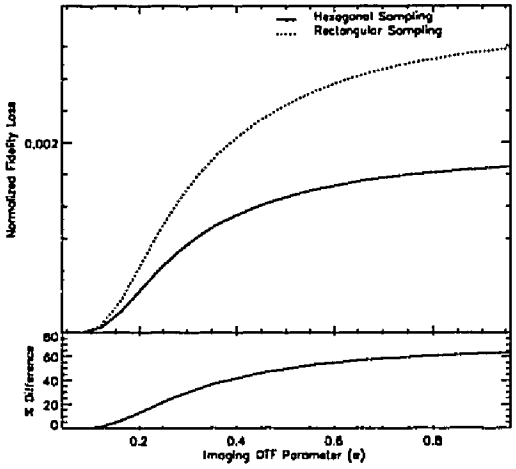

(b) Mandril

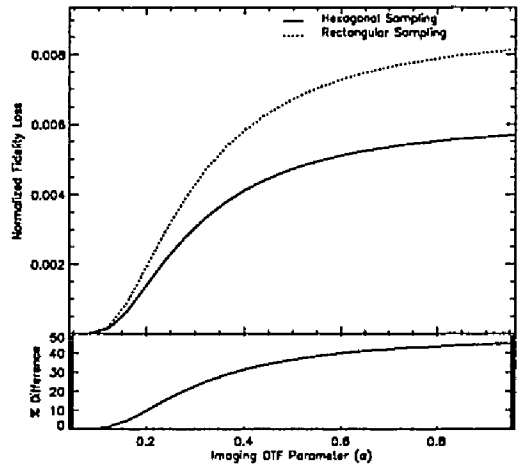

(c) George

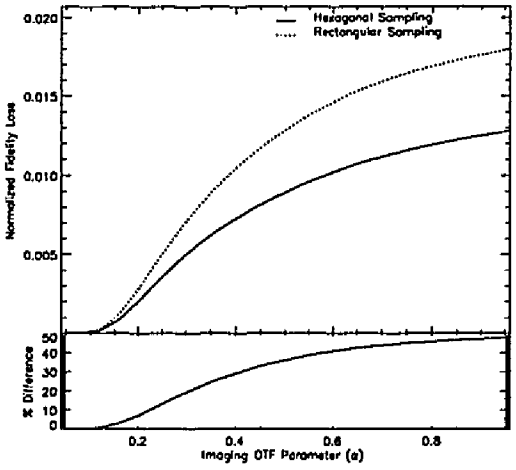

(d) Circles

Figure 5.17: ϵ_r^2 Fidelity Loss Component - Sensor OTF - Ideal Reconstruction

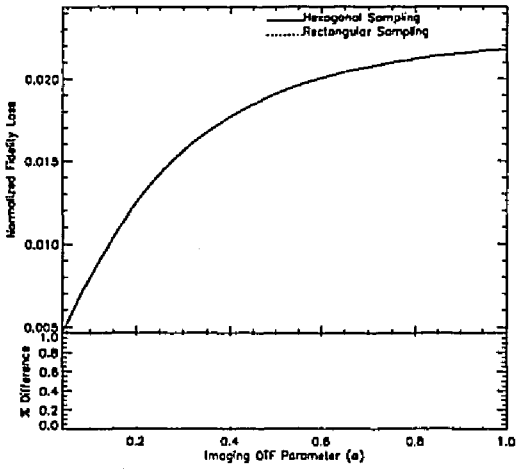

(a) Cat

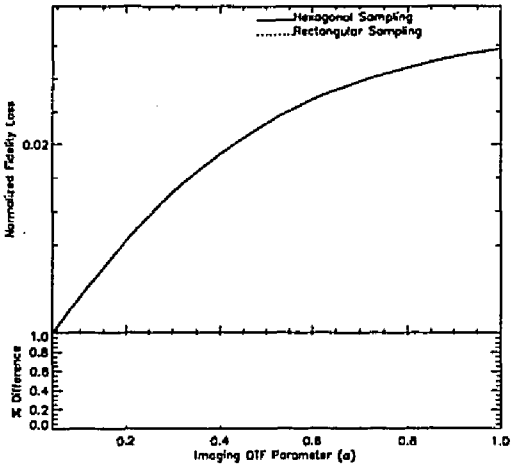

(b) Mandril

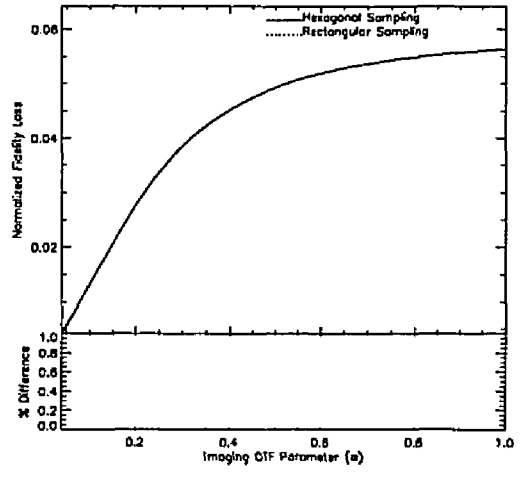

(c) George

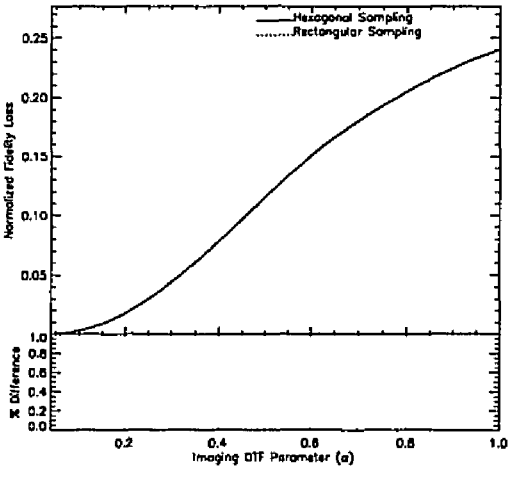

(d) Circles

Figure 5.18: ϵ_r^2 Fidelity Loss Component - No Sensor OTF - Display Reconstruction

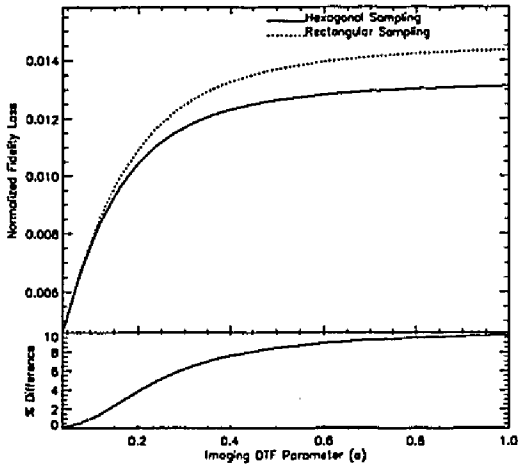

(a) Cat

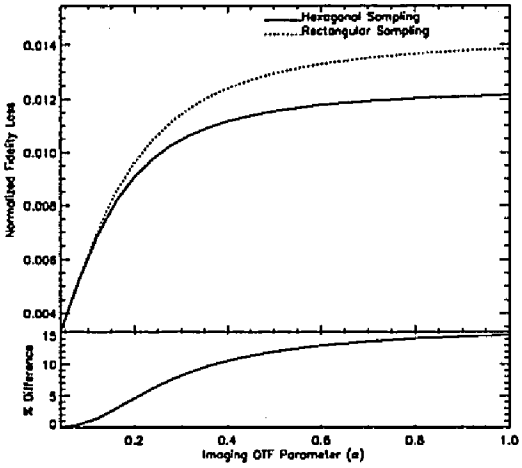

(b) Mandril

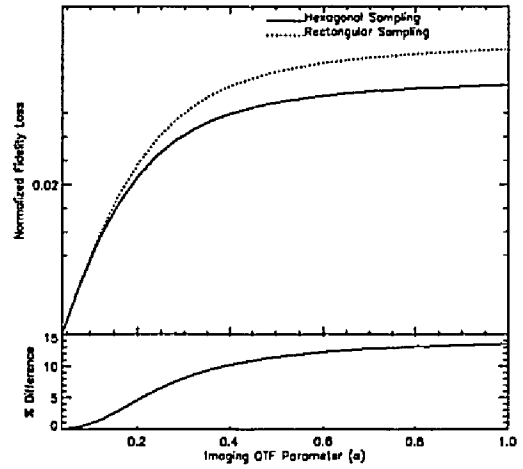

(c) George

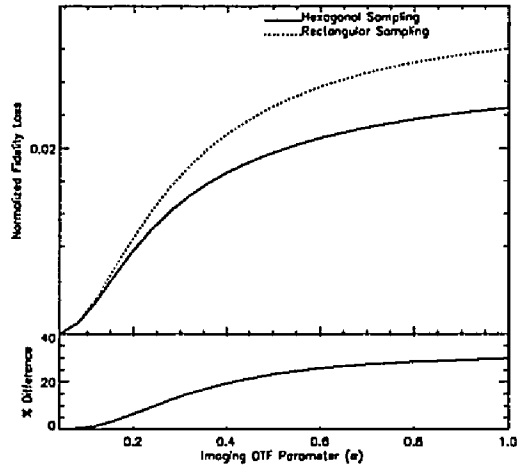

(d) Circles

Figure 5.19: ϵ_r^2 Fidelity Loss Component - Sensor OTF - Display Reconstruction

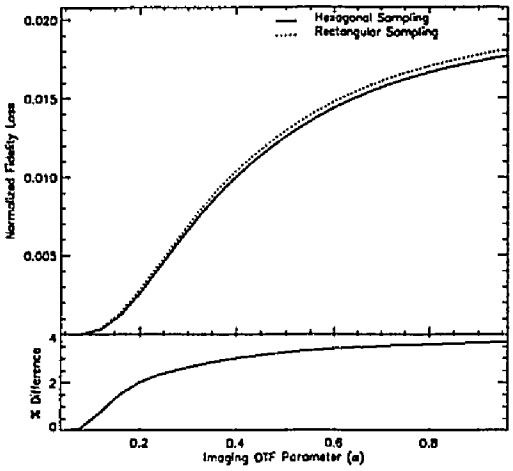

(a) Cat

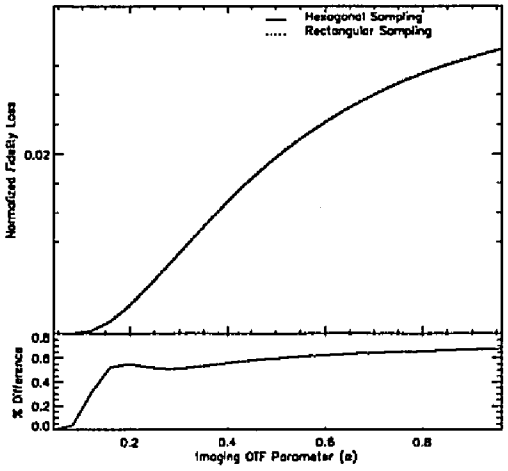

(b) Mandril

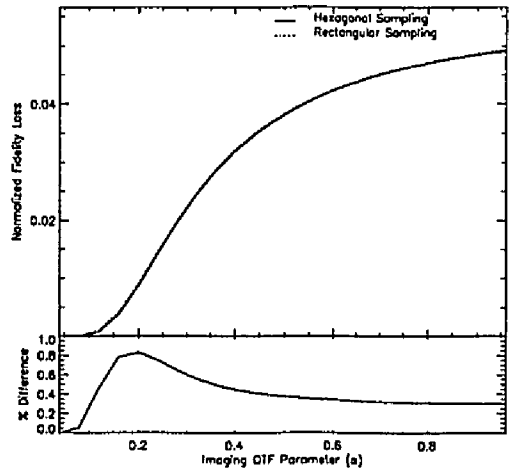

(c) George

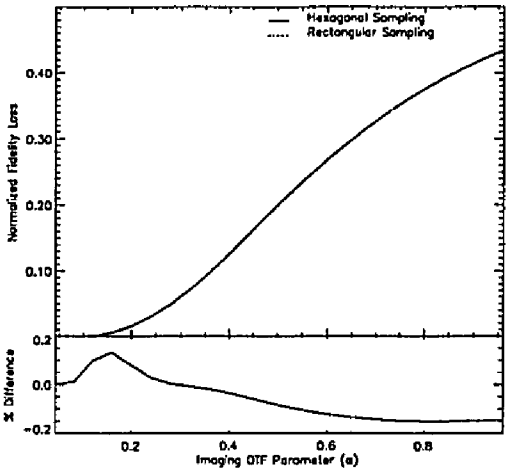

(d) Circles

Figure 5.20: Sampling and Reconstruction Fidelity Loss - No Sensor OTF - Ideal Reconstruction

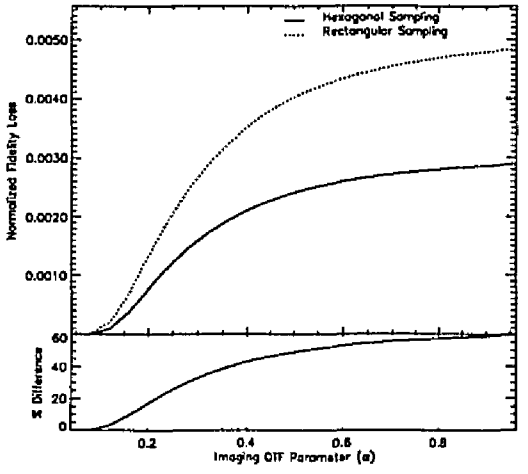

(a) Cat

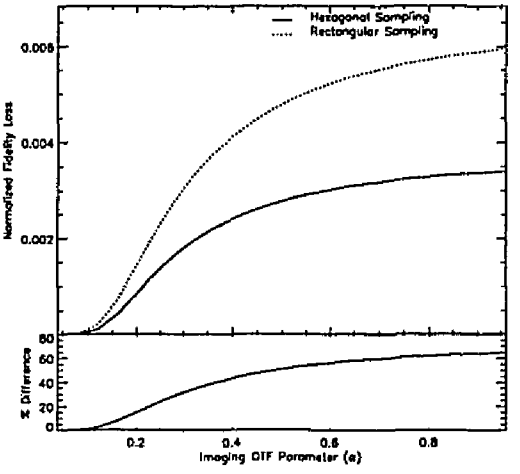

(b) Mandril

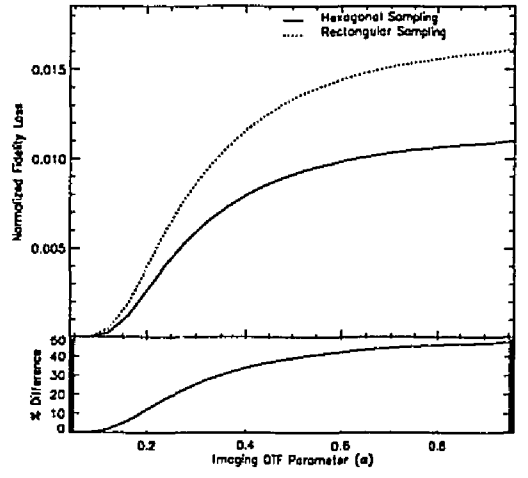

(c) George

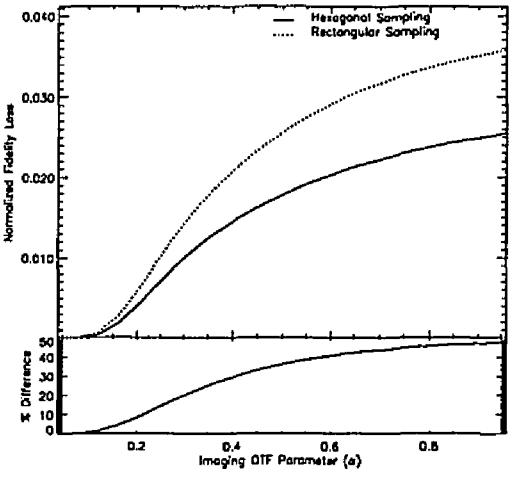

(d) Circles

Figure 5.21: Sampling and Reconstruction Fidelity Loss - Sensor OTF - Ideal Reconstruction

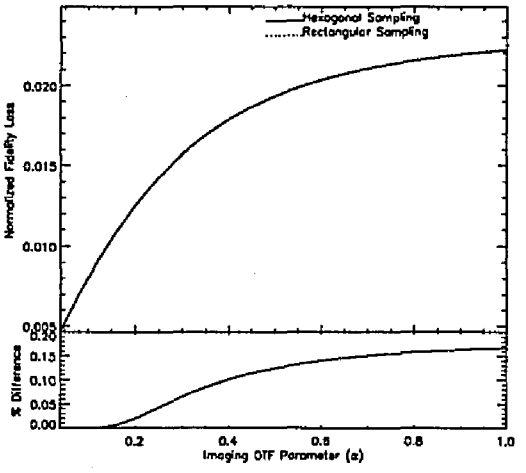

(a) Cat

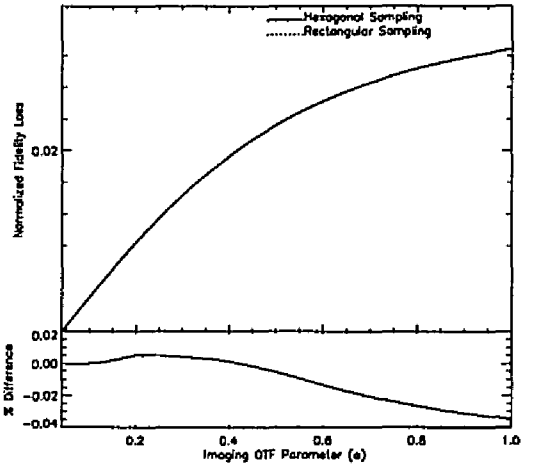

(b) Mandril

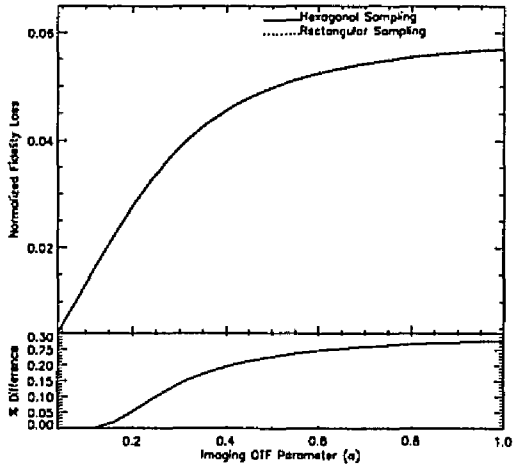

(c) George

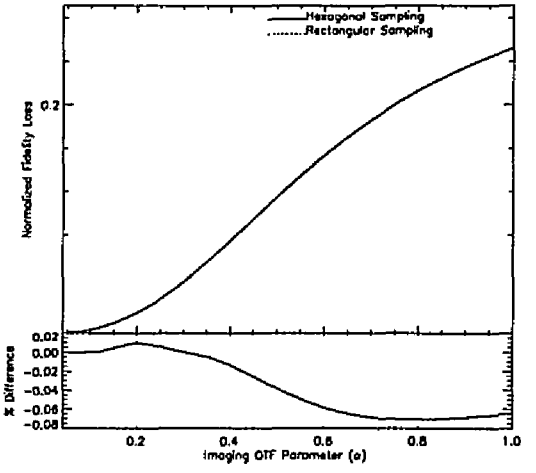

(d) Circles

Figure 5.22: Sampling and Reconstruction Fidelity Loss - No Sensor OTF - Display Reconstruction

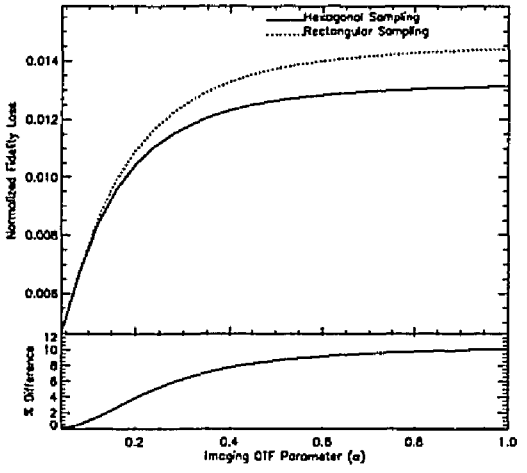

(a) Cat

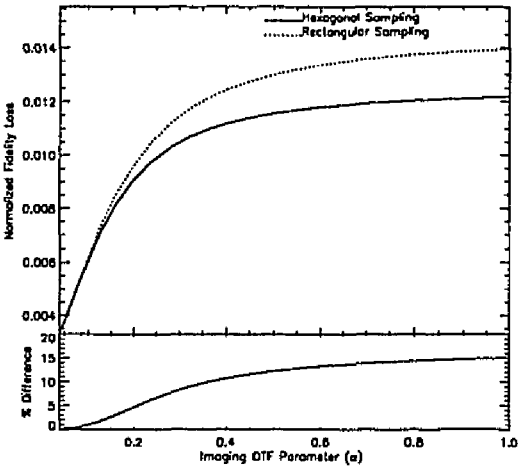

(b) Mandril

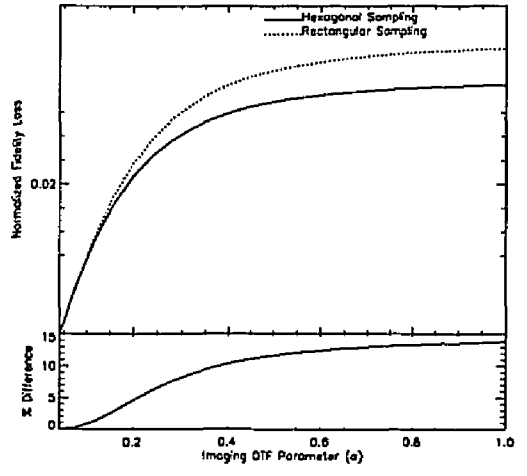

(c) George

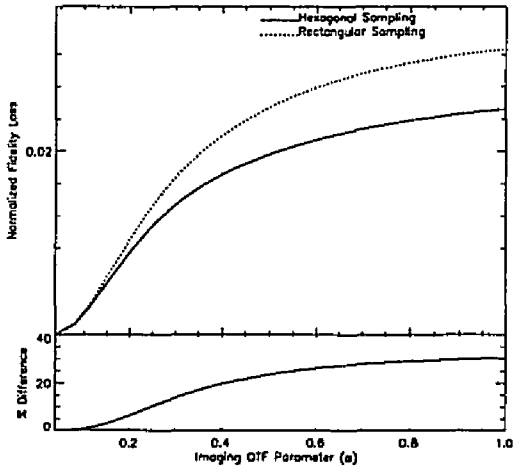

(d) Circles

Figure 5.23: Sampling and Reconstruction Fidelity Loss - Sensor OTF - Display Reconstruction

5.2.3 End-to-End Fidelity Loss

End-to-end fidelity loss is defined in the frequency domain as

$$E\left[\|s - s'\|^2\right] = \epsilon_e^2 + \epsilon_s^2 \tag{5.9}$$

where

$$\epsilon_e^2 = \sum_{\nu} \left|1 - \frac{\hat{r}[\nu]}{|\det \mathbf{V}|}\hat{h}[\nu]\right|^2 |\hat{s}[\nu]|^2 . \tag{5.10}$$

and ϵ_s^2 is given in equation (5.7).

ϵ_e^2 Fidelity Loss Component

The term ϵ_e^2 accounts for the end-to-end loss of fidelity caused by significant scene energy $|\hat{s}[\nu]|^2$ at frequencies where the cascaded response $\hat{r}[\nu]\hat{h}[\nu] \neq |\det \mathbf{V}|$. ϵ_e^2 measures how well the reconstruction function $\hat{r}[\nu]$ is able to restore the frequencies that were suppressed prior to sampling by the image gathering OTF $\hat{h}[\nu]$. The cascaded response $\hat{r}[\nu]\hat{h}[\nu]$, where $\hat{r}[\nu]$ is the ideal reconstruction function and $\hat{h}[\nu]$ has no sensor OTF component, has a value close to $|\det \mathbf{V}|$ over the Nyquist region. This accounts for the low ϵ_e^2 fidelity loss for values of $\alpha > 0.25$ as shown in figure 5.24. The composite OTFs in figure 5.3 decrease much more rapidly with increasing frequency compared to the lens OTF, which accounts for the much lower value of R at which ϵ_e^2 fidelity loss becomes apparent, as shown in figure 5.25.

The ϵ_e^2 results obtained for the display reconstruction function, figures 5.26 and 5.27, are analogous to those obtained for ϵ_r^2 in figures 5.18 and 5.19. As was the case for ϵ_r^2, this is primarily because the display reconstruction function has only one point where $\hat{r}[\nu] = |\det \mathbf{V}|$, $\nu = [0,0]$, which implies that for digital scenes that are not band-limited ϵ_e^2 will always be greater than zero.

End–to–End Fidelity Loss

Analogous to the individual terms for sampling/reconstruction fidelity loss ϵ_e^2 and ϵ_s^2 are both non-negative quantities. In order to have zero end-to-end fidelity loss, both ϵ_e^2 and ϵ_s^2 must be simultaneously zero. As mentioned in chapter 3 the sum $\epsilon_e^2 + \epsilon_s^2 = 0$ defines the conditions necessary for complete reconstruction of the original scene $s(\mathbf{x})$ to occur.

1. The cascaded response $\hat{r}[\nu]\hat{h}[\nu]$ must equal $|\det \mathbf{V}|$ over the region where the band-region of the original scene contains energy ($\hat{s}[\nu] \neq 0$).

2. $\hat{r}[\nu]$ must equal zero over the region where the instances of the periodic extension of $\hat{g}[\nu]$ contain energy ($\hat{h}(\nu - \mathbf{Uk})\hat{s}(\nu - \mathbf{Uk}) \neq 0$).

3. The sampling matrix $\mathbf{V}$ (and hence the periodicity matrix $\mathbf{U}$) must be defined such that adjacent instances of the periodic extension of $\hat{g}[\boldsymbol{\nu}]$ ($\hat{h}(\boldsymbol{\nu} - \mathbf{Uk})\hat{s}(\boldsymbol{\nu} - \mathbf{Uk})$) do not overlap.

Unlike the band-limited scenes used in chapter 4, the digital scenes used in this chapter contain significant energy at points where $\hat{r}[\boldsymbol{\nu}]\hat{h}[\boldsymbol{\nu}]$ differs from $|\det \mathbf{V}|$. Additionally the periodic extensions of the pre-sampling image, $\hat{g}(\boldsymbol{\nu} - \mathbf{Uk})$, contain energy in some regions where $\hat{r}[\boldsymbol{\nu}] \neq 0$. Finally, some of the adjacent instances of the periodic extensions of the pre-sampling image overlap, folding energy at high frequencies back into lower frequencies. This is shown in figures 5.28 and 5.29.

In chapter 4 we observed that for any scene band-region radius greater than zero the display reconstruction function does not meet the conditions for complete reconstruction of the original scene. Since the digital scenes used in this chapter all have significant levels of energy at points other than $\boldsymbol{\nu} = [0, 0]$, it is apparent that the display reconstruction function will induce significant levels of fidelity loss, as shown in figures 5.30 and 5.31. These figures also show that there is very little end–to–end fidelity loss difference between hexagonal and rectangular sampling when used with the display reconstruction function. Any gains realized by the use of hexagonal sampling is completely negated by the display reconstruction function. While there is very little end–to–end fidelity loss difference between hexagonal and rectangular sampling, there is a visible difference in the pattern of the artifacts in figures 5.40 through 5.47.

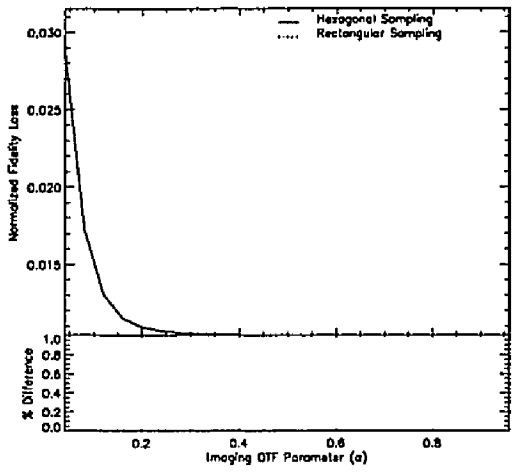

(a) Cat

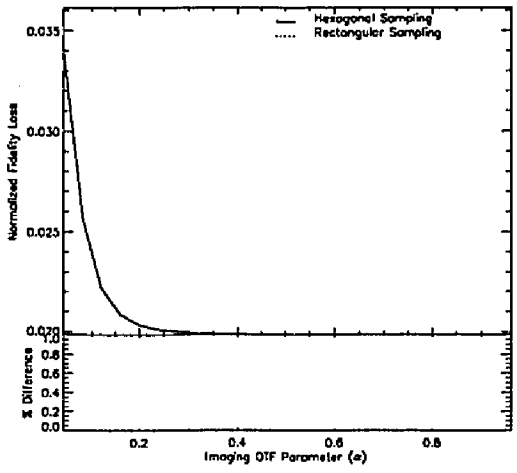

(b) Mandril

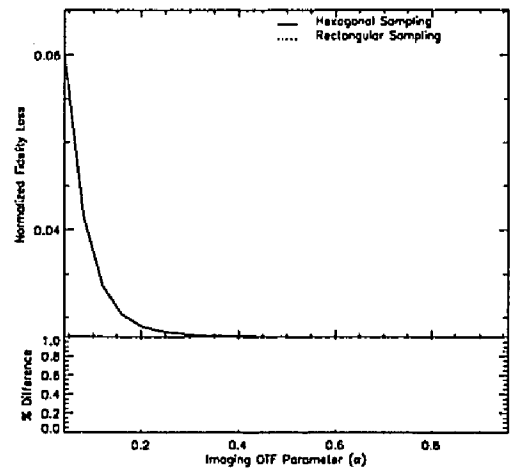

(c) George

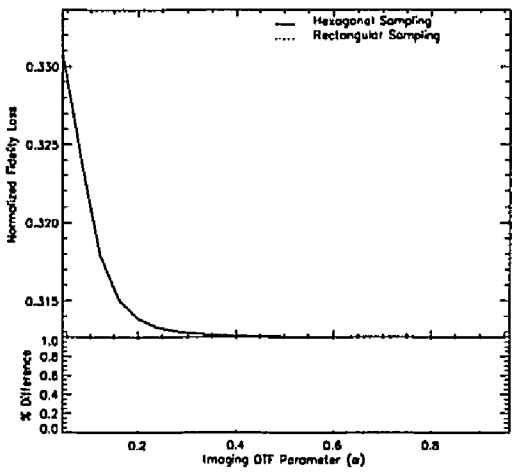

(d) Circles

Figure 5.24: ϵ_e^2 Fidelity Loss Component - No Sensor OTF - Ideal Reconstruction

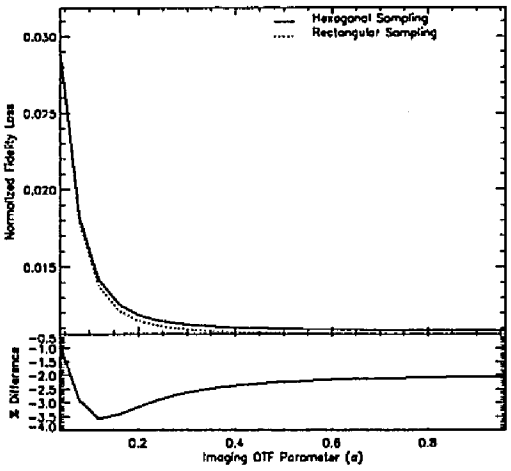

(a) Cat

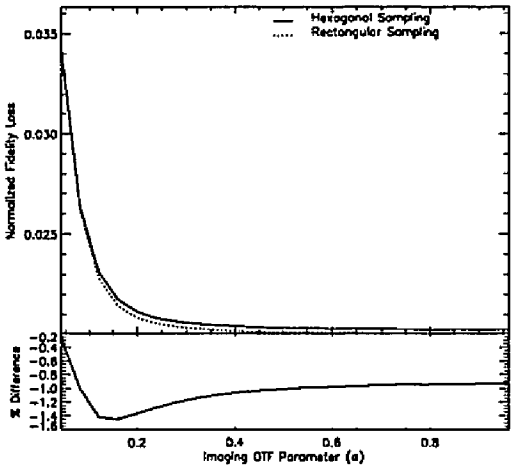

(b) Mandril

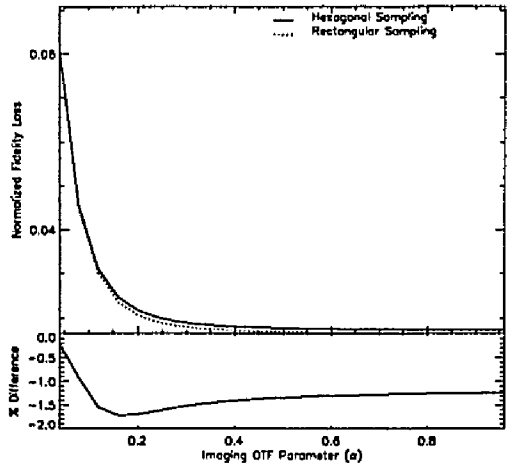

(c) George

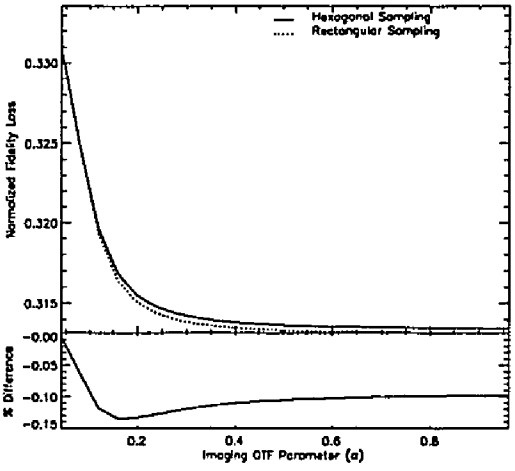

(d) Circles

Figure 5.25: ϵ_e^2 Fidelity Loss Component - Sensor OTF - Ideal Reconstruction

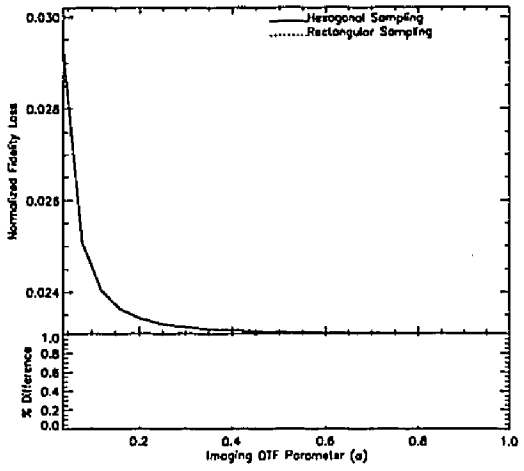

(a) Cat

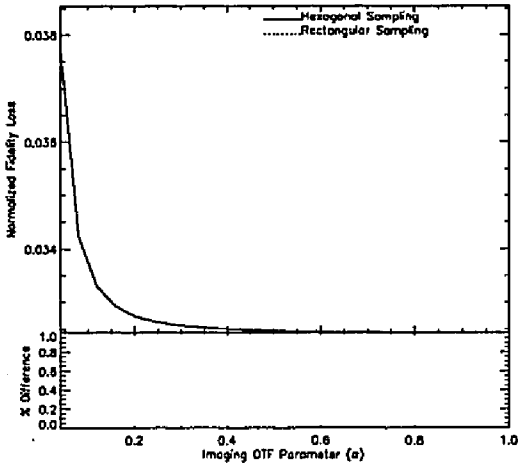

(b) Mandril

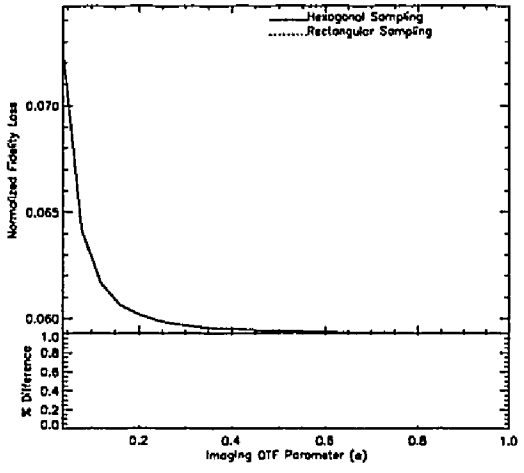

(c) George

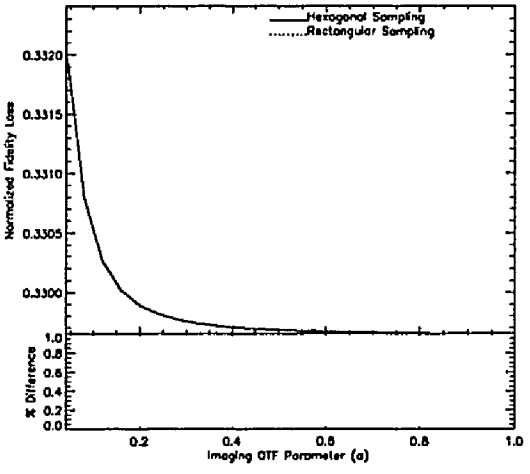

(d) Circles

Figure 5.26: ϵ_e^2 Fidelity Loss Component - No Sensor OTF - Display Reconstruction

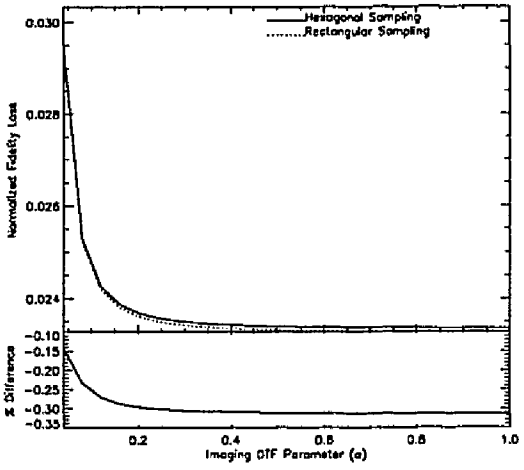

(a) Cat

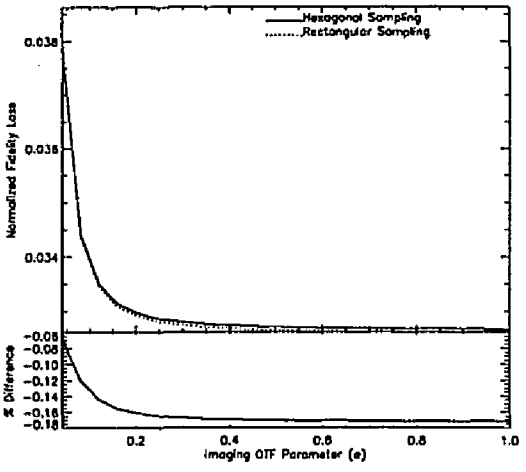

(b) Mandril

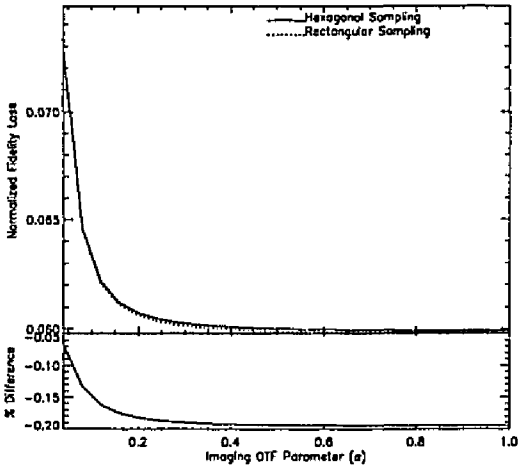

(c) George

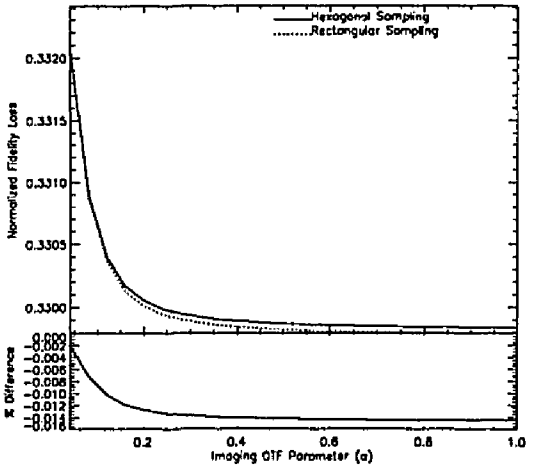

(d) Circles

Figure 5.27: ϵ_e^2 Fidelity Loss Component - Sensor OTF - Display Reconstruction

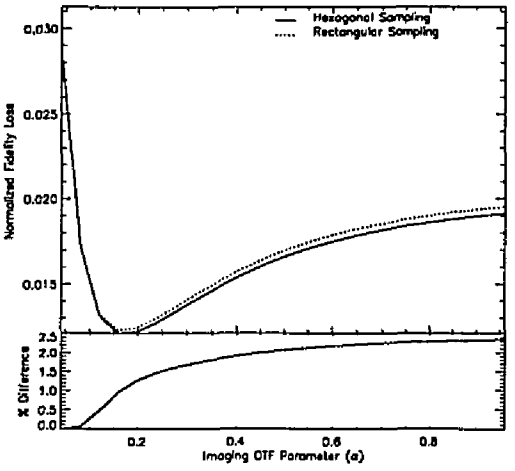

(a) Cat

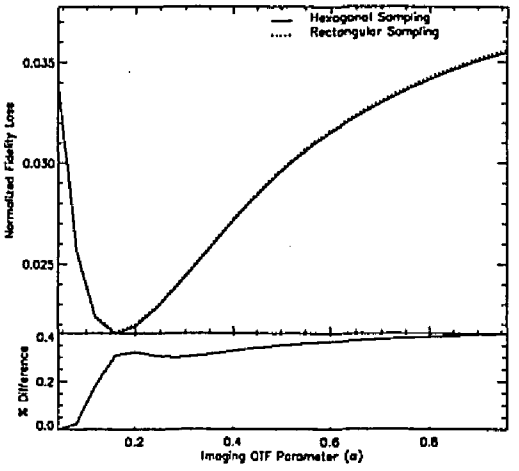

(b) Mandril

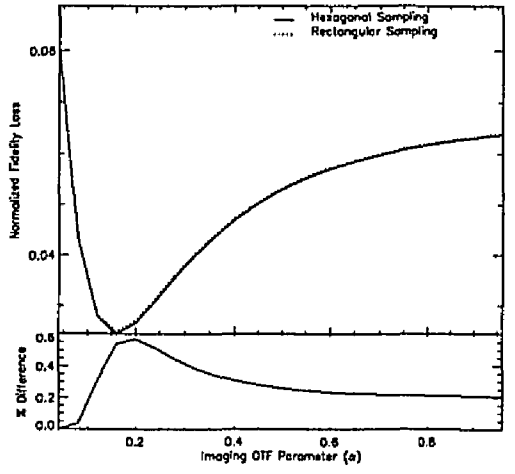

(c) George

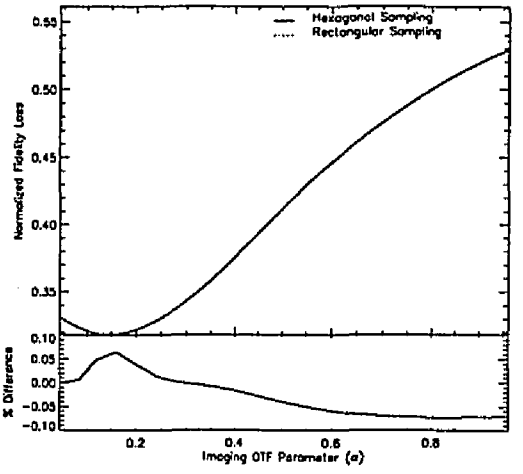

(d) Circles

Figure 5.28: End-to-End Fidelity Loss - No Sensor OTF - Ideal Reconstruction

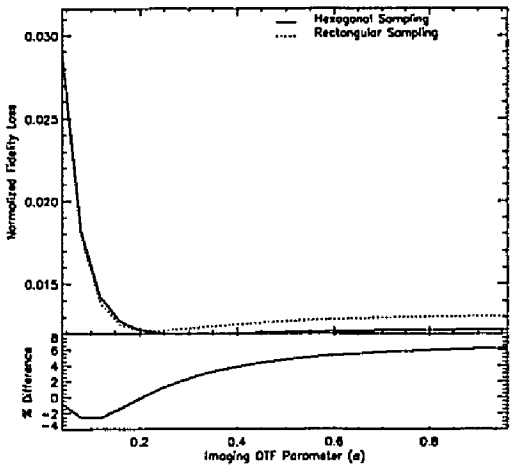

(a) Cat

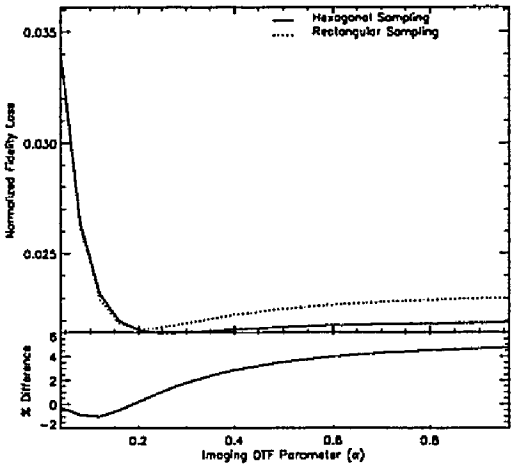

(b) Mandril

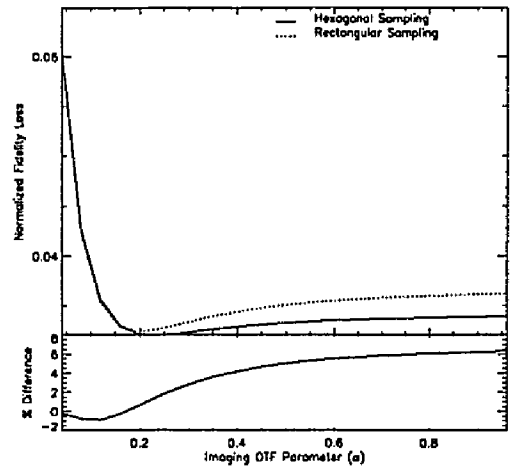

(c) George

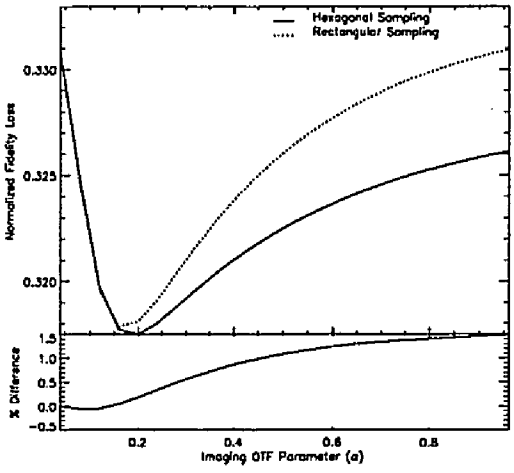

(d) Circles

Figure 5.29: End-to-End Fidelity Loss - Sensor OTF - Ideal Reconstruction

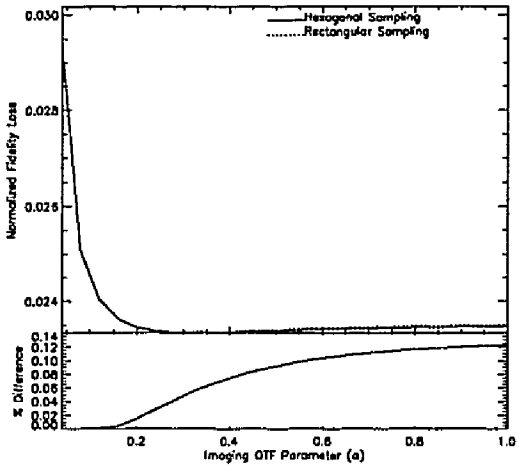

(a) Cat

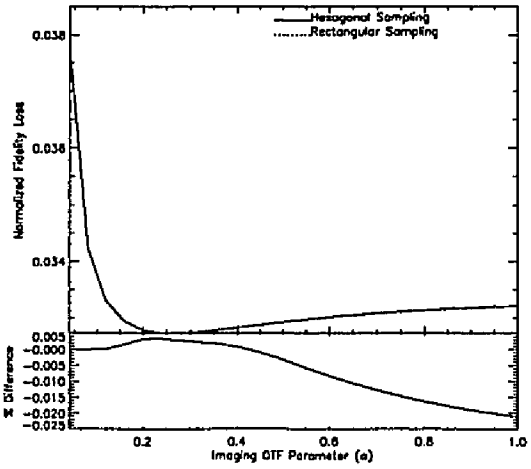

(b) Mandril

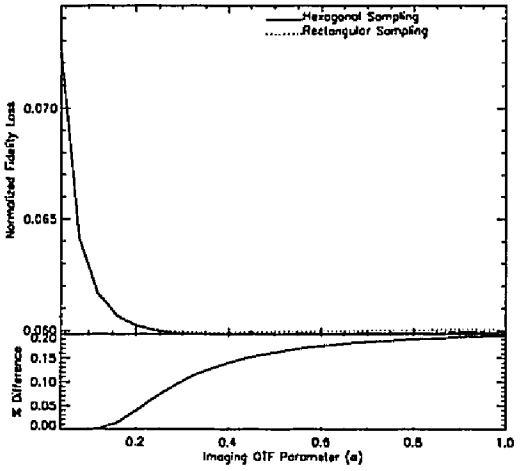

(c) George

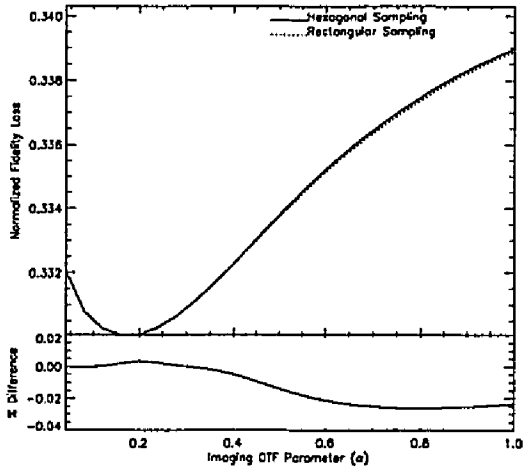

(d) Circles

Figure 5.30: End-to-End Fidelity Loss - No Sensor OTF - Display Reconstruction

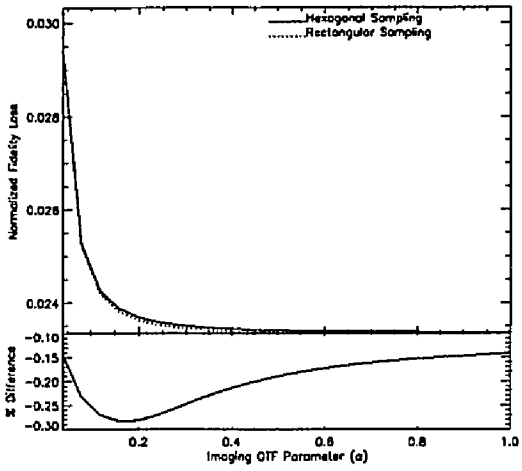

(a) Cat

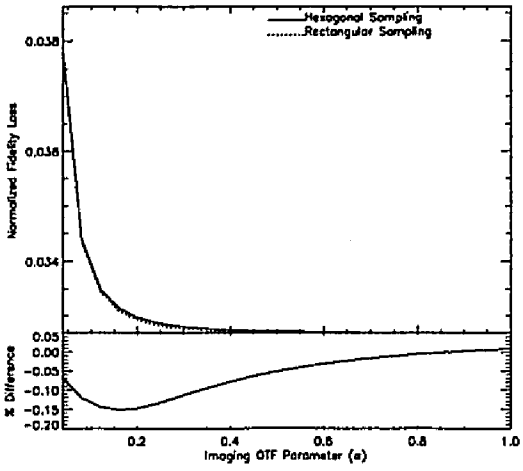

(b) Mandril

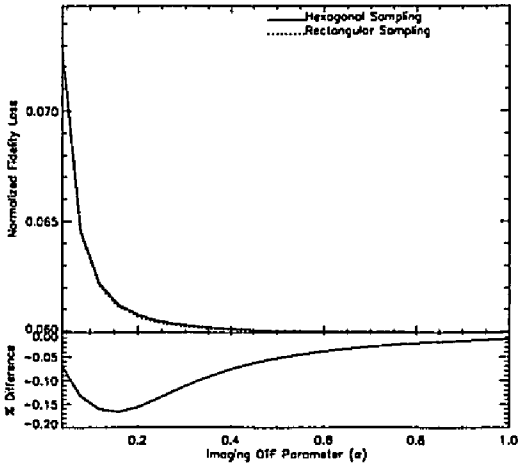

(c) George

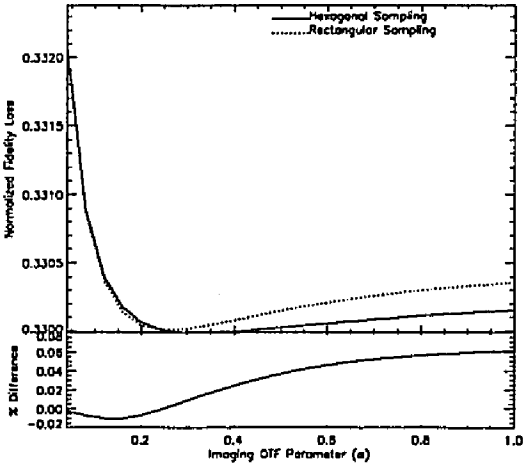

(d) Circles

Figure 5.31: End-to-End Fidelity Loss - Sensor OTF - Display Reconstruction

5.2.4 Reconstructed Images

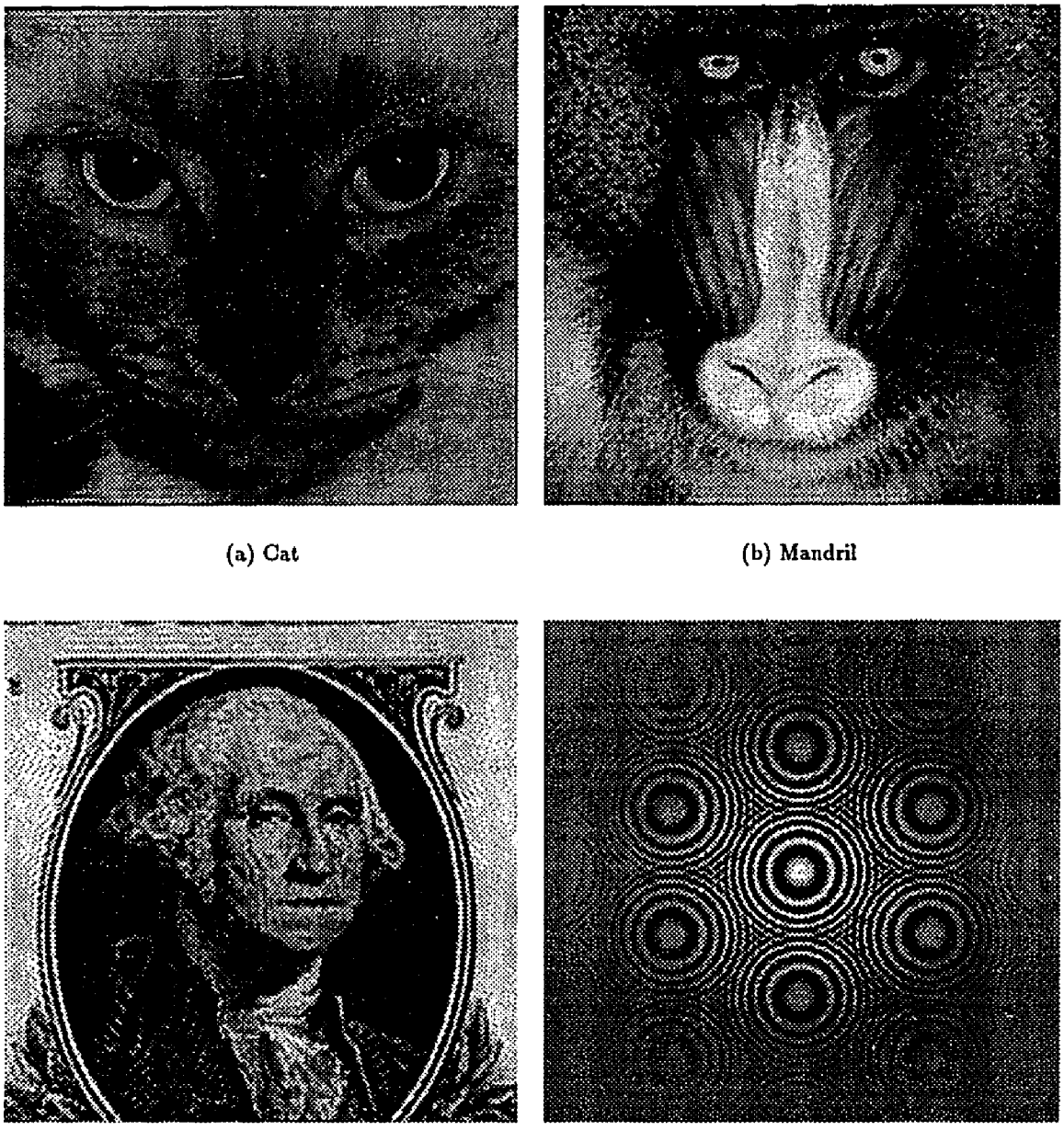

(a) Cat

(b) Mandril

(c) George

(d) Circles

Figure 5.32: No Sensor OTF - $\alpha = 0.25$ - Hexagonal Sampling - Ideal Reconstruction

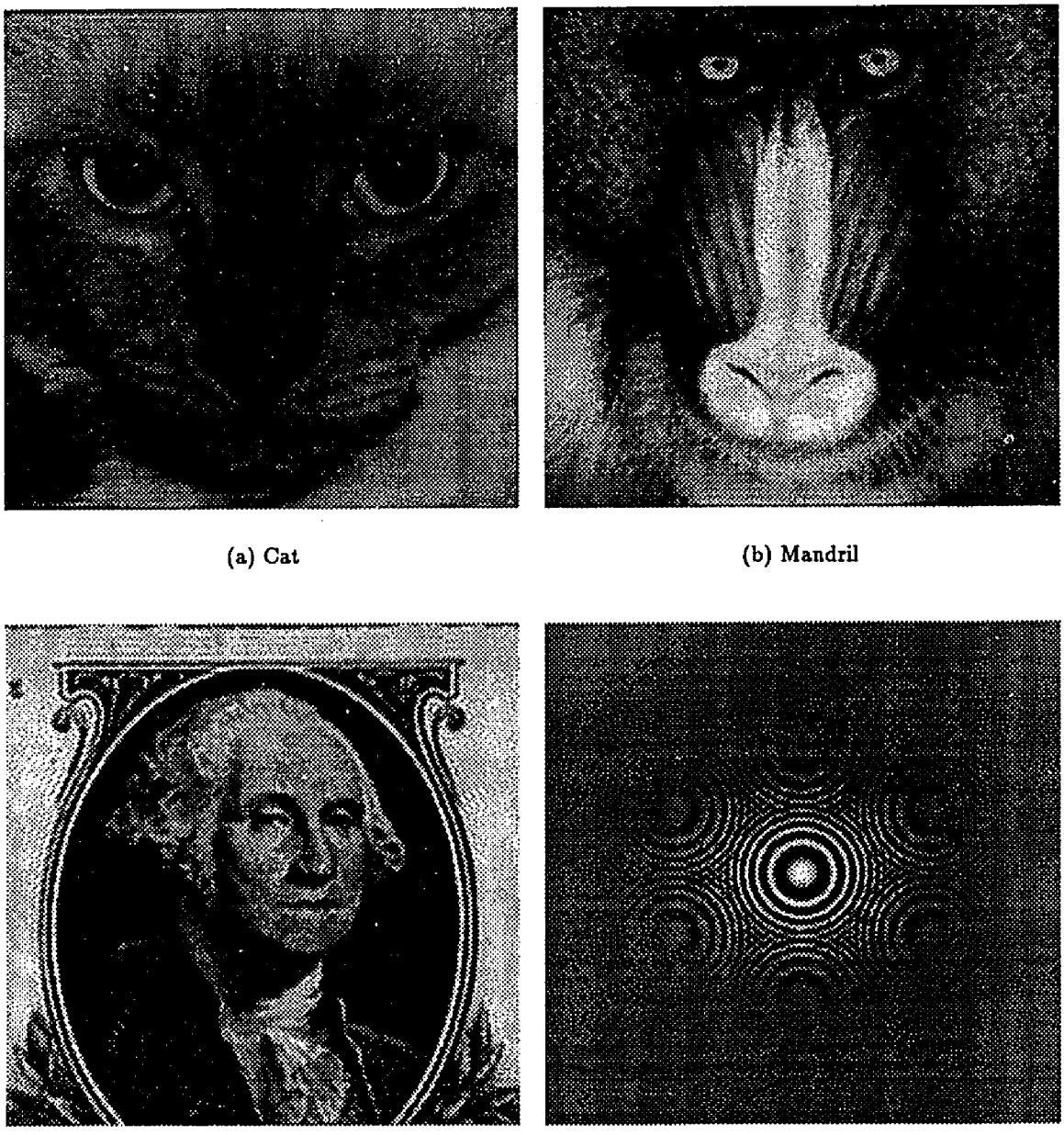

(a) Cat

(b) Mandril

(c) George

(d) Circles

Figure 5.33: Sensor OTF - $\alpha = 0.25$ - Hexagonal Sampling - Ideal Reconstruction

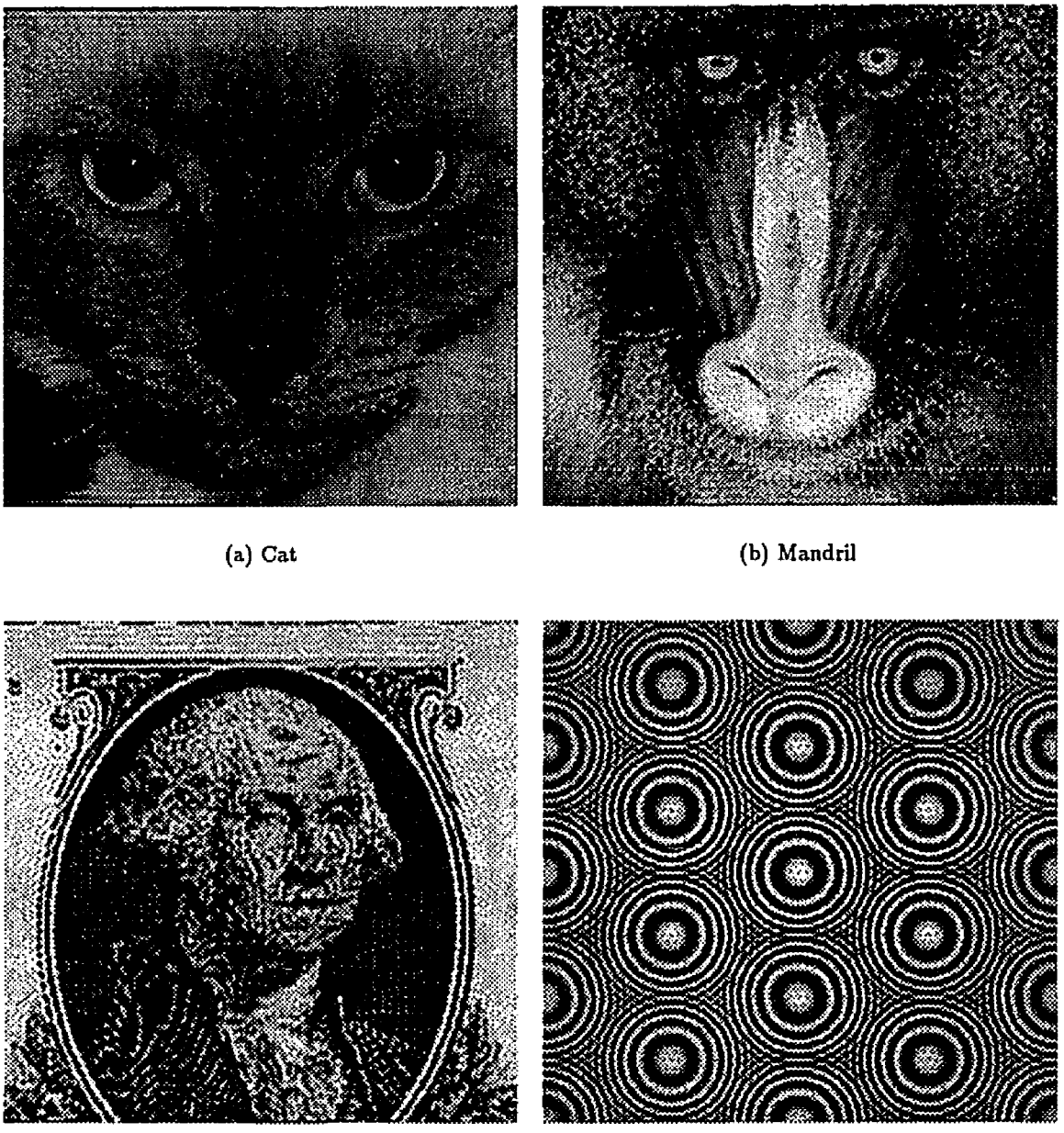

(a) Cat

(b) Mandril

(c) George

(d) Circles

Figure 5.34: No Sensor OTF - $\alpha = 0.75$ - Hexagonal Sampling - Ideal Reconstruction

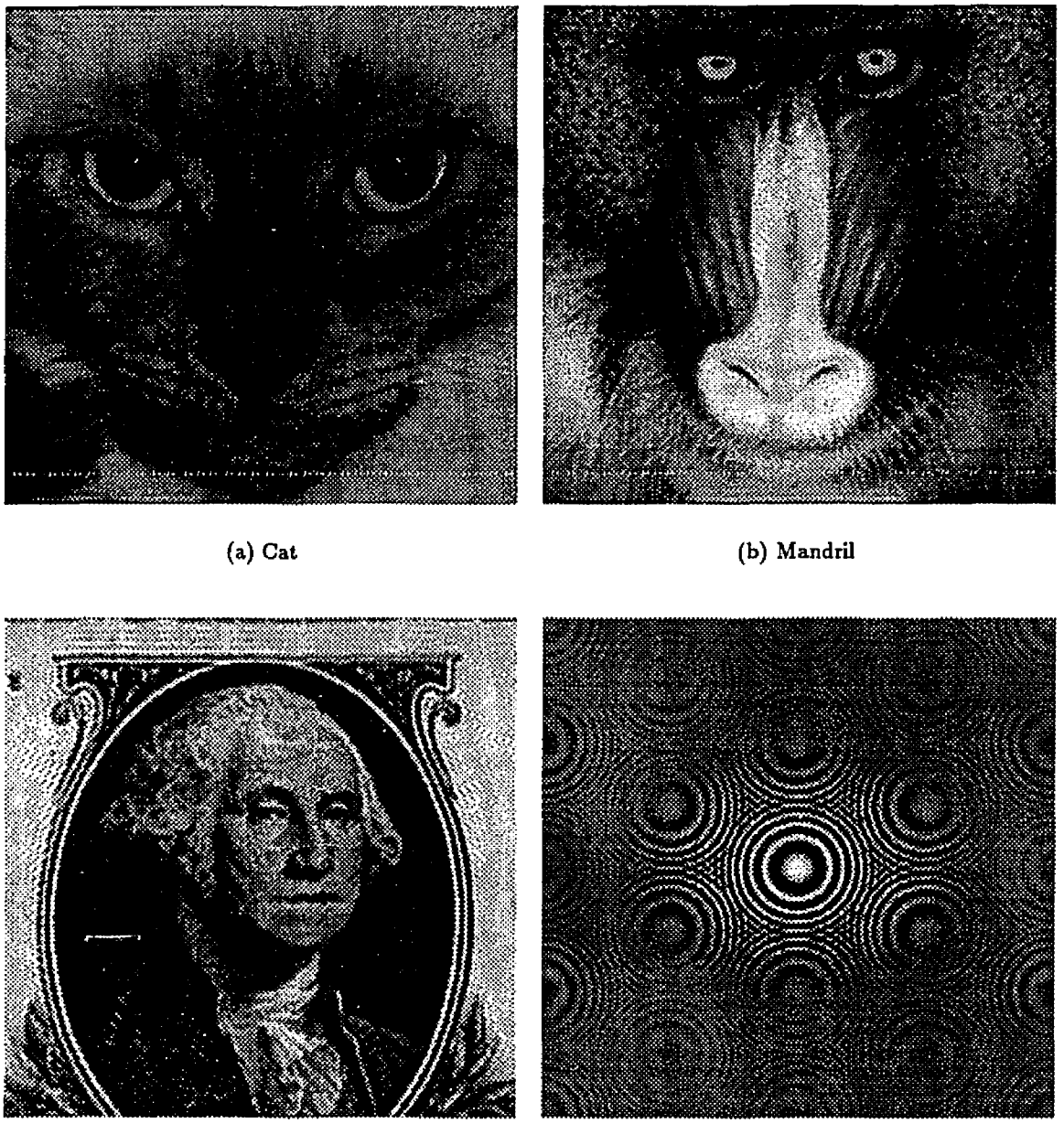

(a) Cat

(b) Mandril

(c) George

(d) Circles

Figure 5.35: Sensor OTF - $\alpha = 0.75$ - Hexagonal Sampling - Ideal Reconstruction

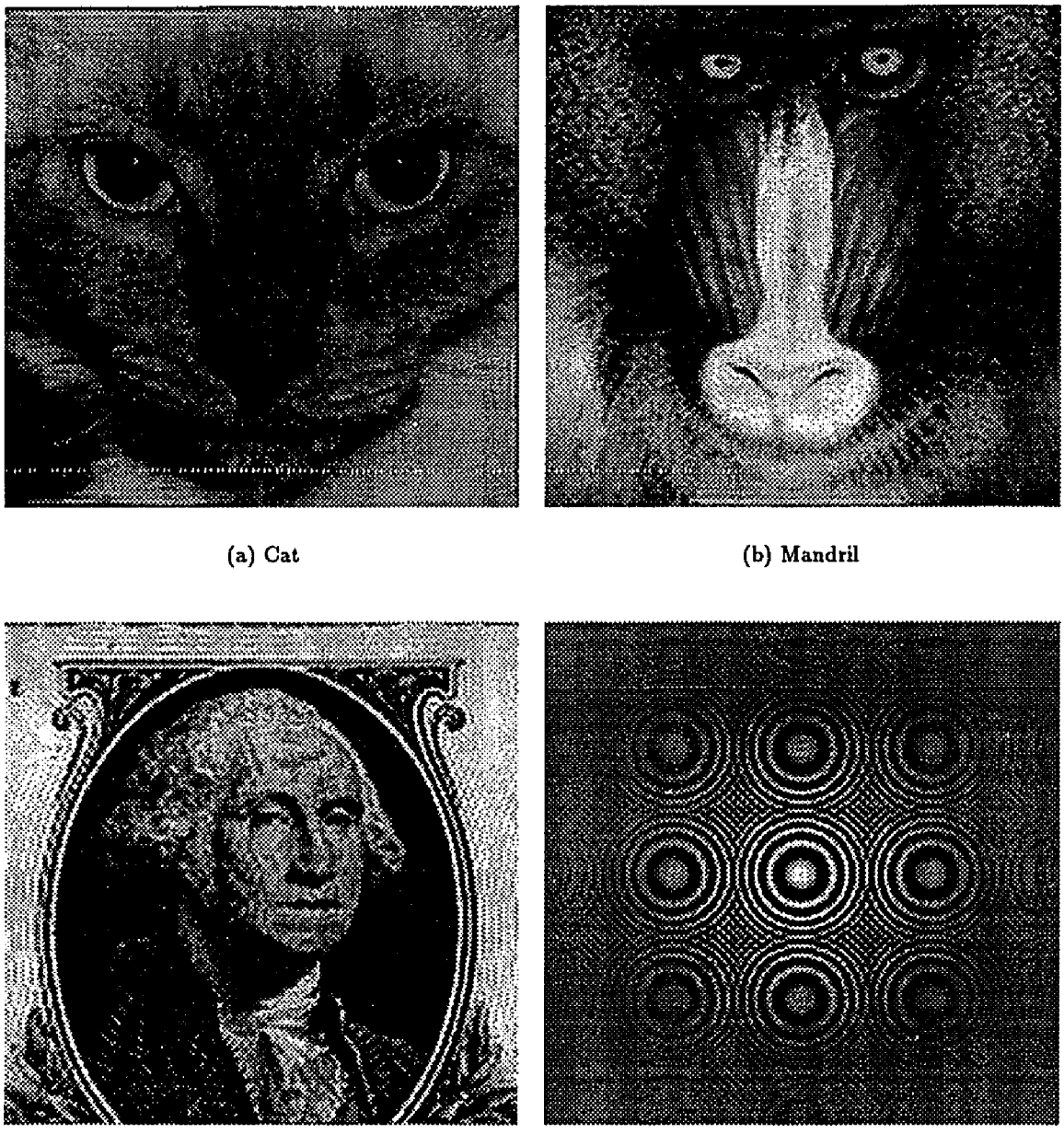

(a) Cat

(b) Mandril

(c) George

(d) Circles

Figure 5.36: No Sensor OTF - $\alpha = 0.25$ - Rectangular Sampling - Ideal Reconstruction

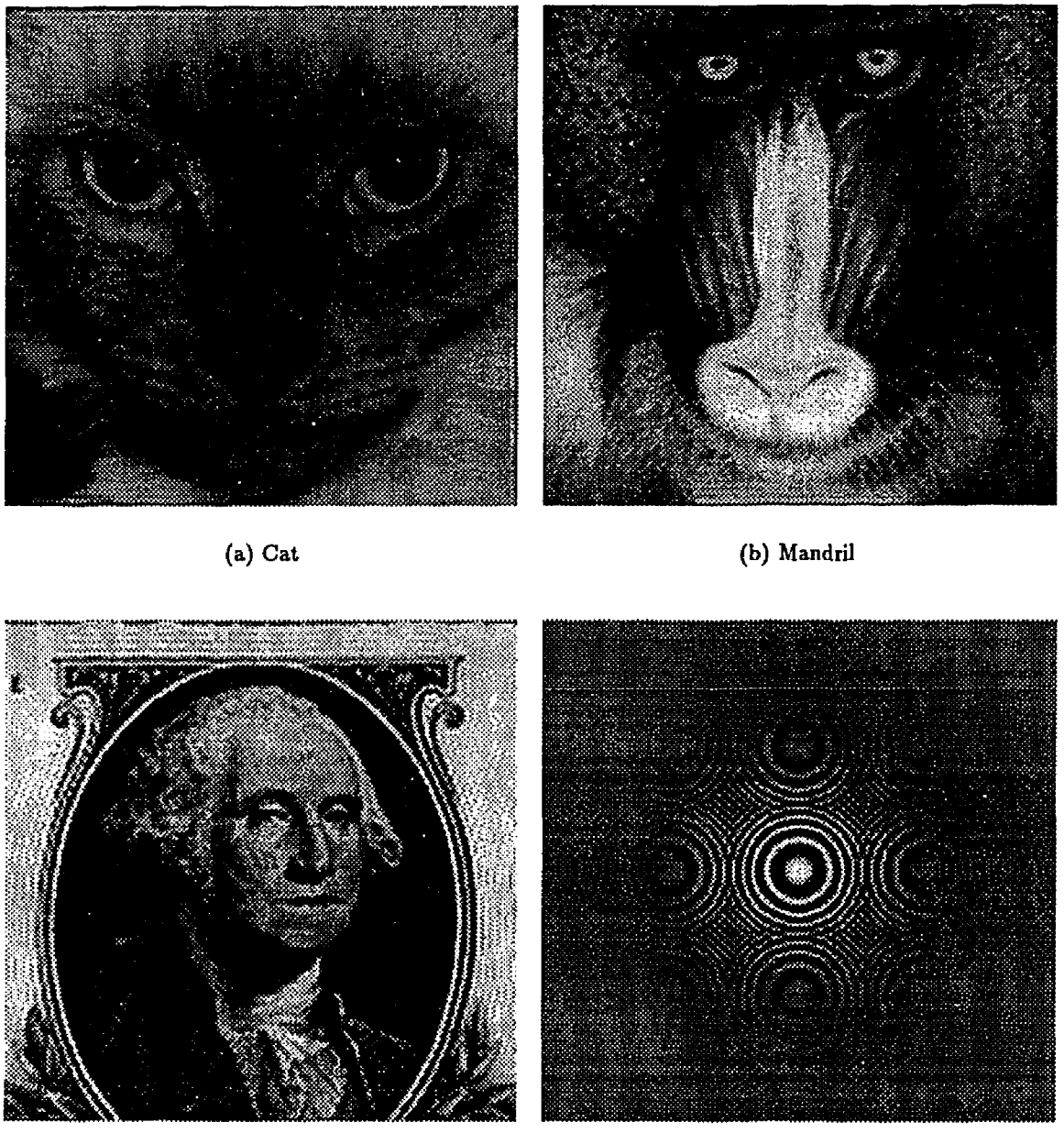

(a) Cat

(b) Mandril

(c) George

(d) Circles

Figure 5.37: Sensor OTF - $\alpha = 0.25$ - Rectangular Sampling - Ideal Reconstruction

(a) Cat

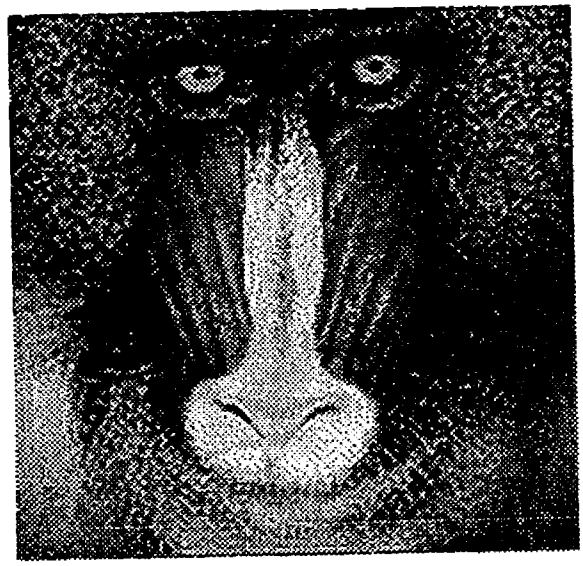

(b) Mandril

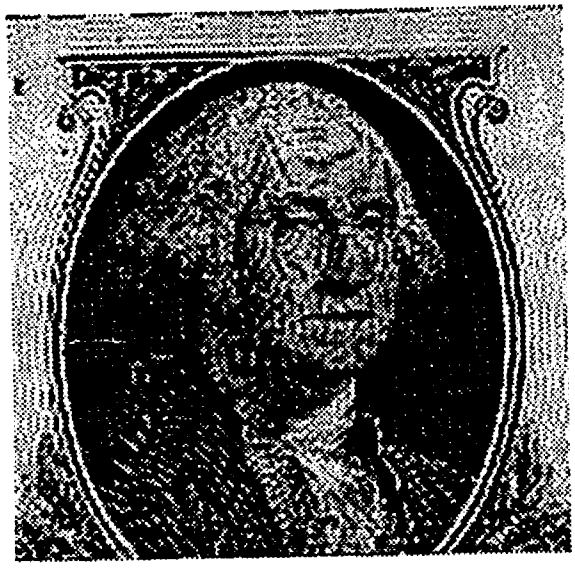

(c) George

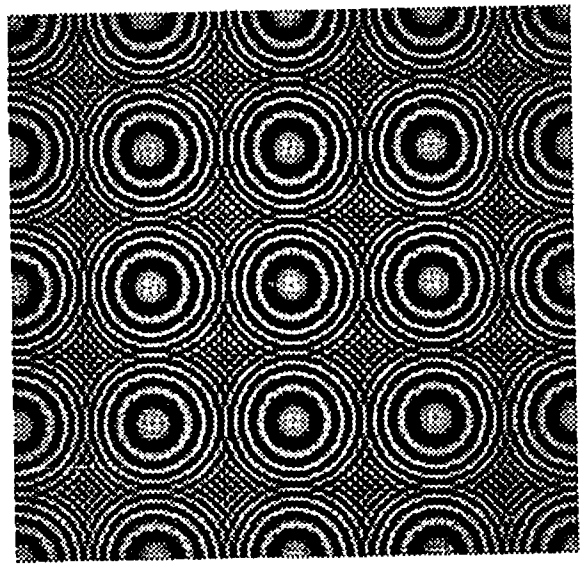

(d) Circles

Figure 5.38: No Sensor OTF - $\alpha = 0.75$ - Rectangular Sampling - Ideal Reconstruction

(a) Cat (b) Mandril

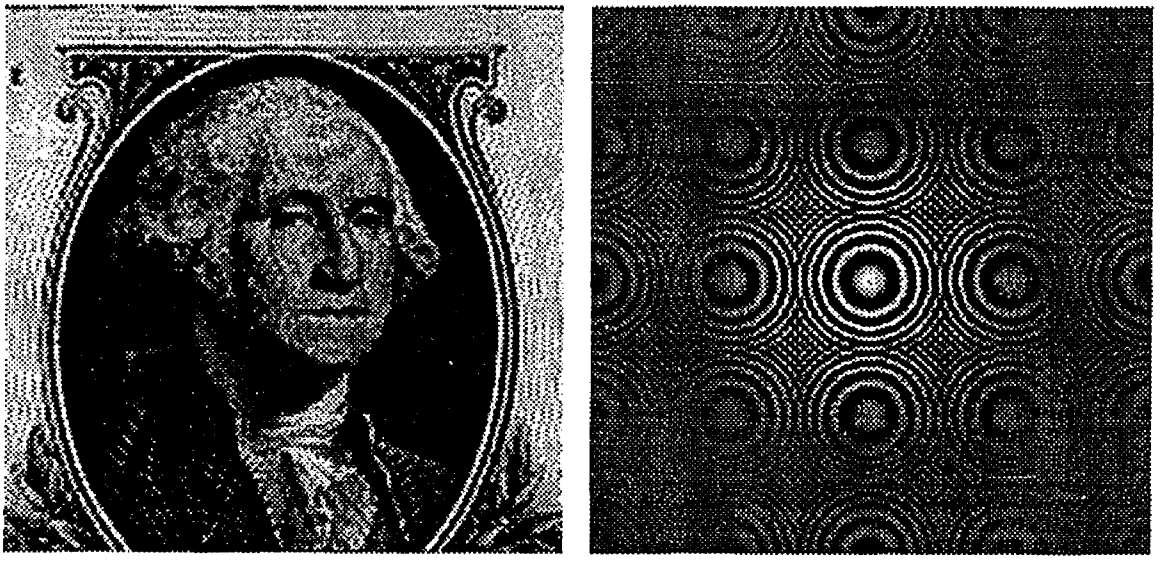

(c) George (d) Circles

Figure 5.39: Sensor OTF - $\alpha = 0.75$ - Rectangular Sampling - Ideal Reconstruction

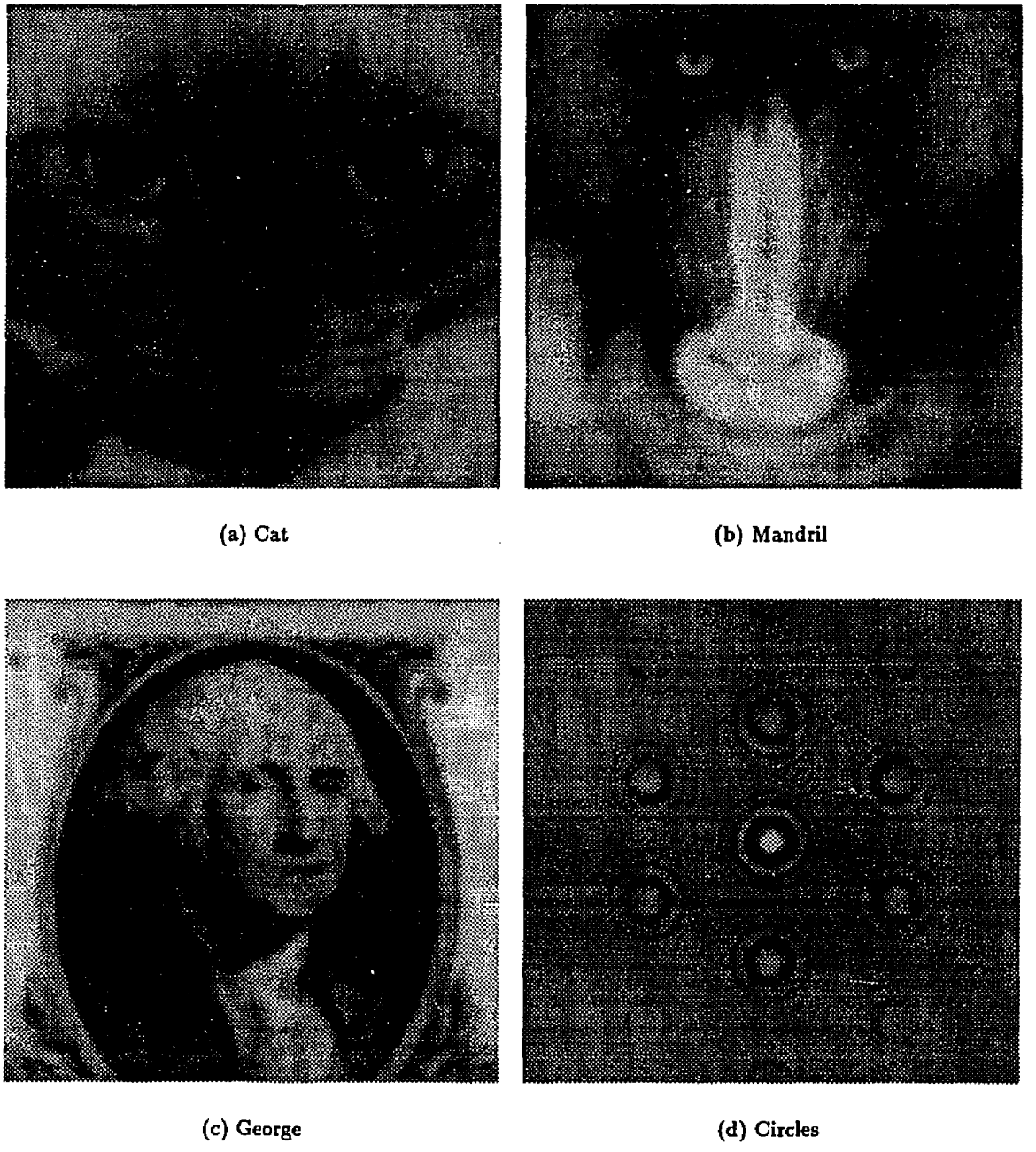

(a) Cat

(b) Mandril

(c) George

(d) Circles

Figure 5.40: No Sensor OTF - $\alpha = 0.25$ - Hexagonal Sampling - Display Reconstruction

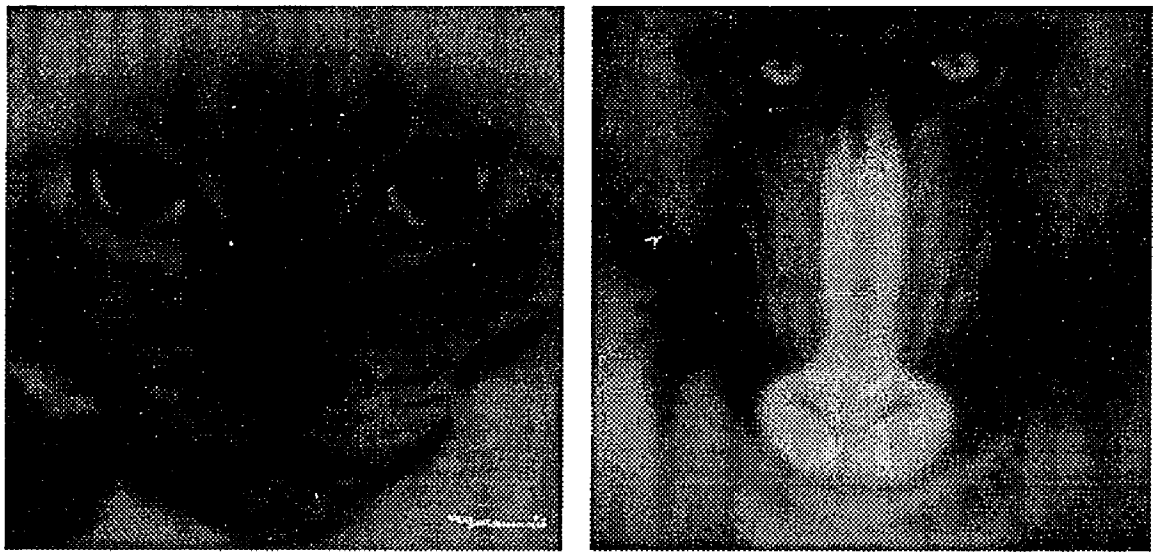

(a) Cat (b) Mandril

(c) George (d) Circles

Figure 5.41: Sensor OTF - $\alpha = 0.25$ - Hexagonal Sampling - Display Reconstruction

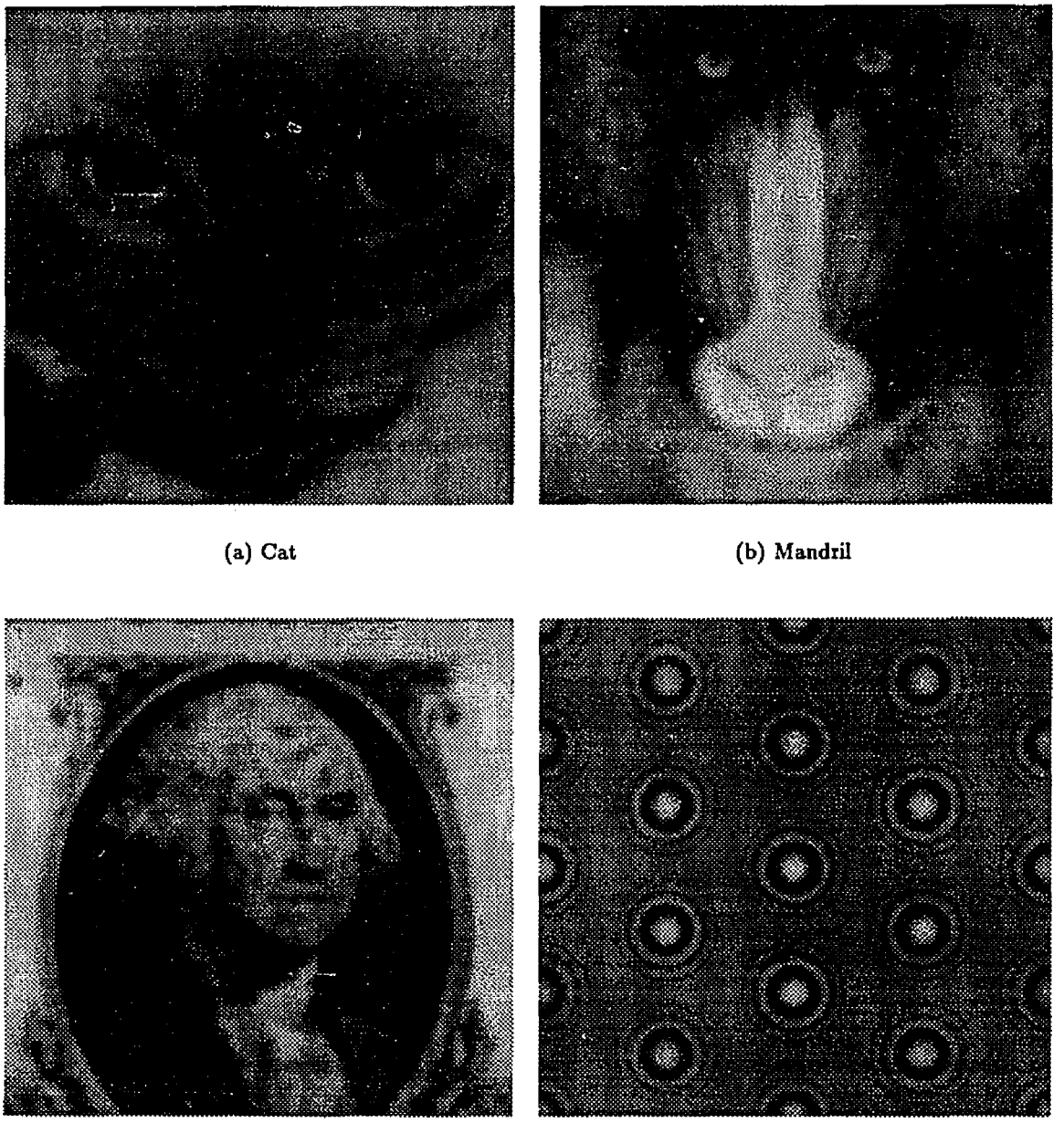

(a) Cat

(b) Mandril

(c) George

(d) Circles

Figure 5.42: No Sensor OTF - $\alpha = 0.75$ - Hexagonal Sampling - Display Reconstruction

(a) Cat

(b) Mandril

(c) George

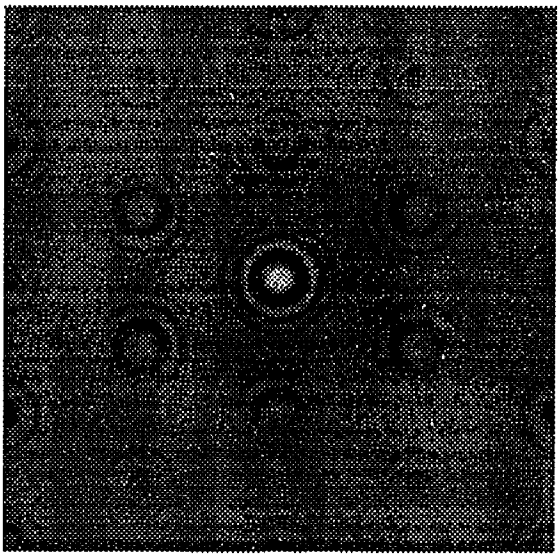

(d) Circles

Figure 5.43: Sensor OTF - $\alpha = 0.75$ - Hexagonal Sampling - Display Reconstruction

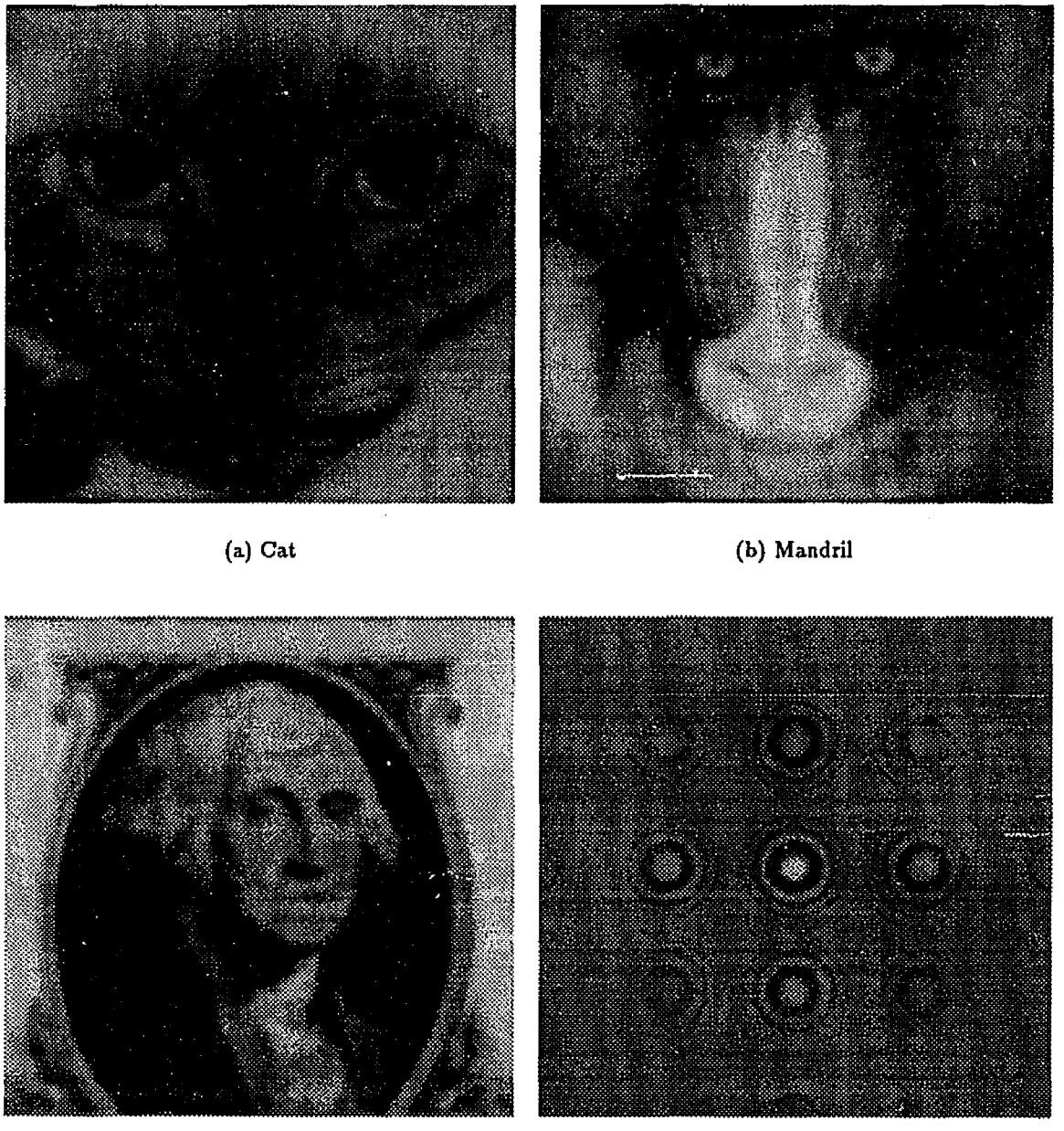

(a) Cat (b) Mandril

(c) George (d) Circles

Figure 5.44: No Sensor OTF - $\alpha = 0.25$ - Rectangular Sampling - Display Reconstruction

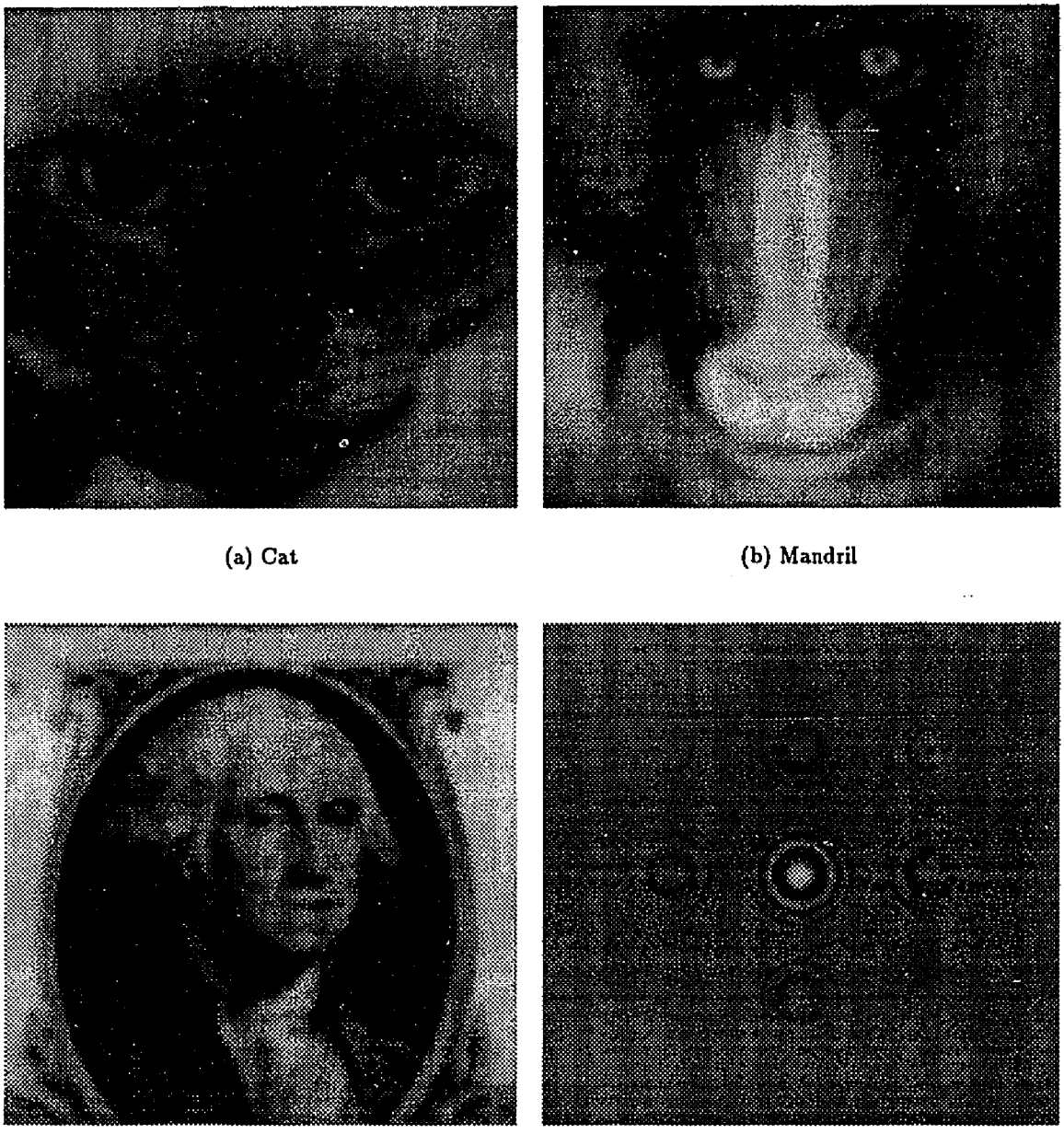

(a) Cat

(b) Mandril

(c) George

(d) Circles

Figure 5.45: Sensor OTF - $\alpha = 0.25$ - Rectangular Sampling - Display Reconstruction

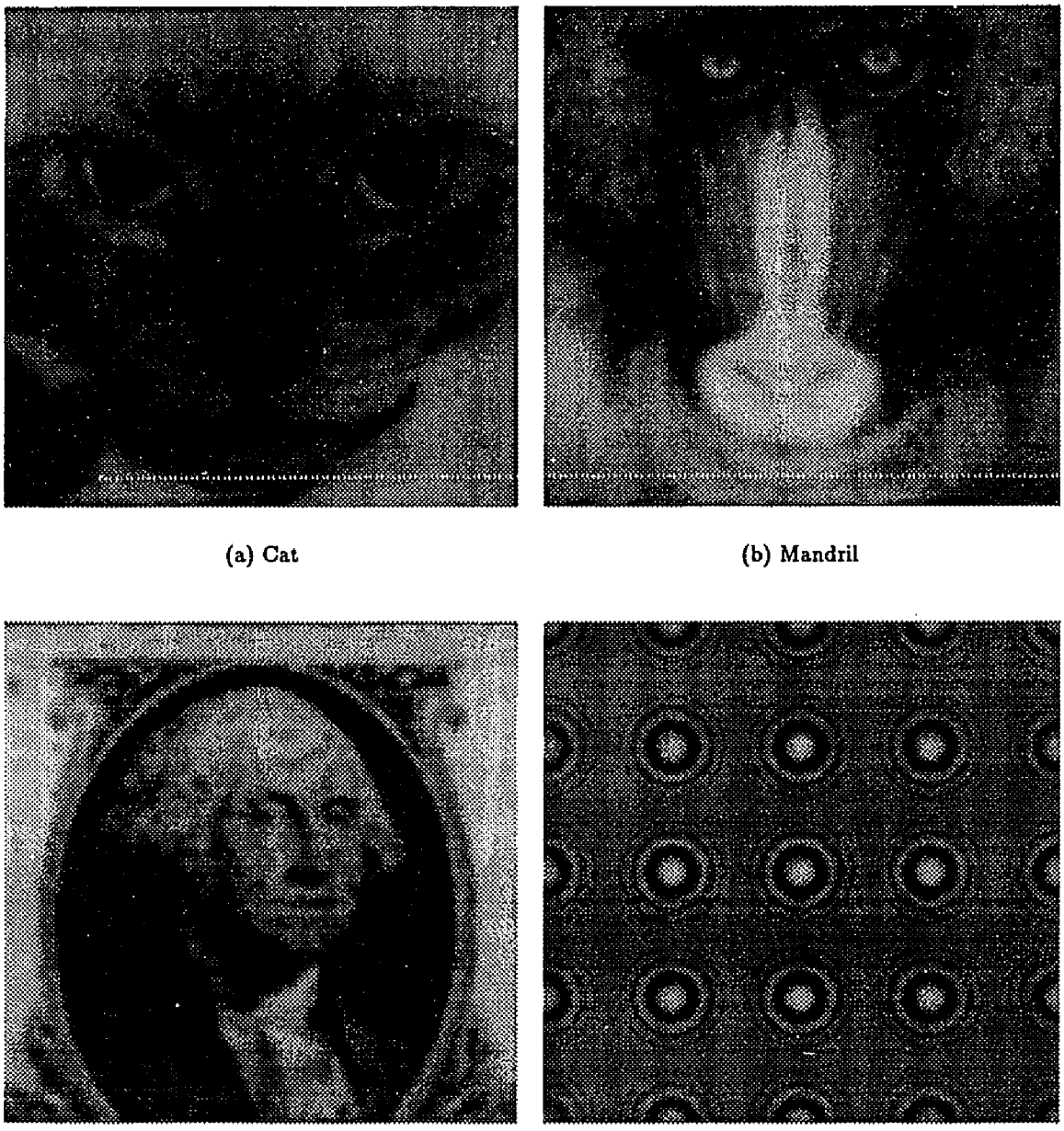

(a) Cat

(b) Mandril

(c) George

(d) Circles

Figure 5.46: No Sensor OTF - $\alpha = 0.75$ - Rectangular Sampling - Display Reconstruction

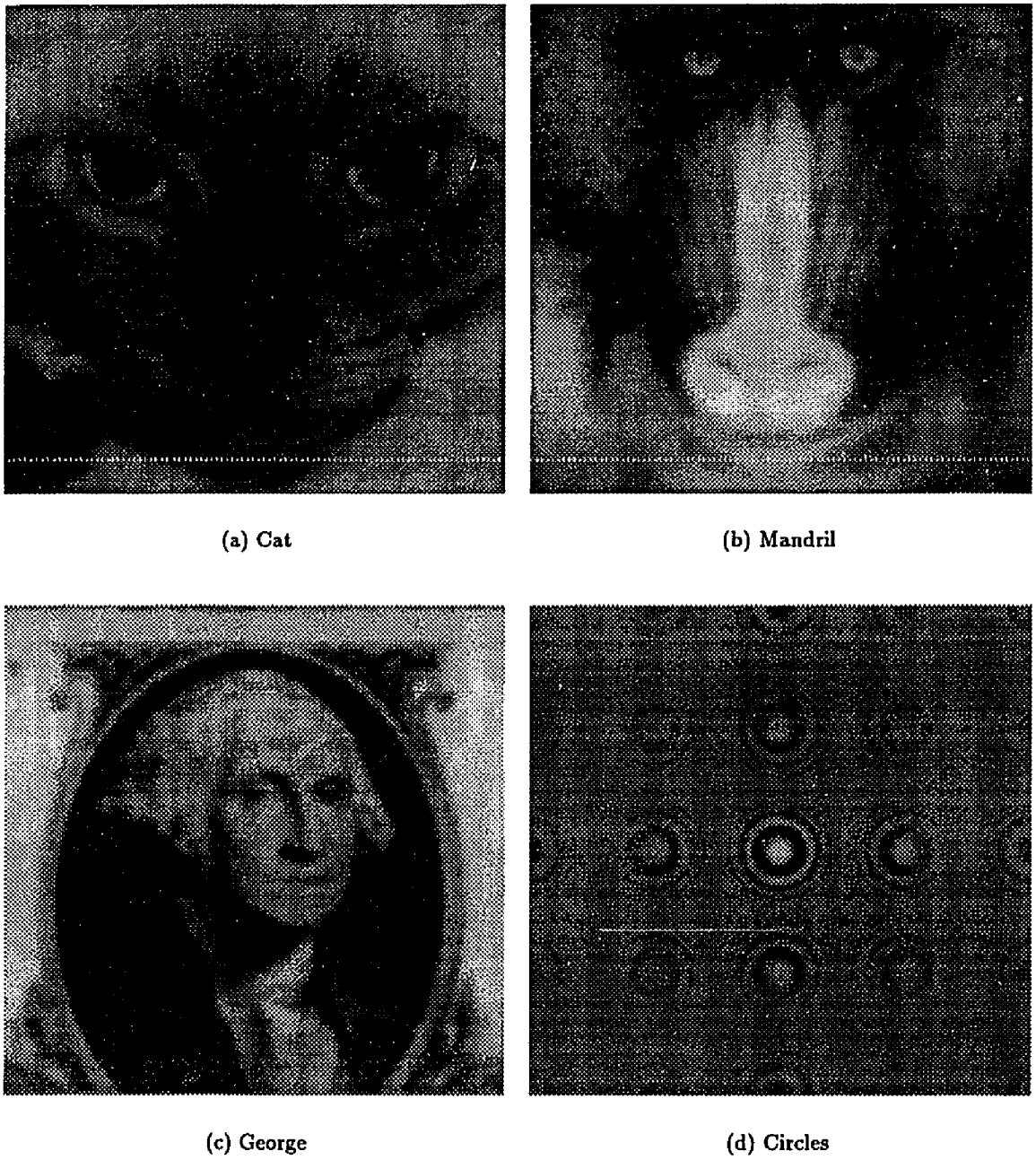

(a) Cat

(b) Mandril

(c) George

(d) Circles

Figure 5.47: Sensor OTF - $\alpha = 0.75$ - Rectangular Sampling - Display Reconstruction

References

[1] Dan E. Dudgeon and Russell M. Mersereau. *Multidimensional Digital Signal Processing.* Prentice-Hall, Englewood Cliffs, NJ, 1984.

[2] Carl L. Fales, Friedrich O. Huck, and Richard W. Samms. Image system design for improved information capacity. *Applied Optics*, 23(6):872–888, 1984.

[3] Russel M. Mersereau. The processing of hexagonally sampled two-dimensional signals. *Proceedings of the IEEE*, 67(6):930–949, 1979.

[4] Daniel P. Petersen and David Middleton. Sampling and reconstruction of wave-number-limited functions in n-dimensional euclidean spaces. *Information and Control*, 5(4):279–323, 1962.

Chapter 6

Summary and Conclusions

The comparison of a rectangularly sampled imaging system to a hexagonally sampled imaging system is a multi-step process. (1) Develop a common mathematical model that encompasses both the rectangularly sampled imaging system and the hexagonally sampled imaging system. (2) Develop a set of metrics to quantitatively measure the similarities and differences between the two imaging system. (3) Use the model and the metrics in a simulation of the two imaging systems under carefully controlled conditions. (4) Use the model and metrics to simulate the two imaging systems under more realistic (real world) conditions.

To facilitate the comparison of rectangular sampling to hexagonal sampling, a common mathematical framework for analyzing image fidelity losses in generalized sampled digital imaging systems was developed. The fidelity losses considered are due to image formation blurring, aliasing due to undersampling, and imperfect reconstruction. The analysis of the individual and combined effects of these losses was based upon an idealized, noiseless, continuous/discrete/continuous end–to–end digital imaging system model, consisting of four independent system components: an input scene, an image formation point spread function, a generalized sampling function encompassing both rectangular and hexagonal sampling lattices, and an image reconstruction function. Quantification of the image fidelity losses was accomplished via the mean–squared–error (MSE) metrics: imaging fidelity loss, sampling and reconstruction fidelity loss, and end–to–end fidelity loss. Shift–variant sampling effects are accounted for with a sample–scene phase expected value analysis. This mathematical framework was used as the basis for a series of simulations comparing a rectangular (square) sampling grid to a hexagonal sampling grid for a variety of image formation and image reconstruction conditions. The results presented provide significant insight into the tradeoffs encountered when designing a digital imaging system.

6.1 Summary of Results

- Imaging fidelity loss depends on the frequency content of the scene, image formation OTF and the sensor OTF, but not the sampling grid geometry or reconstruction function, as shown in figures 4.7, 5.4, 5.5 and 6.1.
- Sampling and Reconstruction fidelity loss depends on the frequency content of the pre-sampling image (which depends on scene frequency content, image formation OTF, and sensor OTF), sampling grid geometry, and reconstruction function. This is demonstrated in figure 4.10 for band-limited scenes, and figures 5.20 - 5.23 for digital scenes.
  - Sampling Fidelity Loss (ϵ_s^2), shown in figure 4.8 for band-limited scenes and figures 5.12 - 5.15 and 6.2 for digital scenes, is a measure of the fidelity loss caused by the folding of significant image energy at frequencies beyond the Nyquist limit into lower frequencies where the frequency response of the reconstruction function is non-zero.
  - Reconstruction Fidelity Loss (ϵ_r^2) is a measure of the fidelity loss due to the presence of significant pre-sampling image energy at frequencies where the frequency response of the reconstruction function is significantly different than $|\det \mathbf{V}|$. This is presented in figure 4.9 and figures 5.16 - 5.19.
- End–to–End fidelity loss is a function of the frequency content of the scene, the image formation OTF, the sensor OTF, the sampling grid geometry, and the reconstruction function, as shown in figure 4.12 and figures 5.28 - 5.31 and 6.4.
  - The ϵ_e^2 term accounts for the end–to–end fidelity loss caused by significant scene energy at frequencies where the cascaded response $\hat{r}[\nu]\hat{h}[\nu]$ is different from $|\det \mathbf{V}|$. ϵ_e^2 is a measure of how well the reconstruction function is able to restore frequencies that were suppressed prior to sampling by the image gathering OTF, as shown in figure 4.11 and figures 5.24 - 5.27 and 6.3.
- The fundamental nature of the end–to–end fidelity loss observed for the ideal and display reconstruction functions was markedly different, as shown in figures 6.2 and 6.3.
  - The end–to–end fidelity loss for the ideal reconstruction functions consisted of approximately equal portions of ϵ_s^2 and ϵ_e^2.
  - ϵ_e^2 was the dominate factor for the display reconstruction function, accounting for almost all the end–to–end fidelity loss.

This difference in fidelity loss mechanism is apparent in comparing figures 6.6 to figure 6.7. Aliasing (sampling fidelity loss) and ringing (reconstruction fidelity loss due to the sharp cut off of the ideal reconstruction functions) can be clearly seen in figure 6.6. Blurring due to the attenuation of high frequency information by the display reconstruction function is clearly visible in figure 6.7

Table 6.1 summarizes the range of fidelity loss values reported in chapters 4 and 5. The fidelity loss difference is the rectangular end-to-end fidelity loss, minus the hexagonal

Fidelity Loss Difference (%)	Ideal Reconstruction				Display Reconstruction			
	Sensor		No Sensor		Sensor		No Sensor	
	Min	Max	Min	Max	Min	Max	Min	Max
Band-limited Scene Imaging	−30	0	0	0	−30	0	0	0
Sampling & Reconstruction	0	30	0	1.5	0	12	−0.1	0.15
End-to-End	0	5	0	1.5	−0.4	0.1	−0.1	0.15
Digital Scene Imaging	−25	0	0	0	−25	0	0	0
Sampling & Reconstruction	0	60	−0.2	4	0	30	−0.06	0.3
End-to-End	−1	6	−0.05	2.5	−0.3	0.06	−0.02	0.2

Table 6.1: Range of Fidelity Loss Values

end–to–end fidelity loss, as a percentage of the rectangular end–to–end fidelity loss.

6.2 Conclusions

The simulation results indicate that for most of the conditions investigated, hexagonal sampling is at best marginally superior to rectangular sampling in terms of end-to-end fidelity loss. Although there can be advantages to the use of a hexagonal sampling grid in certain fields, the choice of a particular sampling grid must be considered in the context of the end–to–end system to determine the possible consequences. Improvements in one area of the system can have adverse effects in other areas. The metrics developed in this thesis provide an excellent basis for examining the individual and combined effects of the various imaging system components on image fidelity.

6.3 Future Efforts

The development and implementation of the system model and fidelity loss metrics encompassing both hexagonal and rectangular sampling grids proved to be an interesting challenge

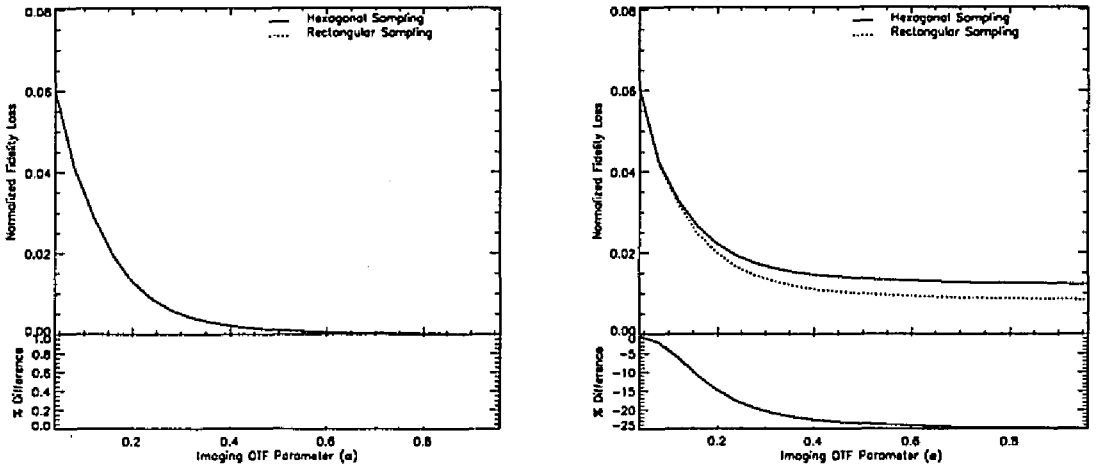

(a) No sensor OTF

(b) Sensor OTF

Figure 6.1: Imaging Fidelity Loss - George

raising several issues outside the bounds of this effort that should be addressed. The fidelity loss metrics developed are global measurements of the amount of image fidelity lost, but do not address the concerns raised by Legault [1] about resolution varying with direction in an image.

The use of a Fourier series to represent the scene, reconstructed image and various transfer functions imposes a slight implementational restriction when concerned with the fidelity loss metrics. ϵ_s^2 is defined in terms of the index $\nu - \mathbf{Uk}$ which must yield integer coordinate values in order to properly address the data in the arrays holding the Fourier series coefficients for the scene, $\hat{s}[\nu - \mathbf{Uk}]$, and the imaging OTF, $\hat{h}[\nu - \mathbf{Uk}]$. The discrete nature of the Fourier series led to another minor trade-off concerning the construction of the sensor OTFs. The model for the sensors implemented is basically an active area surrounded by a fill zone which separates the adjacent sensors. While the areas of the active regions for the rectangular and hexagonal sensors were the same, the number of discrete locations in the regions were different. This difference was responsible for the results indicating the hexagonal sensor produced higher imaging fidelity loss than rectangular sensor.

From an examination of the restored images presented in this thesis it is apparent that images with similar levels of fidelity loss can vary markedly when compared subjectively. This subject was addressed briefly by Hazra et.al. [2] in an attempt to related the perceived

image quality to the fidelity loss metrics for rectangularly sampled imaging systems. Additionally, Huck et.al. [3–6] propose alternative metrics as a measure of image quality that could be useful.

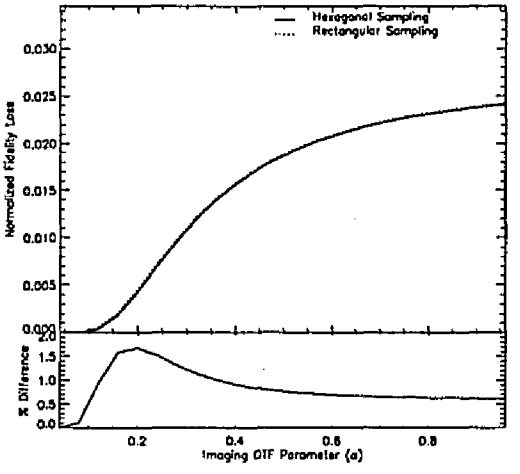

(a) No Sensor OTF - Ideal Reconstruction

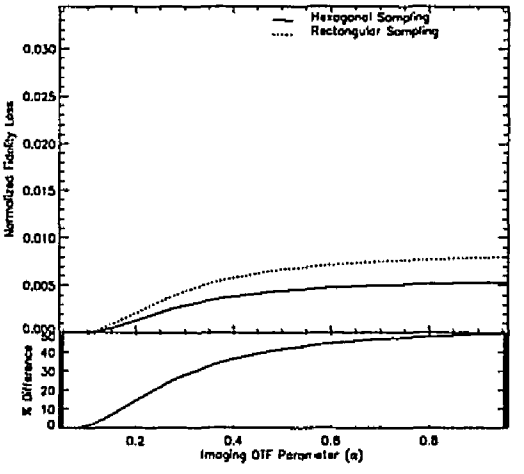

(b) Sensor OTF - Ideal Reconstruction

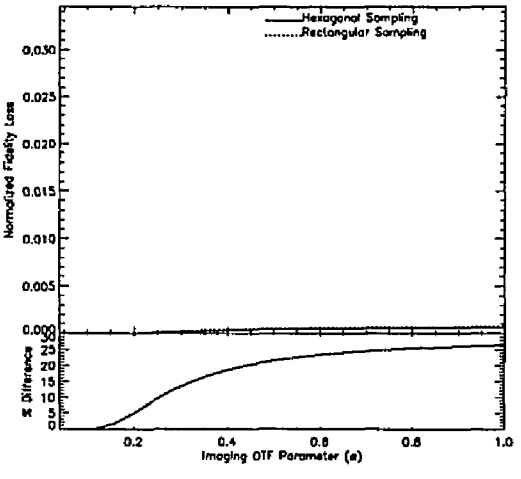

(c) No Sensor OTF - Display Reconstruction

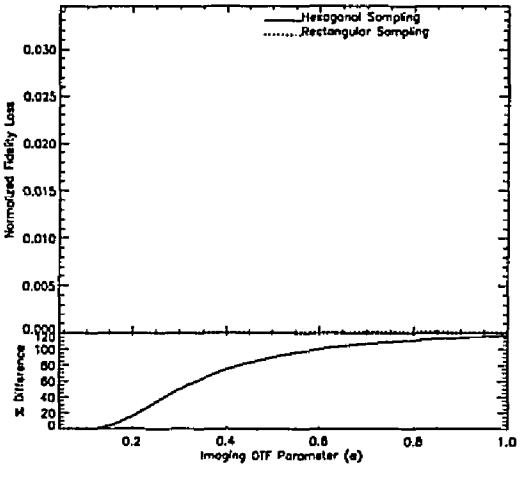

(d) Sensor OTF - Display Reconstruction

Figure 6.2: ϵ_s^2 Fidelity Loss Component - George

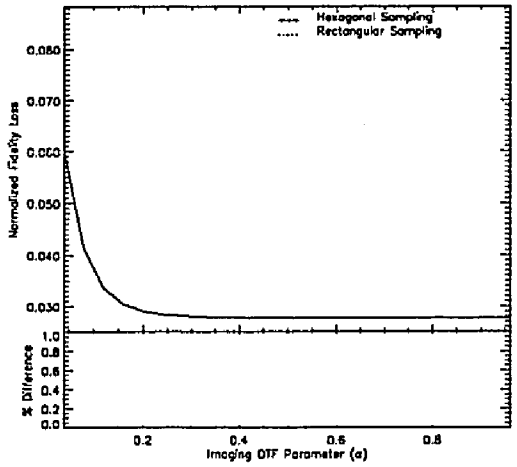

(a) No Sensor OTF - Ideal Reconstruction

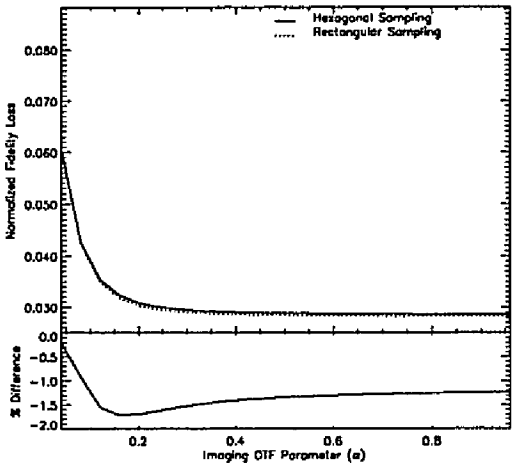

(b) Sensor OTF - Ideal Reconstruction

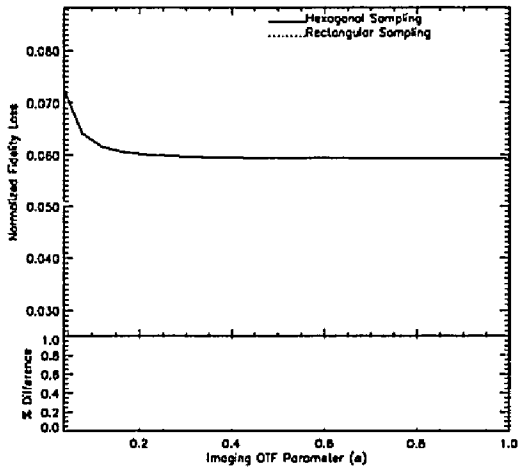

(c) No Sensor OTF - Display Reconstruction

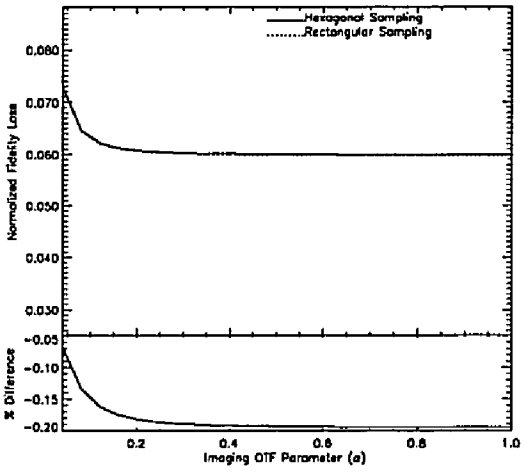

(d) Sensor OTF - Display Reconstruction

Figure 6.3: ϵ_e^2 Fidelity Loss Component - George

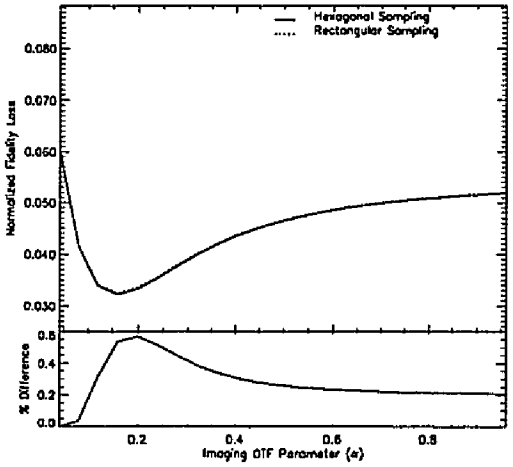

(a) No Sensor OTF - Ideal Reconstruction

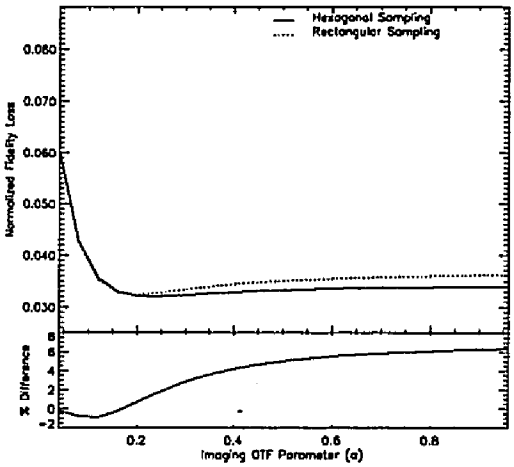

(b) Sensor OTF - Ideal Reconstruction

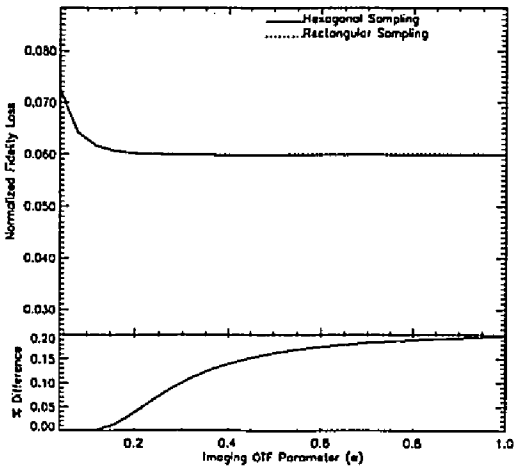

(c) No Sensor OTF - Display Reconstruction

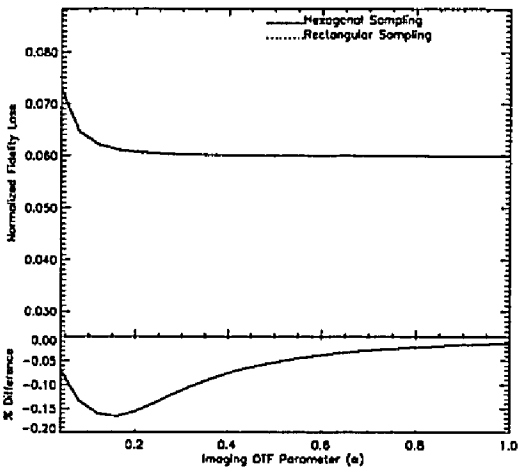

(d) Sensor OTF - Display Reconstruction

Figure 6.4: End-to-end Fidelity Loss - George

(a) Original Scene - $MSE = 0.0$

(b) $\alpha = 0.75$ - $MSE = 0.00872$

(c)
Hexagonal Sensor - $\alpha = 0.75$
$MSE = 0.01928$

(d)
Rectangular Sensor - $\alpha = 0.75$
$MSE = 0.01652$

Figure 6.5: Effect of Image Formation OTF on Scene (α parameter and sensor shape)

(a)
Hexagonal Sampling - No Sensor
$MSE = 0.03547$

(b)
Rectangular Sampling - No Sensor
$MSE = 0.03570$

(c)
Hexagonal Sampling - Sensor
$MSE = 0.03205$

(d)
Rectangular Sampling - Sensor
$MSE = 0.03264$

Figure 6.6: End–to–end Fidelity Loss - $\alpha = 0.75$ - Ideal Reconstruction

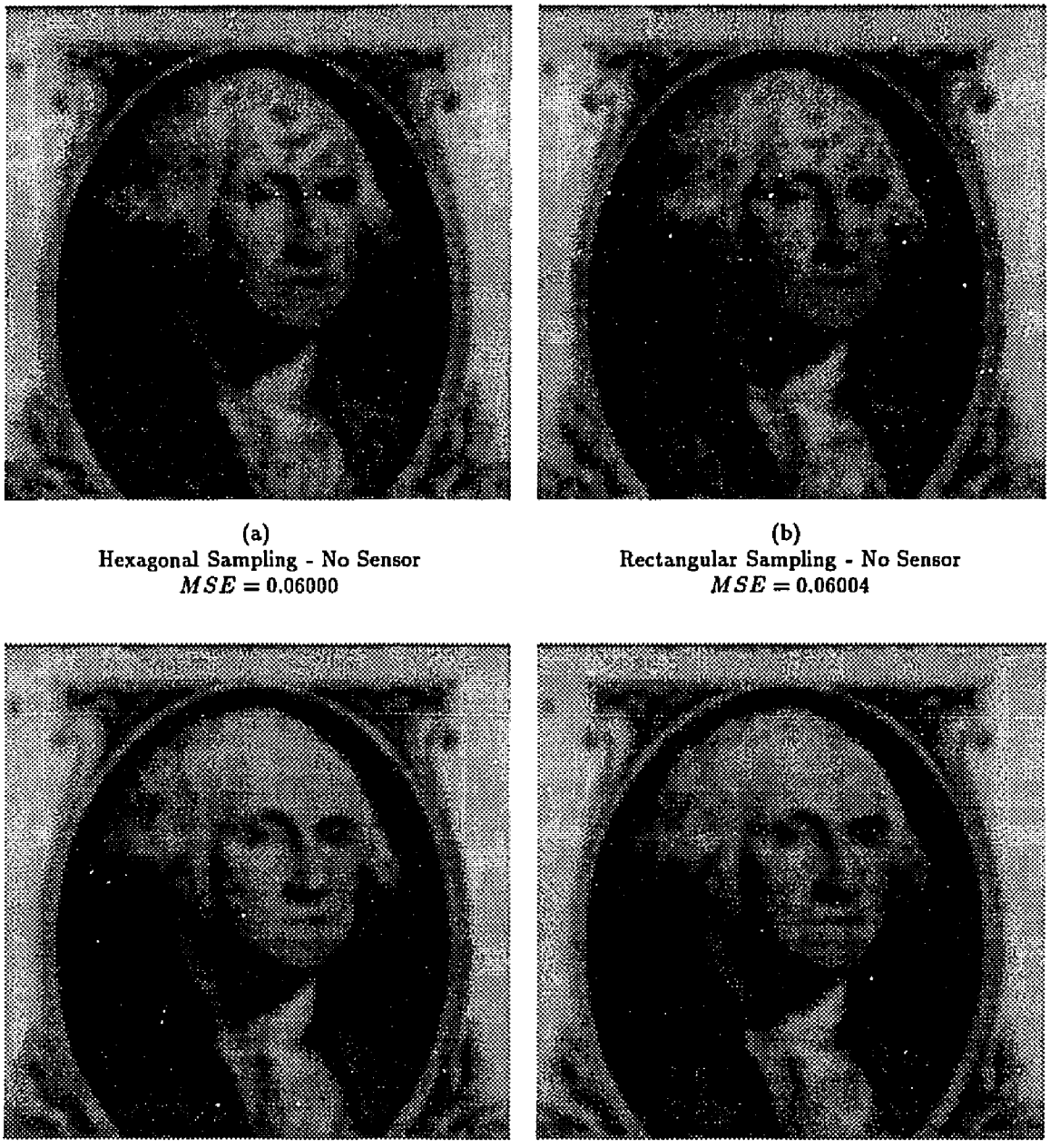

(a)
Hexagonal Sampling - No Sensor
$MSE = 0.06000$

(b)
Rectangular Sampling - No Sensor
$MSE = 0.06004$

(c)
Hexagonal Sampling - Sensor
$MSE = 0.06049$

(d)
Rectangular Sampling - Sensor
$MSE = 0.06040$

Figure 6.7: End–to–end Fidelity Loss - $\alpha = 0.75$ - Display Reconstruction

References

[1] Richard R. Legault. The aliasing problems in two-dimensional sampled imagery. In Lucien M. Biberman, editor, *Perception of Displayed Information*, chapter 7, pages 279–312. Plenum Press, New York, NY, 1973.

[2] Rajeeb Hazra, Keith W. Miller, and Stephen K. Park. Model-based quantification of image quality. In *Visual Information Processing for Television and Telerobotics*, pages 11–22. NASA Conf. Pub. 3053, 1989.

[3] Carl L. Fales and Friedrich O. Huck. An information theory of image gathering. *Information Sciences*, 23(6):872–888, 1990. Accepted for publication in *Information Sciences.*

[4] Friedrich O. Huck, Carl L. Fales, Stephen K. Park, and Richard W. Samms. Image-plane processing for improved computer vision. In *NASA Conference Publication 2302*, pages 19–34. NASA, August 1983.

[5] Friedrich O. Huck, Sarah John, Judith A. McCormick, and Ramkumar Narayanswamy. Image gathering and coding for digital restoration: Information efficiency and visual quality. In *Visual Information Processing for Television and Telerobotics*, pages 11–91. NASA Conf. Pub. 3053, 1989.

[6] Friedrich O. Huck, Sarah John, and Stephen E. Reichenbach. Information theoretical assessment of image gathering and coding for digital restoration. In *Visual Communications and Image Processing V*, pages 1590–1607. Proc. SPIE 1360, 1990.

Bibliography

Milton Abramowitz and Irene A. Stegun, editors. *Handbook of Mathematical Functions.* Dover, New York, NY, 1965.

H. C. Andrews and B. R. Hunt. *Digital Image Restoration.* Prentice-Hall, Englewood Cliffs, NJ, 1977.

Dana H. Ballard and Christopher M. Brown. *Computer Vision.* Prentice-Hall, Englewood Cliffs, NJ, 1982.

Sara B. M. Bell, Fred C. Holroyd, and David C. Mason. A digital geometry for hexagonal pixels. *Image and Vision Computing,* 7(3):194–204, 1989.

Ronald N. Bracewell. Discrete Hartley transform. *Journal of the Optical Society of America,* 73(12):1832–1835, 1983.

Ronald N. Bracewell. The fast Hartley transform. *Proceedings of the IEEE,* 72(8):1010–1018, 1984.

Ronald N. Bracewell. *The Fourier Transform and Its Applications.* McGraw-Hill, New York, NY, revised second edition, 1986.

Ronald N. Bracewell. *The Hartley Transform.* Oxford University Press, New York, NY, 1986.

Ronald N. Bracewell, O. Buneman, H. Hao, and J. Villasenor. Fast two-dimensional Hartley transform. *Proceedings of the IEEE,* 74(9):1282–1283, 1986.

E. O. Brigham. *The Fast Fourier Transform.* Prentice-Hall, Englewood Cliffs, NJ, 1974.

Donald E. Brown. Digital image restoration: A comparative analysis. Master's thesis, George Washington University, 1987.

Oscar Buneman. Multidimensional Hartley transforms. *Proceedings of the IEEE,* 75(2):267, 1987.

John C. Burton, Keith W. Miller, and Stephen K. Park. Fidelity metrics for hexagonally sampled digital imaging systems. *Journal of Imaging Technology*, 17(6):279–283, 1991.

John C. Burton, Stephen K. Park, and Keith W. Miller. Hexagonally sampled digital imaging system analysis. In *SPSE's 43rd Annual Conf.*, pages 238–241. SPSE, 1990.

Kenneth R. Castleman. *Digital Image Processing.* Prentice-Hall, Englewood Cliffs, NJ, 1979.

Kwan F. Cheung and Robert J. Marks. Image sampling below the nyquist density without aliasing. *Journal of the Optical Society of America A*, 7(1):92–105, 1990.

J. W. Cooley and J. W. Tukey. An algorithm for the machine calculation of complex Fourier series. *Mathematics of Computation*, 19(90):297–301, 1965.

Robert M. Cramblitt and Jan P. Allebach. Analysis of time-sequential sampling with a spatially hexagonal lattice. *Journal of the Optical Society of America*, 73(11):1510–1517, 1983.

Richard O. Duda and P. E. Hart. *Pattern Classification and Scene Analysis.* John Wiley and Sons, New York, NY, 1973.

Dan E. Dudgeon and Russell M. Mersereau. *Multidimensional Digital Signal Processing.* Prentice-Hall, Englewood Cliffs, NJ, 1984.

Carl L. Fales and Friedrich O. Huck. An information theory of image gathering. *Information Sciences*, 23(6):872–888, 1990. Accepted for publication in *Information Sciences.*

Carl L. Fales, Friedrich O. Huck, Judith A. McCormick, and Stephen K. Park. Wiener restoration of sampled image data: End-to-end analysis. *Journal of the Optical Society of America A*, 5(3):300–314, 1988.

B. Roy Frieden. Image restoration by discrete convolution of minimal length. *Journal of the Optical Society of America*, 64(5):682–686, 1974.

Marcel Golay. Hexagonal parallel pattern transformations. *IEEE Transactions on Computers*, C-18(8):733–740, 1969.

Rafael C. Gonzalez and Paul Wintz. *Digital Image Processing.* Addison-Wesley, Reading, MA, second edition, 1987.

Stephen B. Gray. Local properties of binary images in two dimensions. *IEEE Transactions on Computers*, C-20(5):551–561, 1971.

William B. Green. *Digital Image Processing: A Systems Approach.* Van Nostrand Reinhold, New York, NY, 1983.

R. W. Hamming. *Digital Filters.* Prentice-Hall, Englewood Cliffs, NJ, second edition, 1983.

R. V. L. Hartley. A more symmetrical Fourier analysis applied to transmission problems. *Proceedings of the IRE*, 30:144–150, 1942.

Rajeeb Hazra, Keith W. Miller, and Stephen K. Park. Model-based quantification of image quality. In *Visual Information Processing for Television and Telerobotics*, pages 11–22. NASA Conf. Pub. 3053, 1989.

Berthold Klaus Paul Horn. *Robot Vision.* MIT Press, Cambridge, MA, 1986.

H. S. Hou. The fast Hartley transform. In *Applications of Digital Image Processing VIII*, volume 575, pages 24–32. SPIE, 1985.

Friedrich O. Huck, Carl L. Fales, Nesim Halyo, Richard W. Samms, and Kathryn Stacy. Image gathering and processing: Information and fidelity. *Journal of the Optical Society of America A*, 2(10):1644–1666, 1985.

Friedrich O. Huck, Carl L. Fales, Daniel J. Jobson, Stephen K. Park, and Richard W. Samms. Image-plane processing of visual information. *Applied Optics*, 23(18):3160–3167, 1984.

Friedrich O. Huck, Carl L. Fales, Judith A. McCormick, and Stephen K. Park. Image-gathering system design for information and fidelity. *Journal of the Optical Society of America A*, 5(3):285–299, 1988.

Friedrich O. Huck, Carl L. Fales, Stephen K. Park, and Richard W. Samms. Image-plane processing for improved computer vision. In *NASA Conference Publication 2302*, pages 19–34. NASA, August 1983.

Friedrich O. Huck, Sarah John, Judith A. McCormick, and Ramkumar Narayanswamy. Image gathering and coding for digital restoration: Information efficiency and visual quality. In *Visual Information Processing for Television and Telerobotics*, pages 11–91. NASA Conf. Pub. 3053, 1989.

Friedrich O. Huck, Sarah John, and Stephen E. Reichenbach. Information theoretical assessment of image gathering and coding for digital restoration. In *Visual Communications and Image Processing V*, pages 1590–1607. Proc. SPIE 1360, 1990.

Sarah John, Zia-ur Rahman, Friedrich O. Huck, and Stephen E. Reichenbach. Information theoretical assessment of digital imaging systems. In *Infrared Imaging Systems: Design, Analysis, Modeling, and Testing*, pages 53–66. Proc. SPIE 1309, 1990.

Behzad Kamgar-Parsi and Behrooz Kamgar-Parsi. Quantization error in hexagonal sensory configurations. *IEEE Transactions on Pattern Analysis and Machine Intelligence*, 11(9):929–940, 1989.

Behzad Kamgar-Parsi and Behrooz Kamgar-Parsi. Quantization error in hexagonal sensory configurations. *IEEE Transactions on Pattern Analysis and Machine Intelligence*, 14(6):665–671, 1992.

Behzad Kamgar-Parsi, Behrooz Kamgar-Parsi, and William A. III Sander. Quantization error in spatial sampling: Comparison between square and hexagonal pixels. In *Proceedings of the Conference on Computer Vision and Pattern Recognition*, pages 604–611. IEEE Computer Society, 1989.

Donald E. Knuth. *The Art of Computer Programming: Fundamental Algorithms*, volume 1. Addison-Wesley, Reading, MA, second edition, 1973.

Donald E. Knuth. *The Art of Computer Programming: Seminumerical Algorithms*, volume 2. Addison-Wesley, Reading, MA, second edition, 1981.

R. Kumaresan and P. K. Gupta. Vector-radix algorithm for a 2-D discrete Hartley transform. *Proceedings of the IEEE*, 74(5):755–757, 1986.

Donald L. Lansing and Stephen K. Park. Quantitative analysis of the reconstruction performance of interpolants. Technical Report 2688, NASA, Washington, DC, May 1987.

Richard R. Legault. The aliasing problems in two-dimensional sampled imagery. In Lucien M. Biberman, editor, *Perception of Displayed Information*, chapter 7, pages 279–312. Plenum Press, New York, NY, 1973.

Lewis N. Lester and John Sandor. Computer graphics on a hexagonal grid. *Comput. & Graphics*, 8(4):401–409, 1984.

Martin D. Levine, editor. *Vision in Man and Machine*. McGraw-Hill, New York, NY, 1985.

Robert J. Marks. Multidimensional signal sample dependency at nyquist densities. *Journal of the Optical Society of America A*, 3(2):268–273, 1986.

David Marr. *Vision*. W. H. Freeman, New York, NY, 1982.

Judith A. McCormick, Rachel Alter-Gartenberg, and Friedrich O. Huck. Image gathering and restoration: Information and visual quality. *Journal of the Optical Society of America A*, 6(7):987–1005, 1989.

Russel M. Mersereau. The processing of hexagonally sampled two-dimensional signals. *Proceedings of the IEEE*, 67(6):930–949, 1979.

Russel M. Mersereau and Theresa C. Speake. A unified treatment of Cooley-Tukey algorithms for the evaluation of multidimensional dft. *IEEE Transactions on Acoustics, Speech, and Signal Processing*, 29(5):1011–1018, 1981.

Russell M. Mersereau and Theresa C. Speake. The processing of periodically sampled multidimensional signal. *IEEE Transactions on Acoustics, Speech, and Signal Processing*, 31(5):188–194, 1983.

Don P. Mitchell and Arun N. Netravali. Reconstruction filters in computer graphics. *Computer Graphics*, 22(4):221–228, 1988.

Yoshitaka Morikawa, Masahiro Kaneda, and Hiroshi Hamada. A method for kernel separation in the multidimensional discrete Fourier transforms. *Electronics and Communications in Japan*, 65A(11):1–10, 1982.

Patrcia K. Murphy and Neal C. Gallagher. Hexagonal sampling techniques applied to Fourier and fresnel digital holograms. *Journal of the Optical Society of America*, 3(2):929–937, 1982.

Robert H. Norton and Reinhard Beer. New apodizing functions for Fourier spectrometry. *Journal of the Optical Society of America*, 66(3):259–264, 1976.

Alan V. Oppenheim and Ronald W. Schafer. *Digital Signal Processing.* Prentice-Hall, Englewood Cliffs, NJ, 1975.

Alan V. Oppenheim, Alan S. Willsky, and Ian T. Young. *Signals and Systems.* Prentice-Hall, Englewood Cliffs, NJ, 1983.

Athansios Papoulis. *Probability, Random Variables, and Stochastic Processes.* McGraw-Hill, New York, NY, 1984.

Jae H. Park. Effect of interferogram smearing on atmospheric limb sounding by Fourier transform spectroscopy. *Applied Optics*, 21(8):1356–1366, 1982.

Stephen K. Park. *Introduction to Digital Image Processing.* Unpublished Draft (Computer Science Department, College of William and Mary), 1987.

Stephen K. Park. *Discrete Linear Systems.* Unpublished Lecture Notes (Computer Science Department, College of William and Mary), 1988.

Stephen K. Park. Linear digital imaging system fidelity analysis. In *Visual Information Processing for Television and Telerobotics*, pages 3–10. NASA Conf. Pub. 3053, 1989.

Stephen K. Park. Image gathering, interpolation and restoration: A fidelity analysis. In *SPIE 1992 Technical Symposium on Visual Information Processing.* SPIE, 1992.

Stephen K. Park and Keith W. Miller. Random number generators: Good ones are hard to find. *Communications of the ACM*, 31(10):1192–1201, 1988.

Stephen K. Park and Stephen E. Reichenbach. Design of constrained digital filters for restoration and enhancement. In *SPSE's 43rd Annual Conf.*, pages 242–244. SPSE, 1990.

Stephen K. Park and Stephen E. Reichenbach. Digital image gathering and minimum mean-square error restoration. In *Visual Communications and Image Processing V*, pages 1578–1589. Proc. SPIE 1360, 1990.

Stephen K. Park and Robert A. Schowengerdt. Image sampling, reconstruction, and the effect of sample-scene phasing. *Applied Optics*, 21(17):3142–3151, 1982.

Stephen K. Park and Robert A. Schowengerdt. Image reconstruction by parametric cubic convolution. *Computer Vision, Graphics, and Image Processing*, 23:258–272, 1983.

Stephen K. Park, Robert A. Schowengerdt, and Mary-Anne Kaczynski. Modulation-transfer-function analysis for sampled image systems. *Applied Optics*, 23(15):2572–2582, 1984.

Daniel P. Petersen and David Middleton. Sampling and reconstruction of wave-number-limited functions in n-dimensional euclidean spaces. *Information and Control*, 5(4):279–323, 1962.

Daniel P. Petersen and David Middleton. Reconstruction of multidimensional stochastic fields from discrete measurements of amplitude and gradient. *Information and Control*, 7(4):445–477, 1964.

William K. Pratt. *Digital Image Processing.* John Wiley and Sons, New York, NY, 1978.

Kendall Jr. Preston. Feature extraction by golay hexagonal pattern transforms. *IEEE Transactions on Computers*, C-20(9):1007–1014, 1971.

Zia-ur Rahman, Sarah John, Friedrich O. Huck, and Stephen E. Reichenbach. Information theoretical assessment of image gathering and coding for digital restoration. In *SPSE 43rd Annual Conf.*, page 194. SPSE, 1990.

Stephen E. Reichenbach. *Small-Kernel Image Restoration.* PhD thesis, College of William and Mary, July 1989.

Stephen E. Reichenbach, John C. Burton, and Keith W. Miller. A comparison of algorithms for computing the two-dimensional discrete Hartley transform. *Journal of the Optical Society of America A*, 6(6):818–823, 1989.

Stephen E. Reichenbach and Stephen K. Park. Computer generated scenes and simulated imaging. In *Optical Society of America Annual Meeting*, volume 11, page 170. OSA Technical Digest 11, 1988.

Stephen E. Reichenbach and Stephen K. Park. Optimal focal-plane restoration. In *Visual Information Processing for Television and Telerobotics*, pages 23–32. NASA Conf. Pub. 3053, 1989.

Stephen E. Reichenbach and Stephen K. Park. Two-parameter cubic convolution for image reconstruction. In *Visual Communications and Image Processing IV*, pages 833–840. Proc. SPIE 1199, 1989.

Stephen E. Reichenbach, Stephen K. Park, Rachel Alter-Gartenberg, and Zia-ur Rahman. Artificial scenes and simulated imaging. In *Stochastic and Neural Methods in Signal Processing, Image Processing, and Computer Vision*, volume 1569, pages 422–433. SPIE, 1991.

Azriel Rosenfeld and Avinash C. Kak. *Digital Picture Processing.* Academic Press, Orlando, FL, second edition, 1982.

Sheldon M. Ross. *Introduction to Probability Models.* Academic Press, Orlando, FL, third edition, 1985.

Sr. Schade, Otto H. Image reproduction by a line raster process. In Lucien M. Biberman, editor, *Perception of Displayed Information*, chapter 6, pages 233–278. Plenum Press, New York, NY, 1973.

Robert Schowengerdt, Stephen K. Park, and Robert Gray. Topics in the two-dimensional sampling and reconstruction of images. *International Journal of Remote Sensing*, 5(2):333–347, 1984.

Claude Shannon and Warren Weaver. *The Mathematical Theory of Communication.* University of Illinois Press, Urbana, IL, 1964. Originally published in the *Bell System Technical Journal*, 27:379–423 and 28:623–656, 1948.

Claude E. Shannon. Communication in the presence of noise. *Proceedings of the IRE*, 37(1):10–21, 1949.

Theresa C. Speake and Russell M. Mersereau. An interpolation technique for periodically sampled two-dimensional signals. In *Proceedings of the International Conference on Acoustics, Speech, and Signal Processing*, pages 1010–1013. IEEE, 1981.

R. C. Staunton. The design of hexagonal sampling structures for image digitization and their use with local operators. *Image and Vision Computing*, 7(3):162–166, 1989.

Robert Ulichney. *Digital Halftoning.* MIT Press, Cambridge, MA, 1987.

Andrew B. Watson and Albert J. Ahumada. A hexagonal orthogonal–oriented pyramid as a model of image representation in visual cortex. *IEEE Transactions on Biomedical Engineering*, 36(1):97–106, 1989.

Andrew B. Watson and Allen Poirson. A separable two-dimensional discrete Hartley transform. *Journal of the Optical Society of America A*, 3(12):2001–2004, 1986.

H. Joseph Weaver. *Applications of Discrete and Continuous Fourier Analysis.* John Wiley and Sons, New York, NY, 1983.

John Clifton Burton II

John Burton was born in Staunton, Virginia, February 15, 1956. He Graduated from Quantico High School, Quantico, Virginia, in 1974. He earned a Bachelor of Science degree in Chemical Engineering with honors from The University of Virginia, Charlottesville, Virginia, in 1978. He worked as a research engineer for Badische Corp. in Williamsburg, Virginia from 1978 to 1985. From 1985 to 1993 he attended the College of William and Mary in Williamsburg, Virginia. While at William and Mary, he earned a Master of Science degree in Computer Science in 1987. He completed the requirements for the degree of Doctor of Philosophy in Computer Science in 1993.